USE OF NEAR INFRARED AND VISIBLE SPECTROSCOPIES TO DETERMINE OPTICAL PROPERTIES OF RAT NERVOUS SYSTEM

by

HARSHA RADHAKRISHNAN

Presented to the Faculty of the Graduate School of

The University of Texas at Arlington in Partial Fulfillment

of the Requirements

for the Degree of

MASTER OF SCIENCE IN BIOMEDICAL ENGINEERING

THE UNIVERSITY OF TEXAS AT ARLINGTON

August 2006

ACKNOWLEDGEMENTS

This thesis is a collaborative effort and thus requires acknowledging a lot of people. First and foremost, I thank my wife, Shivani Gupta, for her love and support and constant advice without which this would not have been possible.

Dr. Hanli Liu, thank you very much for allowing me to explore the length and breadth of my abilities. Dr. Yuan Bo Peng, thank you very much for all those amazing insights without which this study would not have seen its final form. I also like to thank Dr. Kytai Nguyen for serving on my committee and helping me put this thesis together.

A special mention goes out to Arun K Senapati for having put up with me in times of trouble too.

Finally, mom and dad and my in-laws, thank you very much for letting me do what I wanted to and get away with it most of the time.

June 22 2006

ABSTRACT

USE OF NEAR INFRARED SPECTROSCOPY TO DETERMINE OPTICAL PROPERTIES OF RAT CENTRAL NERVOUS SYSTEM

Publication No. _____

Harsha Radhakrishnan, M.S

The University of Texas at Arlington, 2006

Supervising Professor: Hanli Liu, Ph. D.

The goal of this thesis is to determine changes in the light scattering and hemoglobin oxygen saturation in three cases: (i) a normal spinal cord, (ii) demyelinated sciatic nerve, and (iii) spinal cord under neuronal activity induced by peripheral electrical stimulation. We hypothesize that (i) nerve demyelination or degeneration would result in a decrease in light scattering and hemoglobin oxygen saturation and (ii)

peripheral electrical stimulation would show an increase in light scattering and hemoglobin oxygen saturation.

The experiments were done using a one source, one detector fiber optic needle probe with a source-detector separation of 100 microns. Optical reflectance data was obtained using the probe connected to a CCD array spectrometer grated in the wavelength range of 350 to 1100 nm. We used prior developed algorithms for detecting reduced scattering coefficient and hemoglobin oxygen saturation. Based on the spectral data obtained, we statistically proved all our hypotheses.

TABLE OF CONTENTS

Appendix

LIST OF ILLUSTRATIONS

LIST OF TABLES

CHAPTER 1

INTRODUCTION

1.1 Central Nervous System

The central nervous system (CNS) consists of the brain and the spinal cord. This report focuses on the optical properties on the rat spinal cord to peripheral electrical stimulation and also changes in optical properties of sciatic nerve due to spinal nerve ligation. Explanation of the anatomy / properties of the brain are beyond the scope of this report.

1.1.1 Structure of Spinal Cord

The spinal cord is a long column of nervous tissue extending from the brain stem. In a cross section, the spinal cord is made up of a butterfly shaped gray matter (Fig. 1.1) that is in the middle of the cord and is completely surrounded by white matter.

Gray matter is comprised of nerve cell bodies, dendrites, short inter-neurons, glia, and large blood volume (Fox, 1993). It is divided into anterior and posterior horns, and the right and left are connected by the gray commissure. White matter is made up of bundles of mostly myelinated axons, which give white color and have less hemoglobin concentration than gray matter. Myelin increases light scattering, so white matter is expected to have a greater degree of scattering. In the wavelength range of 500-1000 nm, gray matter has a higher absorption than white matter (van der Zee et al., 1993).

This may be attributed to a higher hemoglobin concentration (Svaasand and Ellingsen, 1983). The formation of gray matter in the spinal cord is H-shaped as shown in Figure 1. This shape remains the same throughout the cord, though there are regional variations in size and shape of gray and white matter.

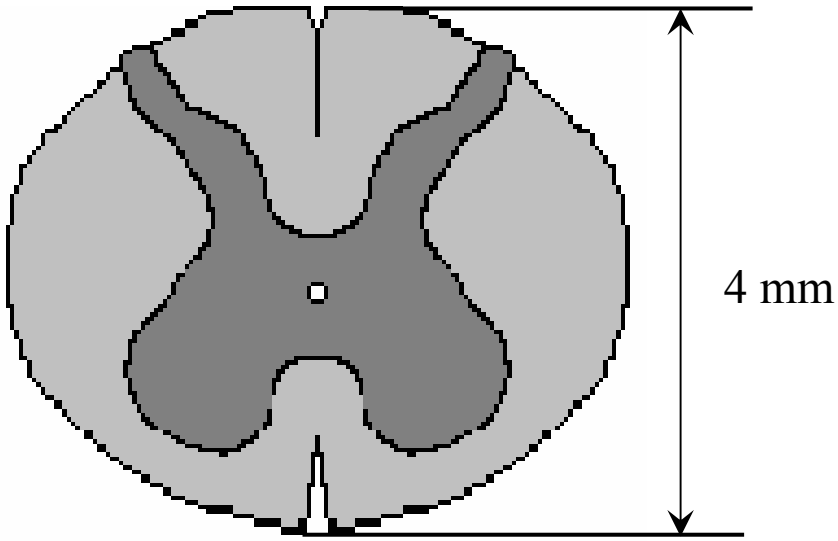

Figure 1.1: Cross section view of the lumbar region of the spinal cord. The darker region is gray matter surrounded by the lighter region of white matter, and the diameter of this section of the spinal cord is around 4 mm. Such formations are prominent through out the spinal cord though the conformations are different in each region.

1.1.2 Structure of Sciatic Nerve

The peripheral nervous system consists of axons that receive sensory input and send motor output. Some peripheral nerves are pure sensory, while others are pure motor in nature. Depending on the location of their paths, most nerves have both components. For example, each segment of the lumbar spinal cord has a dorsal root and a ventral root on each side. A dorsal root receives somatosensory input from a certain

area of the body part, whereas a ventral root will innervate certain groups of muscle. Shortly outside the spinal cord, the dorsal root and ventral root will merge to form the spinal nerve; thus, the spinal nerve has both sensory and motor components. Further down to the periphery, several lumbar spinal nerves form the sciatic nerve. In Sprague-Dawley rats, it is found (Gelderd and Chopin, 1977; Hebel and Stromberg, 1986) that the sciatic nerve is composed of spinal nerves L4-L6, while a further study showed that it was only L4 and L5 that made up the major part of the sciatic nerve, and that the contribution of L3 or L6 varied from rat to rat (Asato et al., 2000).

1.2 Near Infrared Spectroscopy

Near infrared spectroscopy (NIRS) has been widely investigated for a variety of biomedical applications using the wavelength range of 700 – 900 nm. NIR radiation offers the advantage of being non-ionizing, and, therefore, repeated doses can be given to the subject. Moreover, optical imaging instrumentation is inexpensive, robust, unobtrusive and portable. These properties make it one of the simplest methods to examine tissue optical properties. Over the years, optical methods have been used to detect both physiological and pathological conditions of tissue, including measurements for blood flow (Edwards et al., 1993; Elwell et al., 1993), hemoglobin concentration (Isobe et al., 2000), as well as for cancer diagnosis (Mourant et al., 1995, 1998; Liu et al., 2000), tissue distinction (Mourant et al., 1996; Johns et al., 1998, Nilsson et al., 1998; Zonois et al., 1999), and tissue oxygenation (Kurth and Thayer, 1999).

The underlying theory behind NIRS is that when light propagates within a tissue, it undergoes multiple elastic scattering and absorption depending on tissue

optical properties. The prominent properties are the scattering coefficient of the tissue, μ_s, and the absorption coefficient of the tissue, μ_a. In the near infrared region, light scattering is more prominent than light absorption. This is because the scattering mean free path ($1/\mu_s$) of tissue for near-infrared light is on the order of 10-100 microns while the absorption mean free path ($1/\mu_a$) is much longer than the scattering mean free path. Anisotropy (g) is a measure of the amount of forward direction retained after a single scattering event. If a photon is scattered by a particle and deflected by an angle θ, the component of new trajectory aligned in the forward direction is given by $\cos(\theta)$. Therefore, an average deflection angle and the mean value of $\cos(\theta)$ is defined as anisotropy, i.e., $g = \cos(\theta)$. The two limiting cases are g = 0 for ideal isotropic scattering, and g =1 for complete forward scattering of the incident beam. The reduced scattering coefficient (μ_s') is defined as

$$\mu_s' = (1-g)\mu_s . \tag{1.1}$$

1.3 Algorithm to determine Reduced Scattering Coefficient (μ_s')

The algorithm to determine μ_s' values based on the needle-probe reflectance readings has been previously developed (Johns et al., 2003 a, b). This is an empirically developed algorithm that can calculate the μ_s' from a single optical reflectance spectrum. According to the algorithm, for a range of μ_s' values between 5 to 60 cm^{-1} and refractive index 'n' = 1.38, the relationship between μ_s' and the measured reflectance data taken with a 100-μm separation can be approximated by

$$R = a_0 \times (1.6696 \times \mu_s' - 1.5437), \tag{1.2}$$

where R is the measured reflectance, and a_0 is the intensity factor calibrated from the experiments. The unit of μ_s' is cm^{-1}, and the unit of R is the number of photons per unit area (i.e., # of photons/cm^2). The absorption coefficient, μ_a, was not included in equation (1.2) as Monte Carlo simulations (Johns et al., 2003 a, b) showed negligible changes in reflectance for typical tissue μ_a values of 0.01 cm^{-1} to 0.5 cm^{-1} in the NIR range. After performing multiple tissue-phantom experiments for empirical calibrations (Johns et al., 2003 a, b), we have determined a_0 to be equal to 0.0034 and rewritten eq. (1.2) as eq. (1.3):

$$\mu_s'(\lambda_0) = \frac{R(\lambda_0) + 1.5437\,[0.0034]}{1.6696\,[0.0034]} \quad \text{cm}^{-1}, \tag{1.3}$$

where λ_0 denotes a wavelength within the range of 700 nm to 850 nm.

Notice that the constant term, a_0, has to be determined experimentally, and that eq. (1.3) was obtained through the empirical calibration only for the specific probe used for the study. During the algorithm development, it was seen that there was a large variation in μ_s' values due to the small source-detector separations and their similarity to mean free paths. Our solution to this problem was to take 60 reflectance readings for 60 seconds at each point to reduce the noise.

1.4 Algorithm to determine Hemoglobin Oxygen Saturation (SaO_2)

One of the goals of this report is to determine changes in hemoglobin oxygen saturation due to degeneration / demyelination of sciatic nerve and also in the rat spinal cord during peripheral stimulation. To achieve this, we focused our analysis on the visible region between 500-600 nm and utilized the algorithm previously developed to

quantify hemoglobin oxygen saturation of tissue vasculature measured with a needle-like probe (Johns et al., 2001). The algorithm is based on the following theory. The steady-state diffuse reflectance (R), obtained from the diffusion theory, helps us determine optical properties of turbid media. R can be given as (Farrell et al., 1992; Mourant et al., 1997)

$$R(\rho, z_0) = \frac{I_0}{4\pi}\left[z_0\left(\mu_{eff} + \frac{1}{r_1} \right)\frac{\exp(\mu_{eff} r_1)}{r_1^{\,2}} + (z_0 + 4AD)\times\left(\mu_{eff} + \frac{1}{r_2} \right)\frac{\exp(\mu_{eff} r_2)}{r_2^{\,2}} \right] \qquad (1.4)$$

where $r_1 = \sqrt{(z_0^{\,2} + \rho^2)}$, $r_1 = \sqrt{(z_0 + 4AD)^2 + \rho^2)}$, $\mu_{eff} = \sqrt{\frac{\mu_a}{D}}$, I_0 is overall amplitude factor, z_0 is the depth of isotropic point source of a pencil beam and is equal to $z_0 = 1 / \mu_t = 1 / (\mu_a + \mu_s')$, μ_a and μ_s' are light absorption and reduced scattering coefficient, respectively. Moreover, A is a constant corresponding to internal reflection, ρ is the source-detector separation, and D is the diffusion coefficient and equal to $D = 1 / [3 \times (\mu_a + \mu_s')]$. Eq. (1.4) could be modified to suit optical reflectance probes with small source-detector separations (ρ from 0.1 to 1.0 mm). It was seen that the computationally simulated data matched the experimental data after the following modifications: $D = 1 /(3\mu_s')$ and $z_0 = 1/\mu_s'$. Using the modified factors, eq. (1.4) was reduced to the simplified model for the steady-state broadband reflectance measured in the visible range, as given below (Johns et al., 2001):

$$R(\mu_a, \mu_s') = \frac{I_0 \mu_s'^{2}}{4\pi}\left(1 + \sqrt{\frac{3\times\mu_a}{\mu_s'}} \right)\exp\left(-\sqrt{\frac{3\times\mu_a}{\mu_s'}} \right). \qquad (1.5)$$

In principle, the coefficients of μ_a and μ_s' are wavelength dependent and can be expressed as

$$\mu_a = a * \varepsilon_{HbO2}(\lambda) + b * \varepsilon_{Hb}(\lambda), \tag{1.6}$$

$$\mu_s' = -c * \lambda + d, \tag{1.7}$$

where a and b are concentrations of oxygenated hemoglobin (HbO_2) and deoxygenated hemoglobin (Hb), respectively, c and d are tissue dependent parameters (matcher et al., 1997), and ε_{HbO2} and ε_{Hb} are extinction coefficients for HbO_2 and Hb at λ respectively (Zijlstra et al., 1991). Dividing eqs. (1.6) and (1.7), we get

$$\frac{\mu_a}{\mu_s'} = \frac{a \times \varepsilon_{HbO_2} + b \times \varepsilon_{Hb}}{d - c \times \lambda}. \tag{1.8}$$

In eq. (1.8), we have four parameters a, b, c, and d that are not totally independent and cannot be determined individually. This equation is further modified into three independent parameters, $X = (a/d)$, $Y = (b/d)$ and $Z = (c/d)$. Substituting eq. (5) and X, Y, Z into eq. (1.9) yields

$$R = R_0 (1 - Z \times \lambda)^2 \left(1 + \sqrt{\frac{3\left[X \times \varepsilon_{HbO_2} + Y \times \varepsilon_{Hb} \right]}{1 - Z \times \lambda}} \right) \exp\left(- \frac{3\left[X \times \varepsilon_{HbO_2} + Y \times \varepsilon_{Hb} \right]}{1 - Z \times \lambda} \right). \tag{1.9}$$

where R_0 is an experimentally determined factor, including I_0 term, and depends on the light source intensity as well as fiber probe geometry. By fitting eq. (1.9) to the calibrated reflectance data, we would be able to obtain values of X, Y, Z, and R_0 independently. We specifically used a curve-fitting technique in MATLAB® and calculated oxygen saturation as $SO_2 = X/(X+Y) \times 100$ %.

1.5 Overview of this thesis

The overall objective of this thesis is to determine optical properties in specific regions of the rat CNS using a small source-detector separation fiber optic needle probe. The optical properties of the tissue under investigation are measured in both its healthy and artificially altered form. Specifically, the main hypothesis and aims of this study are as follows:

Hypothesis 1: Optical properties of the spinal cord can be determined using a small source-detector separation fiber optic needle probe

Aim 1: to obtain spatial maps of the rat spinal cord showing regions of varying optical properties

Hypothesis 2: There would be a decrease in the values of light scattering and hemoglobin oxygen saturation in the rat sciatic nerve due to demyelination / degeneration.

Aim 2: to determine light scattering (Chapter 2) and hemoglobin oxygen saturation values (chapter 3) of the rat sciatic nerve due to demyelination / degeneration induced by spinal nerve ligation

Hypothesis 3: There would be an increase in the values of light scattering and hemoglobin oxygen saturation in the rat spinal cord during peripheral electrical stimulation.

Aim 3: to determine light scattering and hemoglobin oxygen saturation values of the rat spinal cord during peripheral electrical stimulation.

Hypothesis 4: Peripheral electrical stimulation would induce an increase in blood flow

Aim 4: to determine values of hemoglobin derivatives on rat spinal cord during peripheral electrical stimulation

CHAPTER 2

DETERMINING REDUCED SCATTERING COEFFICIENT (μ_S') OF RAT SPINAL CORD AND CHANGES IN μ_S' OF RAT SCIATIC NERVE DUE TO DEMYELINATION

2.1 Introduction to Optical Techniques

Magnetic resonance imaging (MRI) is well suited to measure the central nervous system (CNS), and it is widely used in evaluation of patients with CNS diseases as it provides greater sensitivity and specificity for a majority of CNS disease states in comparison to other radiological imaging modalities. It has established itself as an important clinical tool and the most common method in the diagnosis of CNS dysfunctions, such as stroke, inflammatory and degenerative diseases, and brain neoplasm, as well as in detection, characterization, and determination of tumor extent (Rorden and Karnath, 2004; Symms et al., 2004). Near infrared (NIR) spectroscopy, as explained in Section 1.2 has its inherent advantages over MRI and is now being widely used in many biomedical applications.

In particular, optical properties of human brain tissue measured in the NIR range have been reported for both *ex vivo* and *in vivo* data: van der Zee measured the reflectance of gray and white matter in post mortem neonatal and adult human brain tissue and showed that gray matter has a smaller scattering coefficient and larger absorption coefficient than white matter (van der Zee et al., 1993). Bevilacqua et al.

measured optical properties of brain tissue in children intraoperatively and reported that white matter has a greater scattering coefficient (Bevilacqua et al., 1999). Such differences in light scattering between gray and white matter have resulted in the development of a new optical reflectance methodology that can be used to differentiate white and gray matter in the human brain to guide functional neurosurgery intraoperatively (Giller et al., 2000, 2003; Johns. 2003). Recently, the feasibility of using NIR for intraoperative monitoring of spinal cord oxygenation has been tested and discussed (Macnab et al., 2002; Germon, 2002).

However, there has been no report on optical properties from the spinal cord of either animals or humans, measured either *ex vivo* or intraoperatively. This chapter focuses on 1) reporting the measurement of reduced light scattering coefficient (μ_s') from the lumbar segment of the rat spinal cord surface intraoperatively using the fiber-optic optical reflectance, and 2) demonstrating that differential light scattering properties in the NIR region can be also used to differentiate healthy and diseased peripheral nerves. One potential application of this study is to utilize the light scattering parameter as a bio-signature for identifying demyelinated legions intraoperatively in the lumbar region of the spinal cord with a low-cost, portable, fiber optic reflectance system. Such a portable, miniaturized technique could be developed for minimally invasive localization of demyelinated legions along the spinal cord, particularly, for detection of certain characteristics of Multiple Sclerosis (MS) lesions in either animal models or humans in the near future.

Over the years, a large amount of research activities on the spinal cord have been involved with the electrophysiological measurements using microelectrodes to explore

fundamental neurophysiological mechanisms in the spinal cord (Baldissera et al., 1981; Marder and Calbrese, 1996; Gardner et al., 2000). In spite of the advantages the microelectrode technique has, it provides neither a real time imaging map of the spinal cord intraoperatively nor information on the extent of spatial-temporal pattern of neural activity. Other research investigations on detection of neural activities using fluorescent dyes *in vitro* have been intensively performed and reported (Wenner et al., 1996; Tsau et al., 1996; Arai et al., 1999; Murase et al., 1999; Mochida et al., 2001a, b), while the development on methodology of using optical imaging to detect neural activity *in vivo* becomes increasingly popular (Sasaki et al., 2002). In our study, we have performed our NIR reflectance measurements on both (a) the spinal cord and (b) sciatic nerves of rats.

The spinal nerve is a nerve mixed with sensory and motor axons. Cell bodies of the sensory component are located in the dorsal root ganglion, whereas cell bodies of the motor component are located in the ventral horn of the spinal cord. Both are proximal to the ligation site of the spinal nerve. It is known that damage to the nerve (e.g., tight ligation) will induce axonal degeneration at the distal part because of lack of nutrition from the cell body, further leading to a loss of myelin. It is our hypothesis that either demyelination or degeneration of the axon will lead to a decrease in light scattering of the nerve. A part of this study is to prove our hypothesis and to demonstrate that differential μ_s' values in the NIR region can be used to differentiate healthy and demyelinated peripheral nerves. Our recent study based on NIR spectral slopes with a large group of animals has been reported (Senapati et al., 2005).

2.2 Materials and Methods

2.2.1 Materials and Methods for Spinal Cord Measurements

2.2.1.1 Subjects and surgical methods

Fourteen adult male Sprague-Dawley rats (250 – 350 g, University of Texas at Arlington vivarium) were used. They were initially administered with sodium pentobarbital (50mg/kg, i.p.). The body temperature was continuously monitored at 37°C using a heating blanket with a control unit (Harvard Apparatus, Inc., Holliston, MA). Before preparing the animal for surgery, care was taken to ensure that all reflexes were eliminated. Tail pinches and eye-blinks were assessed.

Laminectomy was performed to expose the thoracic and lumbar regions of the spinal cord. For the continuous supply of anesthetic during the course of the experiment, intrajugular canulation was performed. Tracheotomy was performed to allow artificial ventilation. After surgery, the rat was mounted on a stereotaxic frame. Mineral oil (~1 cm in height, Figure 2.2) was used to prevent the drying of the exposed surface. The vital signs such as heart rate (~360 beats/min.), respiration rate, and partial pressure of carbon dioxide (PCO_2 =25 mmHg) were regularly monitored. During the entire course of study, care was taken to minimize animal suffering and to reduce the number of rats used. All the experiments have been conducted under the strict regulation of IACUC (**I**nstitution for **A**nimal **C**are and **U**se **C**ommittee) of the University of Texas at Arlington and the guidelines of International Association for Study of Pain (Zimmermann, 1983).

2.2.1.2 Experimental set up

The optical reflectance experiments from the rat spinal cord were taken intraoperatively using a light source, a bifurcated fiber optic probe, a spectrometer and a laptop computer,

as shown in Figure 2.1, in common with our previous work (Johns et al., 1998; Giller et al., 2000, 2003). The incident optical signal was generated by a tungsten-halogen light source (LS–1, Ocean Optics, Inc., Dunedin, FL) and delivered to the tissue through the probe. The optical reflectance signals from the tissue were collected by the same probe and converted to electrical signals by a portable, real-time display spectrometer (USB 2000, Ocean Optics, Inc.) in the wavelength region of 450 nm to 1000 nm. The bifurcated probe contained 2 fibers, one acting as the source and the other as a detector, each with a 100-micron diameter. The two fibers were placed adjacent to one another within a 400-micron stainless steel probe. The optic fiber probe was placed near lumbar level 5 (LL5) region of the rat spinal cord, which was mounted on a stereotaxic frame to assure a firm position of the animal. With the help of a microdrive (Burleigh 6000 ULN Controller, Burleigh Instruments, NY) the probe was held at a height of 575 microns above the exposed spinal cord surface, while the surface was covered with mineral oil (~ 10 mm in height, Figure 2.2). Since the difference in refractive index between mineral oil and tissue is minimal, the specular reflection from the spinal cord surface could be insignificant. This distance was chosen after a series of experiments that were conducted using a reflectance calibrator. The optical reflectance was measured from the calibrator at various distances up to 2 mm from the surface at intervals of 100 microns. The distance between 500 and 600 microns showed maximum reflectance intensity (Figure 2.3).

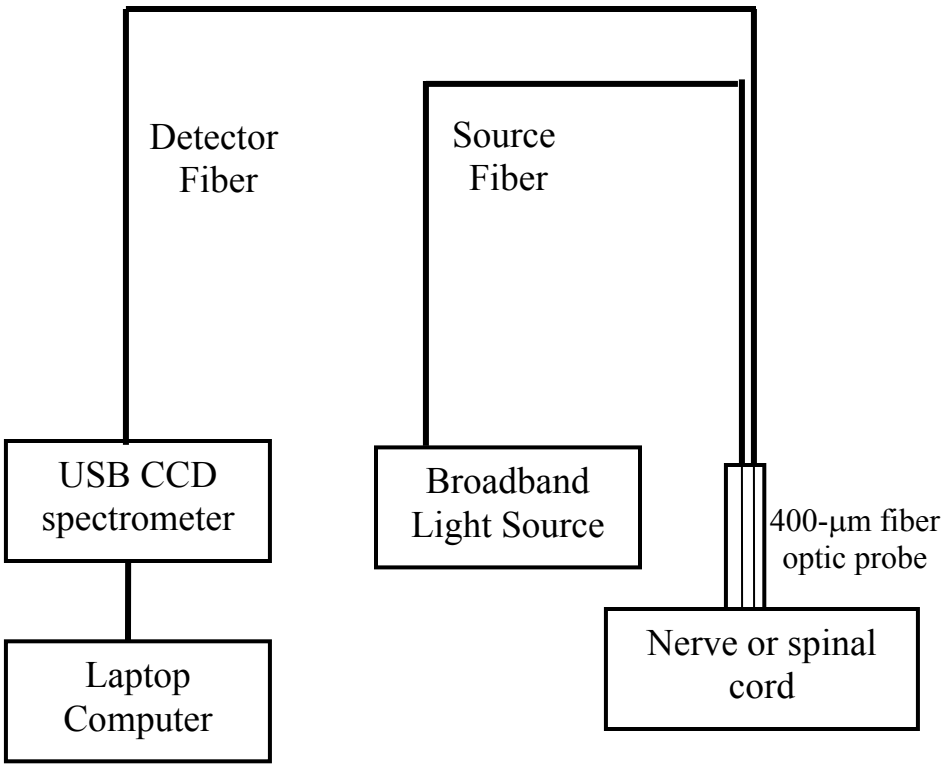

Figure 2.1: Experimental setup. This set up used to obtain data from both the spinal cord and sciatic nerves consists of two 100-μm fibers separated by a distance of 100 μm, a broadband light source, a USB CCD spectrometer, a stereotaxic frame to hold the rat with the probe focused on either the spinal cord or the sciatic nerve, and a laptop computer for data acquisition.

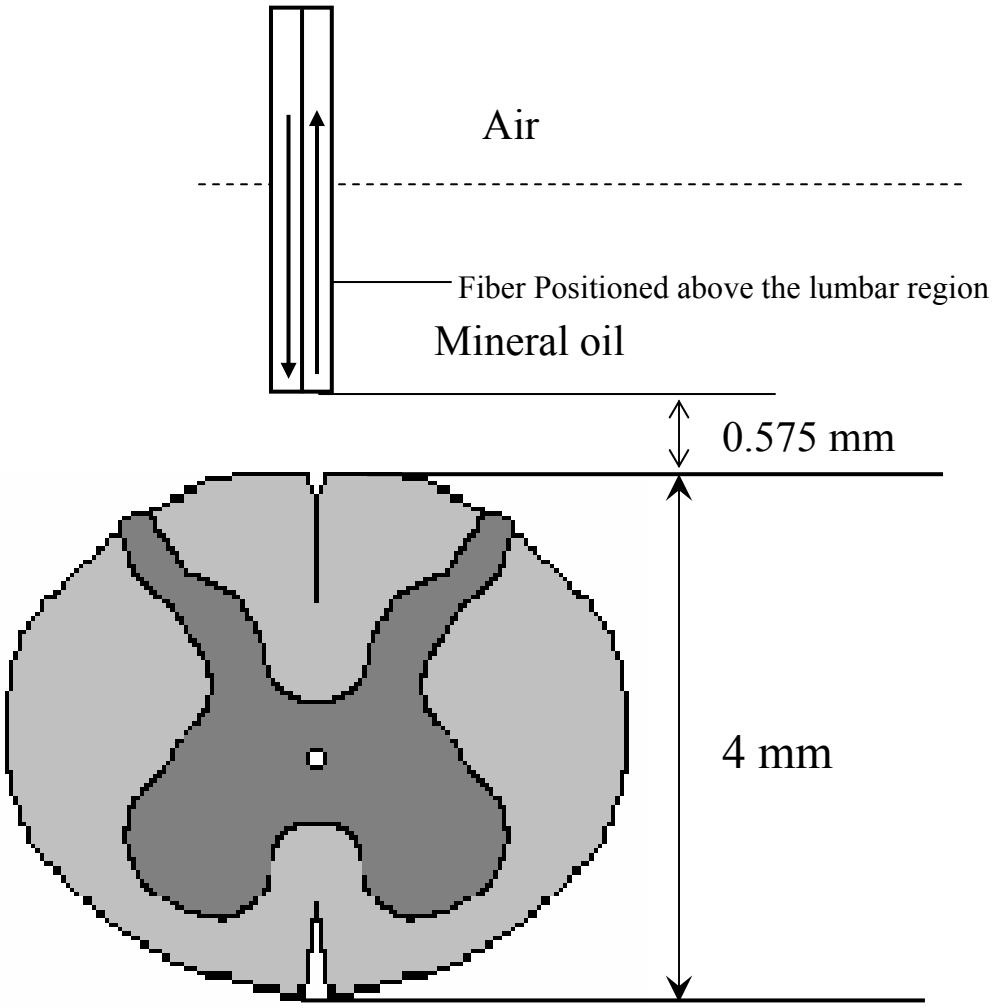

Figure 2.2**:** Cross section view of the lumbar region of the spinal cord. The darker region is gray matter surrounded by the lighter region of white matter, and the diameter of this section of the spinal cord is around 4 mm. Such formations are prominent through out the spinal cord though the conformations are different in each region. The bifurcated fiber optical probe contains two 100-μm fibers and located 0.575 mm above the spinal cord. Both the probe tip and the spinal cord surface were covered with mineral oil. The drawing is not to scale.

Because of the clearness of mineral oil, the height of 575 microns would not generate any significant difference between the current study and the previous results obtained (Johns et al., 2003 a, b).

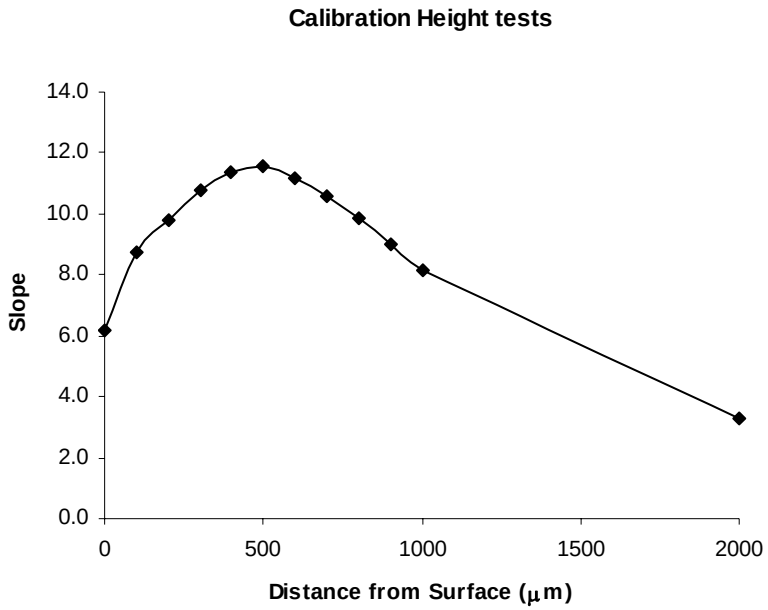

Figure 2.3: Calibration curve to determine optimal distance. This distance determines the separation between the probe tip and surface of the tissue.

2.2.1.3 Data acquisition and analysis

The optical reflectance were recorded from three regions of the exposed rat spinal cord, i.e. left lumbar, right lumbar, and the blood vessel running near the center of the cord. From each region, the data were recorded at 1 mm intervals rostrally starting from LL5. Data were taken at 1 Hz sampling rate with an integration time of 60 ms for a period of 60 seconds at each point. The raw reflectance data were firstly converted to the spectral slope values between 700 nm - 850 nm without calibration, followed by further processing to quantify the reduced scattering coefficient, μ_s', using a calibrated spectrum taken from the standard reflectance (WS–1, Diffuse Reflectance Sample, Ocean Optics, Inc., Dunedin, FL).

The goal of this set of measurements was (a) to show a heterogeneous map of light scattering in the region of rat spinal cord, and (b) to quantify μ_s' values of the rat

spinal cord. For purpose (a), an interpolated gray scale map of the slope values was obtained using Matlab®. Specifically, the slope values at each point were firstly averaged over the sixty seconds, and then the adjoining points were interpolated to generate a smoothed image. For purpose (b), we utilized our newly developed algorithm (Johns et al., 2003 a, b) to determine μ_s' values of the rat spinal cord based on the needle-probe reflectance readings as explained in Section 1.3.

2.2.2 Materials and Methods for Sciatic Nerve Measurements

2.2.2.1 Spinal Nerve Ligation

We used the modified spinal nerve ligation model (Kim and Chung, 1992) to induce demyelination in the sciatic nerve. The difference between the model and our procedure is that we ligated the L4 and L5 spinal nerves and not L6. Demyelination and degeneration should occur following the spinal nerve ligation.

On the day of ligation, the rats were anesthetized with isoflurane in 100% oxygen (3% induction, 2.25% maintenance) and placed in the prone position to access the left L4–L6 spinal nerves. Care was taken to ensure that all reflexes (tail pinches and eye-blinks) were eliminated. Under magnification, approximately one third of the transverse process was removed. The *left* L4 and L5 spinal nerve were identified and carefully dissected free from the adjacent tissue. Spinal nerves of three different groups (L4 only, L4 and L5, and L5 only, n = 28 in each group) were then tightly ligated using a 6–0 silk suture followed by a transection distal to the ligation. The wound was treated with an antiseptic solution of Betadine, the muscle layer was sutured, and the incision was closed with wound clips. The animal was kept in their habitual environment till the day of the experiment. More details on postoperative care can be found elsewhere (Senapati et al.,

2005). All the experimental procedures follow the guidelines of International Association for Study of Pain (Zimmermann, 1983) and approved by the IACUC of the University of Texas at Arlington.

2.2.2.2 Subjects and surgical methods

Animals of each spinal nerve ligation group were further divided into 4 subgroups based on the postoperative day (i.e. 1, 4, 7, or 14 days). The rats were initially anesthetized with sodium pentobarbital (50 mg/kg, i.p., supplemented as necessary). A 3 cm incision was made from the gluteal region to the middle of the thigh. The muscle was carefully dissected to expose 2.0 – 2.5 cm of the sciatic nerve on both sides. Tracheotomy was done and a cannula was inserted into the trachea to connect it to the artificial respirator as a precaution at times of abnormal respiration. Intra-jugular cannulation was done to allow for continuous anesthesia (1.2 ml/hr, 0.5% sodium pentobarbital). Animals were then placed on the stereotaxic frame. Mineral oil was used to prevent the drying of the exposed surface. The body temperature was kept at 37°C using a heating blanket with a feedback control unit (Harvard Apparatus, Inc., Holliston, MA). The vital signs including heart rate (360 beats/min.), respiration rate, partial pressure of carbon dioxide (PCO_2 = 25 - 30 mmHg) were continuously monitored. After the experiment animals were euthanized by intracardial injection of sodium pentobarbital.

2.2.2.3 Experimental set up

A similar experimental set up to the one for the spinal cord measurements (Section 2.2.1.2) was used for the sciatic nerve measurements. The optic fiber probe was placed on the distal region of the sciatic nerve of the rat mounted on the stereotaxic

frame. The probe tip was held perpendicularly at a height of 575 microns above the sciatic nerve (Fig. 2.1).

2.2.2.4 Data Acquisition

The measurements were taken on the left (ligated) and right (control) sciatic nerves: on each side, 5 readings were taken starting from the distal side. Similar to the procedures used for the spinal cord readings, the data were recorded for a period of 60 seconds at each point at a 1 Hz sampling rate with integration time of 60 ms. We quantified the slope values for relative comparison between ligated and control nerves, and the slope differences are reported as Mean ± Standard Error of Mean. In statistical analysis, in order to show the differences in light scattering between the ligated and control side, we performed a paired t-test with a confidence level of 95 %.

2.3 Experimental Results

2.3.1 Results from the Spinal Cord Measurements

Using the experimental protocols and data processing procedures, we generated gray scale maps of the light scattering index, i.e., the slope values, of the spinal cord near left L5.

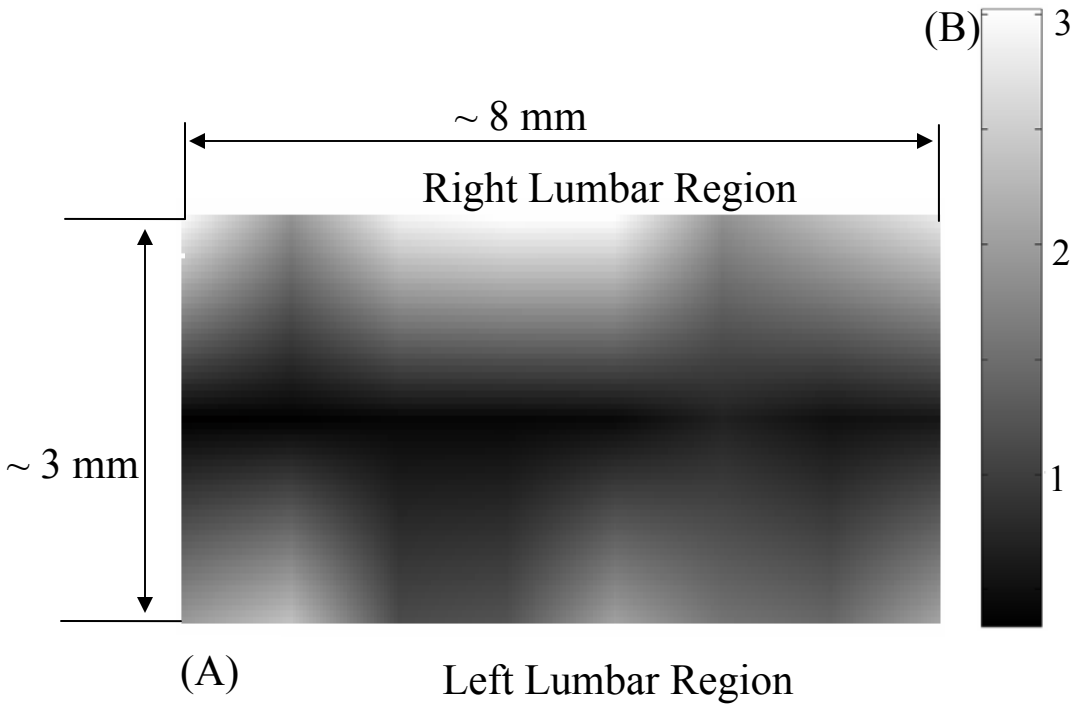

Figure 2.4: Example of spectral slope map. (A) A spectral-slope map with its gray scale bar (B) to show differences in spectral slope of the rat spinal cord. The dark region, representing lower slope values, at the center corresponds to the location of the blood vessels; the lighter regions, representing larger slope values, are the lumbar regions of the spinal cord. The example map is taken from a single rat in experiment No. 6.

Figure 2.4(A) shows one example of the maps: the darker regions on the map show lower scattering (with smaller slope values), while the lighter regions show more scattering. The region with lower slopes (0.34 to 0.67) at the center corresponds to a blood vessel; on the spinal cord per se, the slope values read between 1.12 and 3.02. Figure 2.4(B) shows the gray level bar for the map. Furthermore, Figure 2.5 shows a summarized map of the rat spinal cords taken from all slope values of the 14 rats, and this map has similar aspects to those explained for Figure 2.4.

Table 2.1 Average values of slope on the spinal cord

No:	Left Lumbar	Blood Vessel	Right Lumbar
1	0.830	0.477	0.809
2	1.069	0.808	1.770
3	1.129	0.562	1.163
4	1.118	0.773	1.016
5	1.451	0.867	1.305
6	1.704	0.463	2.597
7	0.888	0.368	1.448
8	1.309	0.452	1.568
9	1.003	0.571	1.055
10	2.425	0.987	1.990
11	2.258	0.352	1.644
12	0.816	0.247	0.501
13	1.244	0.272	1.563
14	2.771	0.480	2.054
Mean	**1.430**	**0.549**	**1.463**
Std. Dev.	**0.628**	**0.228**	**0.547**

From Table 2.1, the blood vessel region near the center shows a slope value of 0.55±0.23, while the rest of the mapped regions on either side of the central blood vessel have slope values ranging from 1.45±0.5. We have performed several t-tests to study the light scattering characteristics on the spinal cord. The left and right lumbar regions showed no significant difference in slope values ($p = 0.80$), while a significant difference existed between the lumbar regions (both left and right) and the central area where the blood vessels were ($p << 0.001$).

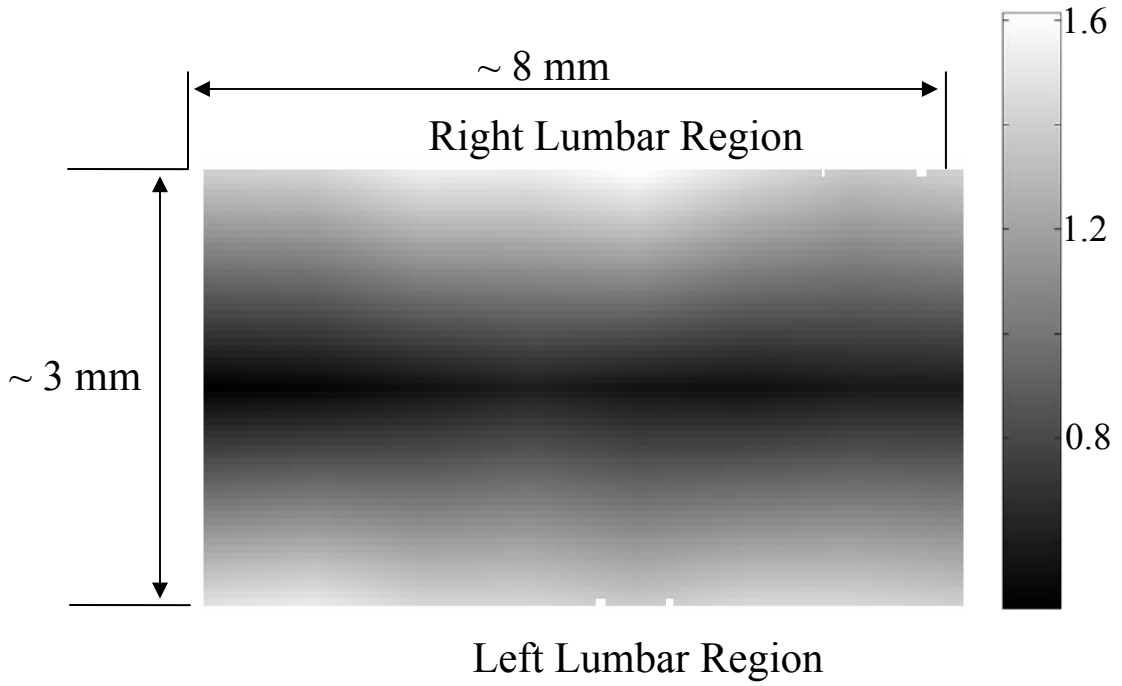

Figure 2.5: Average spectral slope map. (A) A slope map with its gray scale bar (B) to show the average values of slope taken from 14 rats.

The more meaningful and quantitative parameter to show tissue properties is the reduced scattering coefficient, μ_s'. Figure 2.6 shows a plot of μ_s' values at 750 nm from one rat, which are obtained using eq. (1.3).

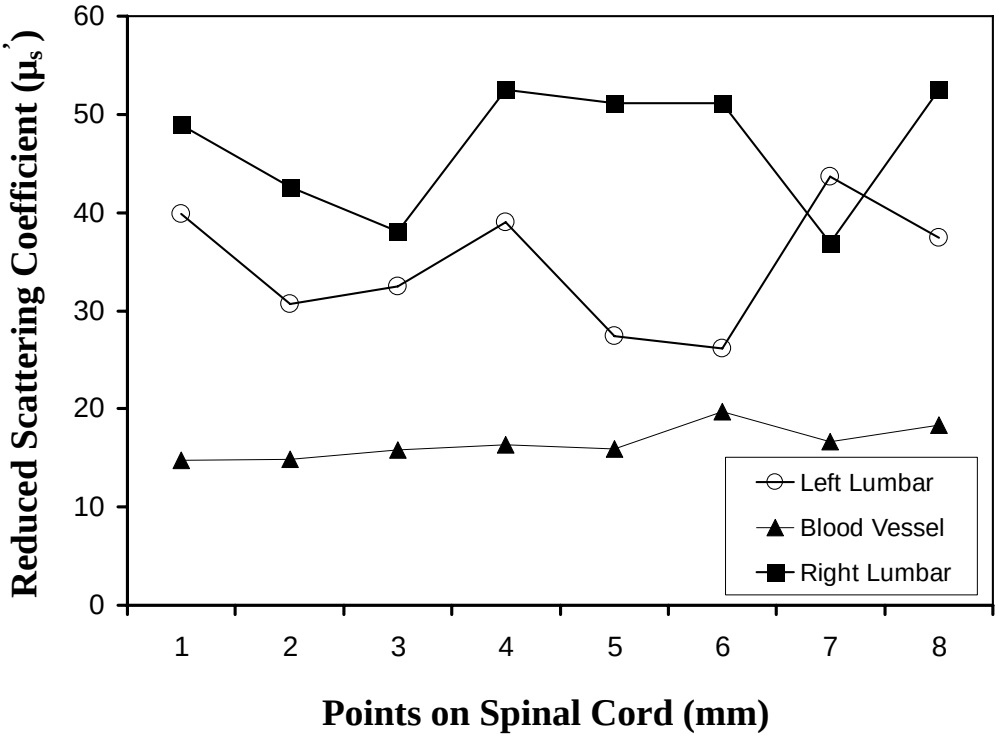

Figure 2.6: A plot to show variation in μ_s'. The values are from the left, right, and central lumbar regions of the spinal cord. The μ_s' values are computed at 750 nm with the unit of cm^{-1}. The example map was obtained from a single rat in experiment No. 6.

Pooling the relative groups of data together leads to 40.4±2.2 cm^{-1} for the lumbar regions (left and right together since there is no significant difference between them) and 17.3±0.7 cm^{-1} for the central blood vessel region. If the data from the 14 rats is considered, we have obtained 34.2±2.1 cm^{-1} and 19.9±1.0 cm^{-1} as slope values for the lumbar regions and the central region containing the blood vessels, respectively. It is evident that the values of μ_s' are much higher in the nervous regions than the blood vessels.

Table 2.2: Average values of μ_s' on the spinal cord

Sl No:	Left Lumbar	Blood Vessel	Right Lumbar
1	23.507	17.633	21.528
2	26.841	20.577	34.175
3	24.430	18.255	25.211
4	32.404	25.126	28.297
5	47.205	21.556	29.469
6	34.567	16.574	46.721
7	23.970	16.098	30.701
8	29.590	17.372	32.332
9	25.461	20.376	25.937
10	56.007	30.186	46.875
11	50.832	17.962	37.389
12	26.889	16.869	21.247
13	30.161	18.253	37.747
14	59.785	21.730	47.402
Mean	**35.118**	**19.898**	**33.216**
Std. Dev	**12.720**	**3.876**	**8.993**

It is known that the raw reflectance spectra of brain tissue between 700 nm - 850 nm are nearly linear with the maximum located at 700 nm. Thus, the spectral slopes of tissue reflectance have been used as an index to mark light scattering. Eq. (1.3) also clearly indicates that the reflectance is highly correlated with μ_s'. Figure 2.7(A) plots average values of μ_s' map taken from the 14 rats.

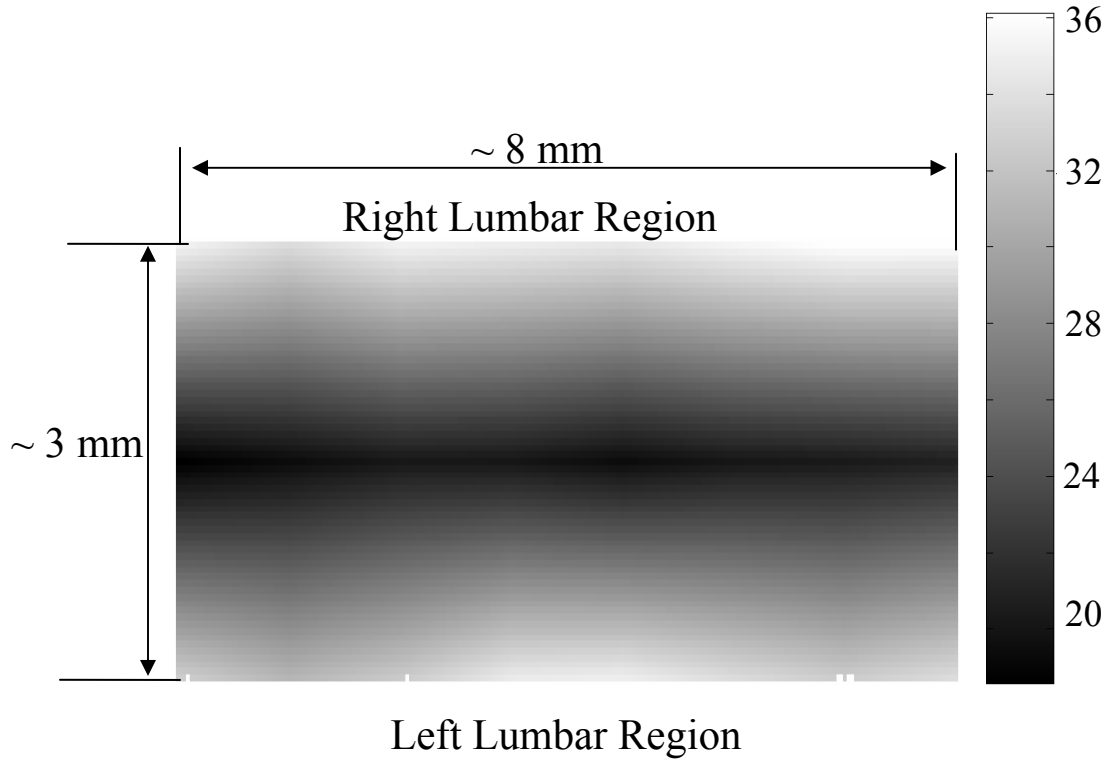

Figure 2.7: Average μ_s' map. (A) μ_s' value map with its gray scale bar (B) to show the average values of μ_s' (in cm^{-1}) in the lumbar regions of the spinal cord, taken from 14 rats.

The similarity seen in Figures 2.5(A) and 2.7(A) demonstrates that the two indices, i.e., the slope and μ_s', can be used as a marker to differentiate levels of light scattering on the spinal cord. Similarly, a t-test shows that a significant difference in μ_s' values exists only between the lumbar regions (both left and right) and the central blood vessel area ($p << 0.001$).

2.3.2 Results from the Sciatic Nerve Measurements

Eighty-four rats were divided into three groups based on the left spinal nerve ligation (n = 28 in each group): L4 only, L4 plus L5, and L5 only. Each group was further

divided into four subgroups based on the postoperative day (n = 7 in each subgroup): 1, 4, 7, and 14.

Representative traces collected from the NIR spectroscopy are shown below. They represent three different left sciatic nerve ligation groups, i.e.; Figure 2.8 for L4 ligation only, Figure 2.9 for L4 - L5 ligation, and Figure 2.10 for L5 ligation only on postoperative day 4. In each case, the overall intensity (arbitrary unit) from the left sciatic nerve (ligated, in gray trace) was lower as compared to the one from the right sciatic nerve (normal, in black trace). The intensity within the wavelength range of 700-900 nm was also lower in the left sciatic nerve.

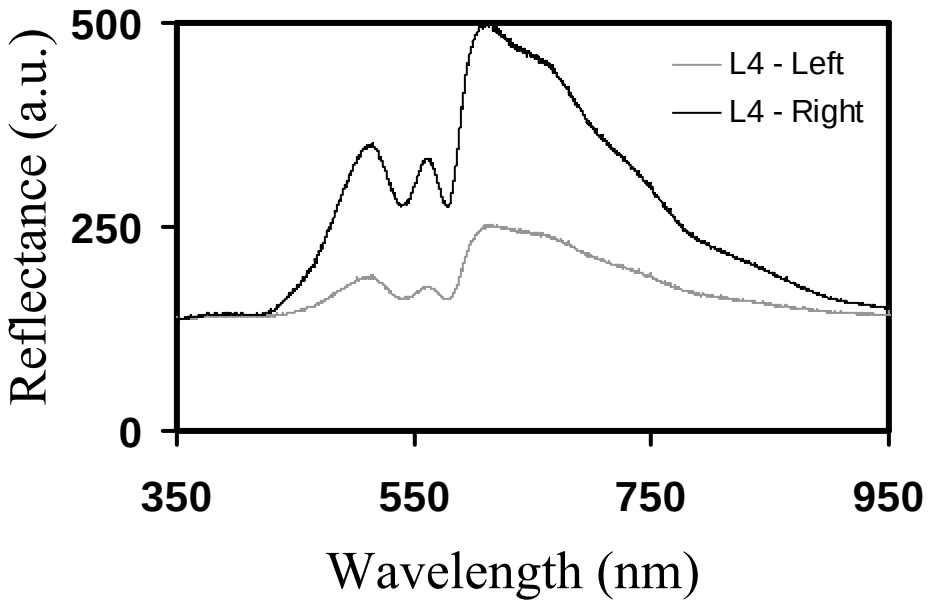

Figure 2.8: Spectral traces on PO4 after L4 spinal nerve ligation only

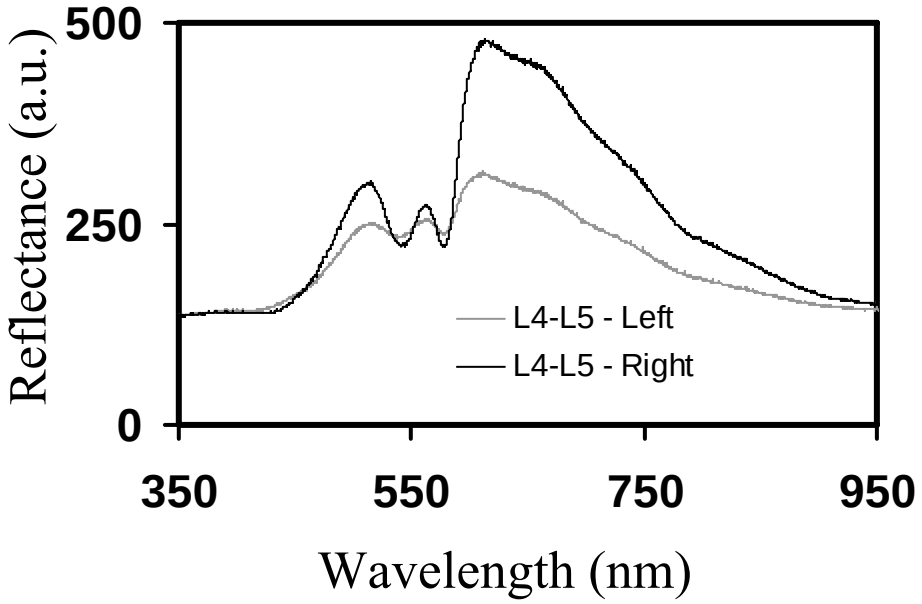

Figure 2.9: Spectral traces on PO4 after L4-L5 spinal nerve ligation

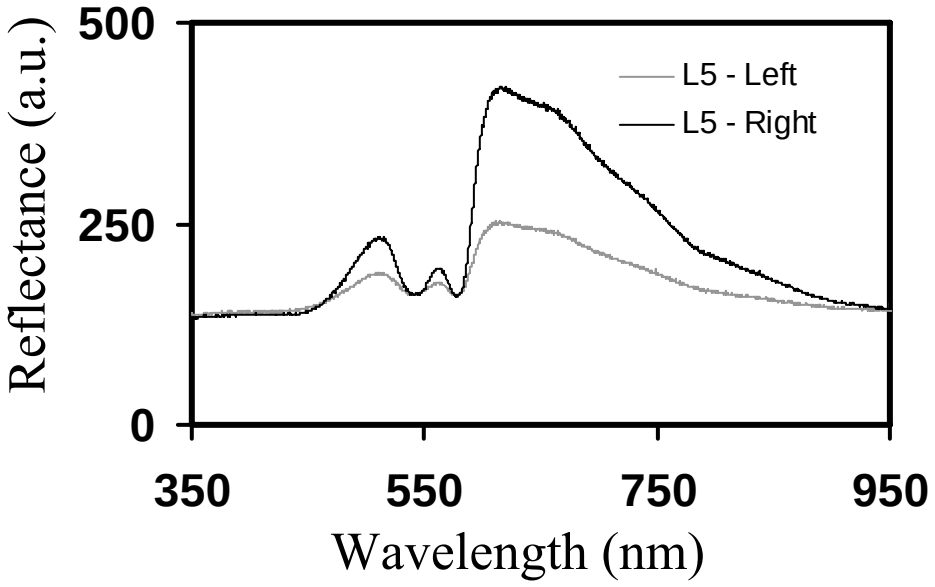

Figure 2.10: Spectral traces on PO4 after L5 spinal nerve ligation only

There was no statistical difference in the slope values among five spots along the sciatic nerve where readings were taken. Therefore, 5 data points were pooled to get the average slope value for one sciatic nerve. These are shown in Table 2.3 and plotted in Figure 2.11 for L4 ligation only, Figure 2.12 for L4-L5 ligation, and Figure 2.13 for L5 ligation only.

Table 2.3: Average slope values for different types of ligation.

	Slope Values					
	L4 Ligation		L4-L5 Ligation		L5 Ligation	
PO Day	Ligated Side	Control Side	Ligated Side	Control Side	Ligated Side	Control Side
1	1.01 ± 0.10	0.99 ± 0.20	0.72 ± 0.10	0.74 ± 0.06	0.83 ± 0.10	0.78 ± 0.06
4	0.46 ± 0.03	0.83 ± 0.12	0.57 ± 0.05	0.91 ± 0.12	0.46 ± 0.07	0.96 ± 0.09
7	0.64 ± 0.06	0.92 ± 0.21	0.62 ± 0.05	1.05 ± 0.08	0.59 ± 0.04	0.80 ± 0.10
14	0.55 ± 0.05	0.80 ± 0.09	0.84 ± 0.19	0.88 ± 0.16	0.38 ± 0.04	0.58 ± 0.13

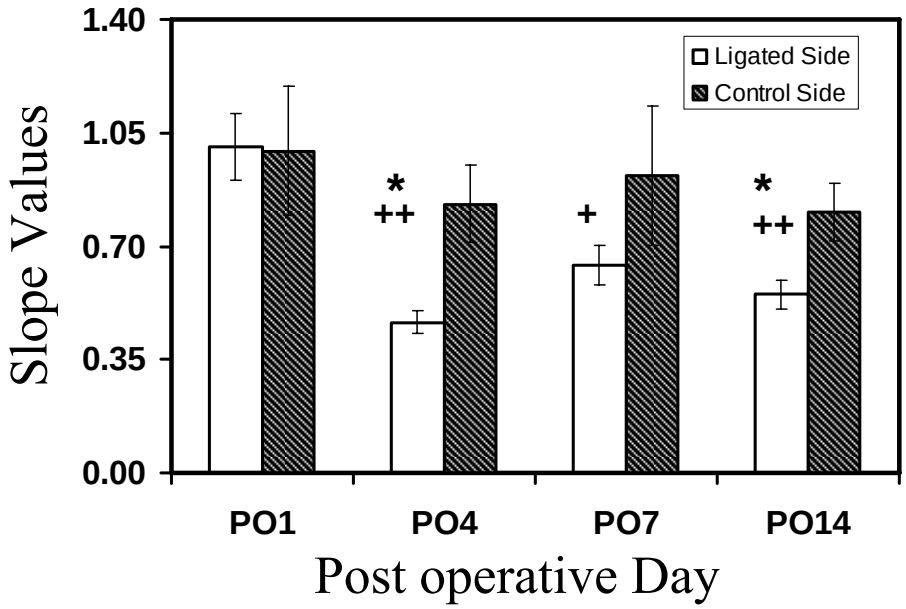

Figure 2.11: Summary of slope values due to L4 ligation only. * indicates significant difference between ligated and control sides; + indicates significant difference as compared with PO1 on the ligated side; no significant difference among control side. Error bars indicate SEM.

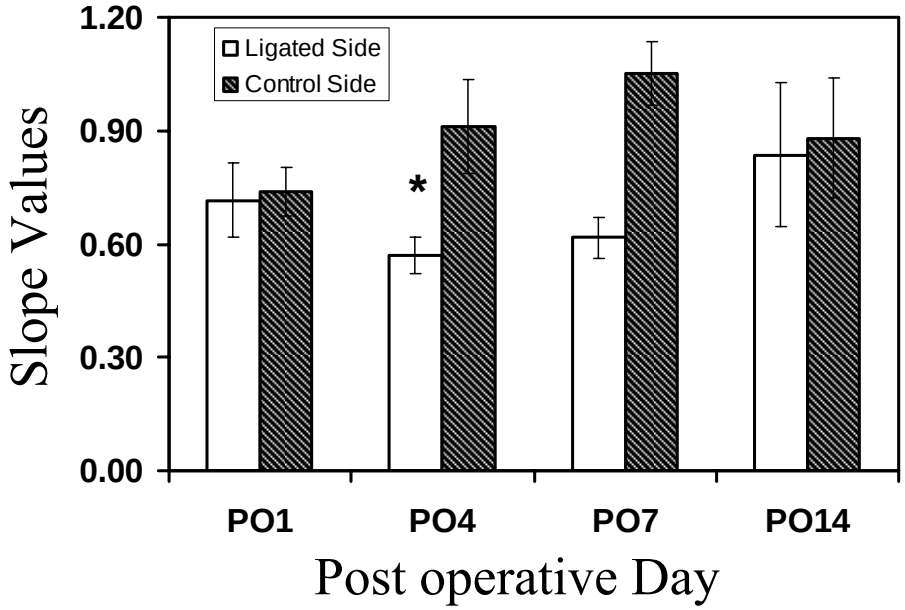

Figure 2.12: Summary of slope values due to L4-L5 ligation. * indicates significant difference between ligated and control sides; no significant difference among control side. Error bars indicate SEM.

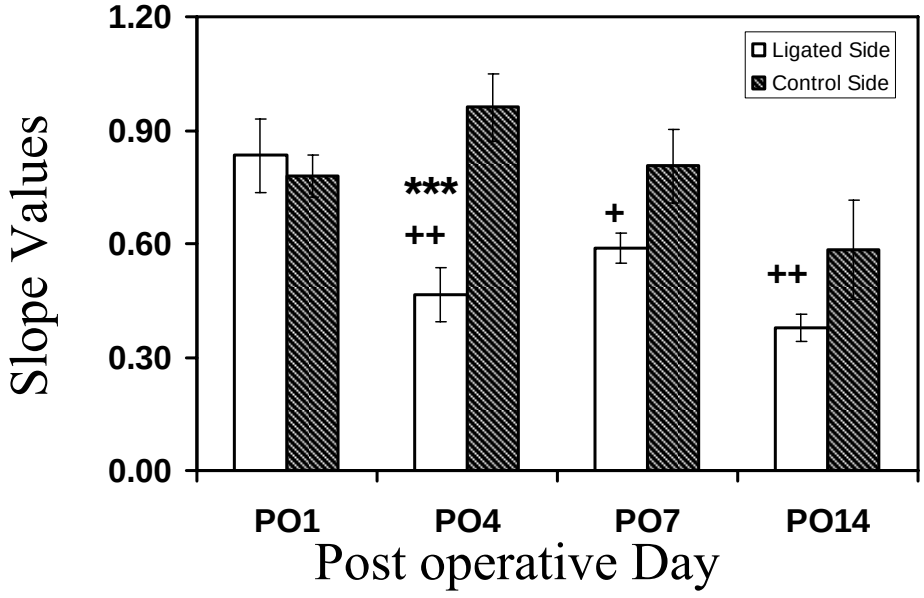

Figure 2.13: Summary of slope values due to L5 ligation only. * indicates significant difference between ligated and control sides; + indicates significant difference as compared with PO1 on the ligated side; no significant difference among control side. Error bars indicate SEM.

This procedure resulted in three dependent variables: type of ligation, side of ligation, and days after ligation. They all have potential influence on the scattering properties of the nerve. Statistical analysis by ANOVA showed no difference among different types of ligation. Therefore, data can be collapsed under types of ligation variable.

Analysis of Variance showed that there were significant differences between left and right side of the sciatic nerves, and among the postoperative days (Figure 2.14). The slope values for the left sciatic nerve at postoperative day 1, 4, 7, and 14 are 0.85±0.06, 0.51±0.03, 0.62±0.03, and 0.58±0.07, respectively. The slope values for the right sciatic nerve at postoperative day 1, 4, 7, and 14 are 0.82±0.07, 0.88±0.06, 0.91±0.09, and 0.76±0.08, respectively.

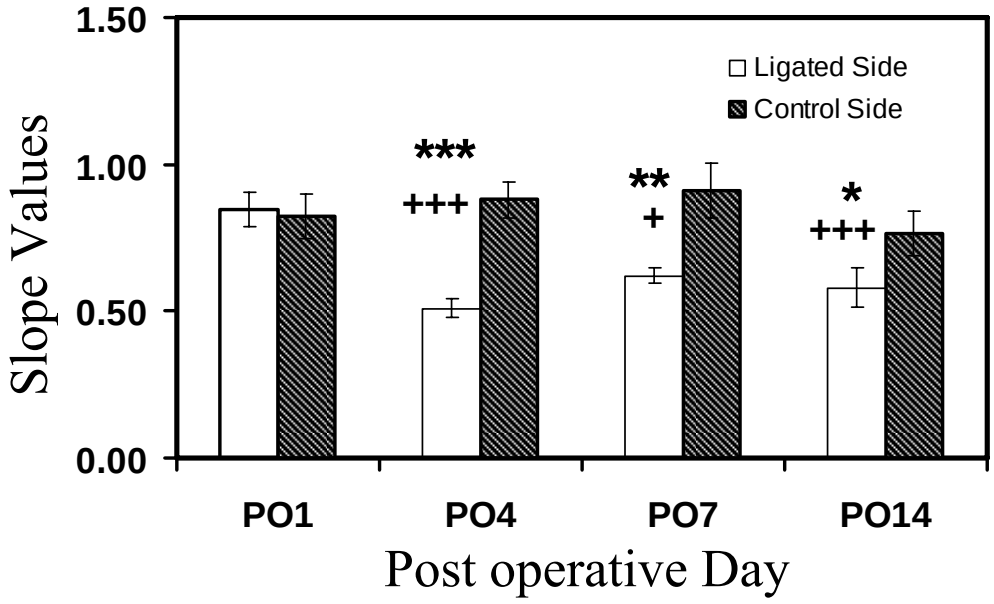

Figure 2.14: Statistical summary of slope values. The scattering properties of the left sciatic nerve are significantly lower than the right side on postoperative day 4, 7, and 14 (*). The scattering properties of the left sciatic nerve on postoperative day 4, 7, and 14 are significantly lower than day one (+).

There was no significant difference between the left and right on postoperative day one. Slopes of the left sciatic nerves were significantly lower than those of the right side (n=21) on postoperative day 4 ($p < 0.001$), day 7 ($p < 0.01$), and day 14 ($p < 0.05$). There were no statistical significant changes for the right sciatic nerves along the course of postoperative days. However, significantly lower slope values of the left sciatic nerves were found on postoperative day 4 ($p < 0.001$), day 7 ($p < 0.05$), and day 14 ($p < 0.001$) as compared to day one.

2.4 Discussion

The primary goal of this study was (1) to quantify the reduced scattering coefficient, μ_s', of the rat spinal cord intraoperatively and (2) to determine if the optical reflectance and the μ_s' values could be used to differentiate healthy and demyelinated nerves connected directly to the rat spinal cord. We will discuss the two kinds of measurements separately first, followed by a joint discussion to address common issues and future work.

2.4.1 Discussion on the Spinal Cord Measurements

The results from the spinal cord measurements have shown that the quantified μ_s' values are most likely in a range of 34.2±2.1 cm^{-1} in the lumbar regions and 19.9±1.0 cm^{-1} near the blood vessels at the center of rat spinal cord. Such differences in μ_s' are expected due to the variations of anatomical and hemo-physological structures around the spinal cord. Larger scattering signals detected on the lumbar regions of the spinal cord are an indication of the abundance of white matter present in those regions. It has been shown that the μ_s' values of gray and white matter in the human brain are in the range of

30 ± 12 cm^{-1} and 80 ± 10 cm^{-1} respectively, (Johns, 2003) while for the rat brain the μ_s' values range from 15 to 61 cm^{-1} (Gurnani, 2003). Thus, the μ_s' results of the rat spinal cord reported here are consistent with the previous finding for the rat brain.

There have been a large number of studies using NIR spectroscopy on the assessment of hemoglobin and other chromophore concentrations. Such kind of studies can mostly be benefited if the corresponding μ_s' values are known. Since the optical measurements of tissues are strongly influenced by both light scattering and absorption, quantification of light scattering will help decouple light scattering from absorption, leading to better interpretation on the optical measurements of tissue and their physiological responses to various stimulations.

On the other hand, because of the limitation of fiber optic mapping, the spatial resolution of the scattering coefficient maps is low, lower than what we expected. A possible way to improve the spatial resolution of light scattering mapping is to utilize a CCD camera and to take reflectance images at multiple selected wavelengths. Then, the algorithm to obtain μ_s' maps of the measured tissue has to be developed and validated accordingly. While we expect that our existing algorithm for the fiber optic probe could be modified and adapted for the CCD camera approach, we need further investigation to validate our expectation.

2.4.2 Discussion on the Sciatic Nerve Measurements

The sciatic nerve measurements have demonstrated that light scattering from the spinal nerves correlate well with the pathological changes, i.e., demyelination, following peripheral nerve injury. Light scattering in the sciatic nerve depends mainly on the presence or absence of myelin and some other components that might alter the degree of

scattering. A higher slope or μ_s' value shows more scattering due to the presence of myelin, and a lower slope or μ_s' value results from the lack or decrease of myelin. It is known that damage to nerves (e.g., tight ligation and transection) will induce axonal degeneration at the distal part because of lack of nutritional supply from the cell body. Similarly, ligation and transection of the spinal nerve will lead to degenerative processes distal to the site of lesion. Although it is known that at 36 - 48 hours after ligation, myelin breaks down, and at 48 – 96 hours, there is a loss of axonal continuity (Lubinska, 1982; 1997), we were unable to show such change by the NIR technique on postoperative day 1. We speculated that early inflammatory processes in the sciatic nerve would contribute to the discrepancy on day 1. However, significant changes in light scattering were found on postoperative days 4, 7, and 14, correlating well with the pathological changes. Moreover, the idea that variations in light scattering may be used to identify intraoperatively possible diseases of the spinal cord is novel, and our preliminary finding encourages further exploration in this direction.

2.4.3 Joint Discussion on Common Issues

A close look at the cross sectional view of the lumbar region shows a larger H-shaped gray matter area compared to the thoracic spinal cord. A common question often to be asked is how deep into the white matter we are able to detect, or if we are able to reach gray matter by fiber optic reflectance measurement. To answer this question, we need to address the 'Look-Ahead Distance' (LAD) for the probe used in the study. Our previous study has demonstrated that LAD is shown as a function of μ_s' and is approximately around 1.0 to 1.5 mm for the current probe (Giller et al., 2003; Gurnani, 2003; Qian et al., 2003) with μ_s' values in the range of 4 to 35 cm^{-1}. The diameter of

segments of the lumbar region is about 4 mm (Fig. 1), and the white matter that covers the dorsal horn is about 0.5 mm thick. Taking these values into account, if light was to travel 1.1 mm from the surface of the spinal cord/nerve, it is possible that the fiber optic reflectance may reach gray matter. Variation highly depends on the local anatomy of the spinal cord and dorsal roots. We have not addressed this issue in the current study, and further research could be conducted in this direction.

Further inspection on the measured data reveals that there exists a certain variation in the data, which is one of the drawbacks of the technique. Imaging by point measurement in the spinal cord is highly variable as there is no standard measure to assure the placement of probe to be at the same point for all experiments. For the spinal cord, subject-to-subject variability could be attributed to various factors, such as anatomical variation of the spinal cord, position of dorsal roots when they enter the spinal cord, number and site of branching of the blood vessel, and slight body movement due to respiration. All these factors played a certain role in causing variability. For the sciatic nerve measurements, the variability could result from probe localization, animal body movements, tension of the sciatic nerve, and inhomogeneous demyelination. While we have not provided any histology support to our findings as it requires the use of trained personnel, our evidence of demyelination induced by ligation lies in the numerous published reports (Mira, 1976; Lubinska, 1982; Clemence et al., 1989; Lubinska., 1997). Histological evidence for demyelination shall be provided in our future research report.

While numerous studies have focused on light scattering properties of the brain, there is still a large discrepancy of light scattering coefficients taken between in vivo and in vitro, particularly for μ_s' values of white matter. Most common values of μ_s' for the

human brain reported through non-invasive, in vivo methods (Hueber et al., 2001; Fukui et al., 2003; Choi et al., 2004) are within 10-20 cm^{-1}, whereas those of μ_s' reported through in vitro measurements (Cheong et al., 1990; van der Zee et al., 1993; Taddeucci et al., 1996; Schwarzmaier et al., 1997; Yaroslavsky et al., 2002) are in the range of 40-100 cm^{-1}. We attribute the reason of having such large disagreement to the following factors: 1) the non-invasive *in vivo* measurements using the photon migration approach actually include all the signals from the scalp, skull, and gray matter, resulting in a mean of optical properties of multi layers. 2) In the case of invasive measurements, it is lack of validated algorithms to quantify μ_s' when a limited tissue volume is measured with a limited source-detector separation. It has been previously shown by our group that the μ_s' values of gray and white matter in the human brain is in the range of 30 ± 12 cm^{-1} and 80 ± 10 cm^{-1}, respectively (Johns, 2003), while the μ_s' values from the rat brain (Gurnani, 2003) range from 15 to 61 cm^{-1}. The μ_s' values of the rat spinal cord and sciatic nerves given in this study are highly consistent with those reported values. The primary aim of this study was to investigate light scattering from the spinal nerves and to explore if light reflectance can be used to detect nerve/spinal cord demyelination. The NIR reflectance technique is minimally invasive, low-cost, and portable, and it can be used *in vivo* without requirement of separating nerves and spinal cord from the surrounding tissue.

CHAPTER 3

DETERMINATION OF OXYGEN SATURATION IN RAT SCIATIC NERVE DUE TO DEMYELINATION

3.1 Introduction

3.1.1 Near infrared spectroscopy versus visible spectroscopy

Non-invasive optical imaging has seen tremendous growth and development since the time it was shown that hemoglobin and oxygen saturation information could be obtained in the near-infrared (NIR) region due to the semi-transparency of the biological tissues in that region (Jobsis, 1977) and then subsequently used for measurement of *in vivo* cerebral metabolism (Wiensperger et al., 1981), cerebral blood flow (Colacino et al., 1981), brain oxygenation (Mook et al., 1984), and other chromophores (Karimanet al., 1983). The use of this modality has since grown towards measurements in the brain (hebden et al., 2003; Strangman et al., 2002), breast (Pogue et al., 2001; Duduran et al., 2002), and skin (Soyemo et al., 2005). Later reports have shown that NIR spectroscopy could be used effectively to determine spinal cord oxygenation (Macnab et al., 2002; Germon, 2002). Our recent studies have determined the optical properties of the rat spinal cord and also demonstrated the use of NIR in distinguishing healthy and ligated nerves using light scattering and reflectance as an index (Senapati et al., 2005; Radhakrishnan et al., 2005).

With a different spectral analysis, this study focuses on determination of oxygen saturation in the peripheral nerves of rats. We shift our spectral hemoglobin window from the scattering dominant NIR region to the absorption dominant visible region between 500 nm – 600 nm. Numerous reports on hemoglobin oxygen saturation obtained in the visible range have been published (Doppenberg et al., 1997; Schweitzer et al., 1999; maxim et al., 2005) since vascular oxygen saturation can be a suitable index for quantifying pathological alterations. Our aim here is to show variations in oxygen saturation between normal and demyelinated nerves in rats. We hypothesize that there is a significant reduction in hemoglobin oxygen saturation in the ligated nerve as compared to a healthy peripheral nerve. In this study, we introduced demyelination using the modified spinal nerve ligation model in rats (Kim and Chung, 1992) and used an algorithm developed previously by our group (Johns et al., 2001) to finally prove our hypothesis.

3.2 Methods and Materials

Details of type of subject, surgical methods, experiment set up and data acquiaition methods are explained in Section 2.2.2.

3.2.1 Data analysis

3.2.1.1 To obtain Calibrated Reflectance Data

According to the algorithm (Johns et al., 2001), the raw reflectance data taken from the rats need to be calibrated in order to quantify their hemoglobin oxygen saturation values. The reflectance data were divided by the calibration spectrum taken from the standard reflectance sample. The calibrated spectra were then normalized at

500 nm so that the processed experimental readings from rats at 500 nm would have a value of unity (Johns et al., 2001).

3.2.1.2 To determine hemoglobin oxygen saturation (SO_2):

The algorithm to determine hemoglobin oxygen saturation values is given in Section 1.4.

3.2.1.3 Statistical analysis:

The data reported in this study is the hemoglobin oxygen saturation in the sciatic nerve of the rat. A set of sample traces obtained from the animal measurements is shown in Figure 3.1 to demonstrate the differences in oxygen saturation between control and ligated nerves. Five measurement points were taken on the sciatic nerve for each side – ligated (left) and non-ligated or control (right) side. The data were averaged across different groups, whenever statistically appropriate, and reported as mean ± SEM. Statistical significant differences were tested for different factors (ligated and non-ligated, sampling points along the sciatic nerve, types of ligation, and post-operative days) by ANOVA, followed by posthoc Tukey test. Significance was determined by $p<0.05$.

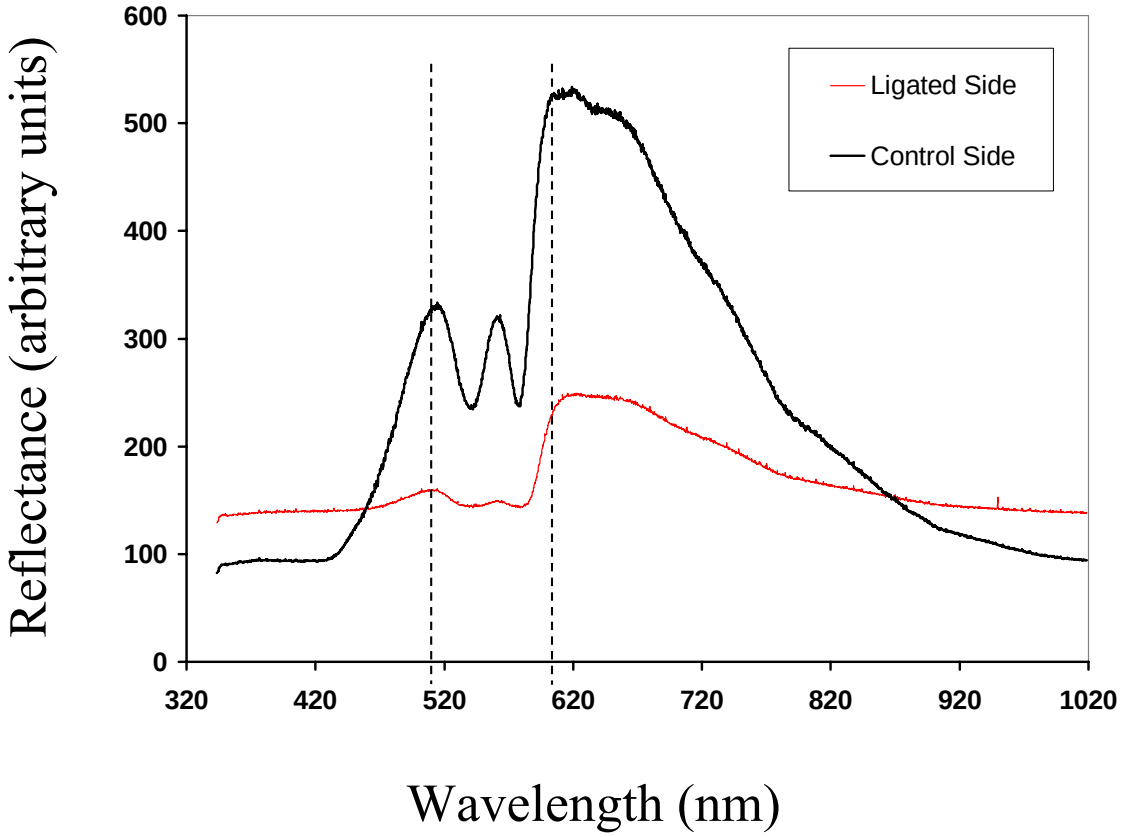

Figure 3.1: Representative traces obtained from a control and ligated sciatic nerve. The spectrum within the two dashed vertical lines indicates the 500 to 600 nm visible region.

3.3 Results

The study was done using eighty two Sprague-Dawley rats. They were divided into three groups (n = 28 in each group) based on spinal nerve ligated – L4, L4-L5, and L5. Furthermore, each group was sub-divided into four groups based on post-operative days – 1, 4, 7, and 14 days after ligation (n = 7 in each group).

Several representative traces of visible spectroscopy, normalized at their spectral peaks, are shown below. They represent three different groups of sciatic nerves L4 ligation only (Figure 3.2), L4 and L5 ligation (Figure 3.3), and L5 ligation only (Figure 3.4) on postoperative day 4.

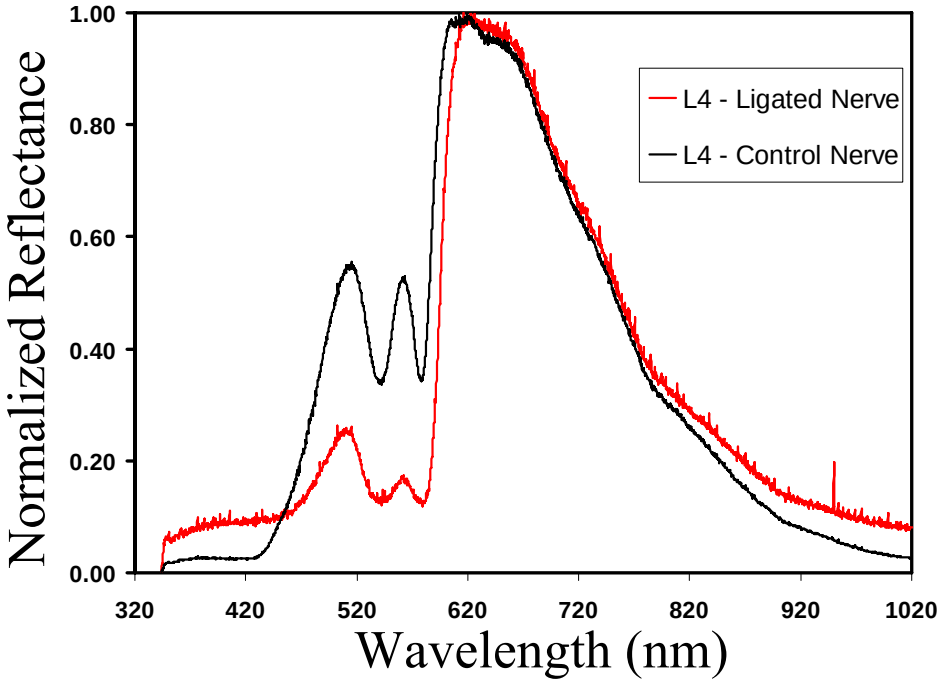

Figure 3.2: Spectral readings after L4 ligation only.

In each case, the normalized intensity (arbitrary unit) from the left sciatic nerve (ligated, in gray trace) was lower as compared with the one from the right sciatic nerve (control, in black trace). The depth in the double dip feature, or the "w" shape, in the 500 – 600 nm wavelength range is also lower in the left sciatic nerve. The 'w' shape is a qualitative indicator of saturation percentage. Higher saturation values have greater depth in the 'w' feature thereby indicating higher concentrations of oxygenated

hemoglobin, while a lower saturation percentage has a shallow ‘w’ or sometimes an absence of ‘w’, showing higher deoxygenated hemoglobin.

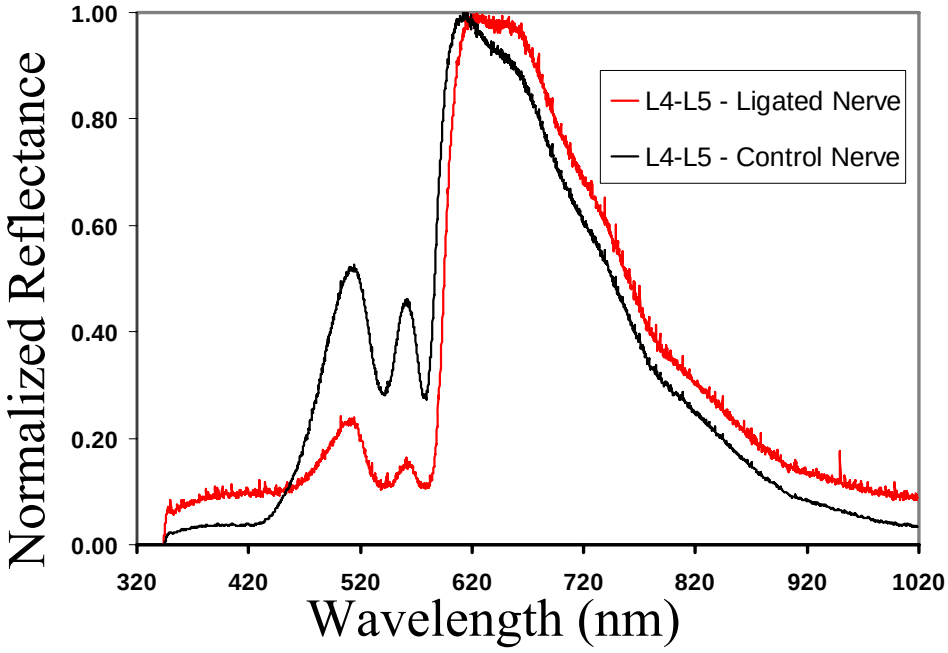

Figure 3.3: Spectral readings after L4-L5 ligation.

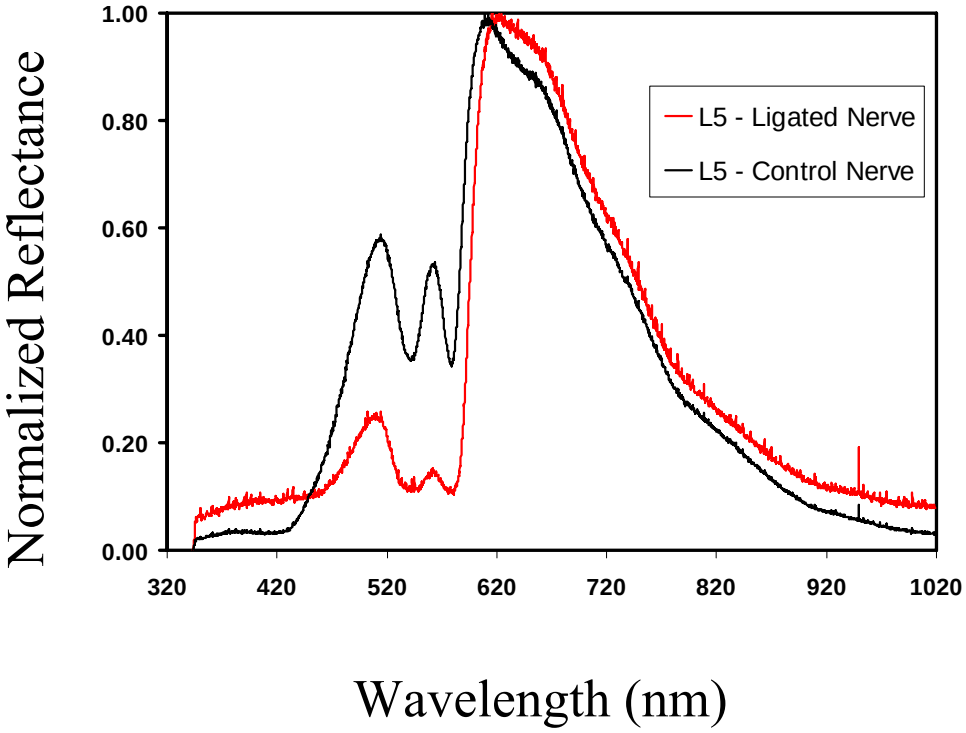

Figure 3.4: Spectral readings after L5 ligation only.

The factors that have the propensity to contribute to variations in oxygen saturation are the ligation type, ligation side, and the day of experiment after ligation. The measurements were taken at 5 points along the sciatic nerve, starting from the distal side of the sciatic nerve. Since we did not find any statistical difference among the five points, we have obtained an average value by pooling all the five values. These values are shown in Table 3.1.

Table 3.1: Average values of hemoglobin oxygen saturation for different types of ligation

	Oxygen Saturation Values					
	L4 Ligation		L4-L5 Ligation		L5 Ligation	
PO Day	Ligated Side	Control Side	Ligated Side	Control Side	Ligated Side	Control Side
1	66.22 ± 2.51	63.70 ± 2.50	63.61 ± 2.27	62.55 ± 2.95	56.41 ± 2.89	62.20 ± 3.22
4	46.11 ± 2.34	62.01 ± 2.49	47.08 ± 2.68	66.39 ± 2.98	40.98 ± 2.53	64.29 ± 2.45
7	50.77 ± 3.13	60.85 ± 2.39	48.38 ± 2.27	65.34 ± 2.52	48.41 ± 3.27	62.05 ± 2.99
14	38.07 ± 3.58	52.66 ± 3.91	50.09 ± 3.32	60.51 ± 2.55	38.77 ± 2.32	48.63 ± 3.47

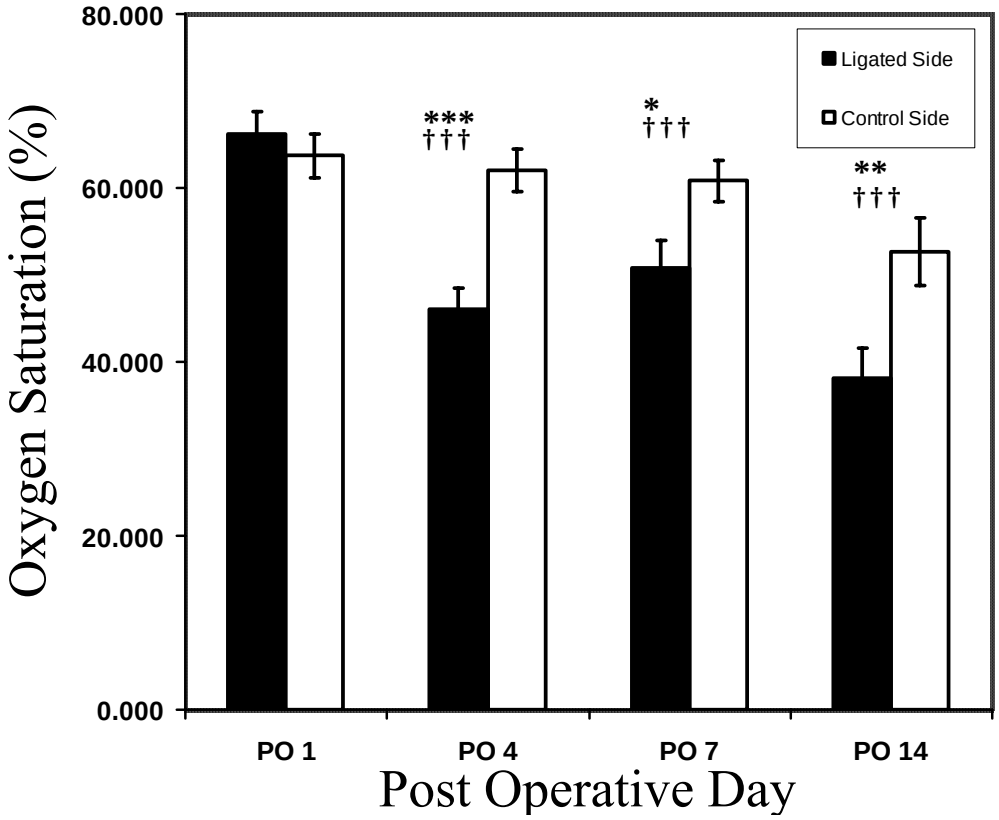

Figure 3.5: Summary of oxygen saturation values due to L4 ligation only. * indicates significant difference between ligated and control sides; + indicates significant difference as compared with PO1 on the ligated side; no significant difference among control side. Error bars indicate SEM.

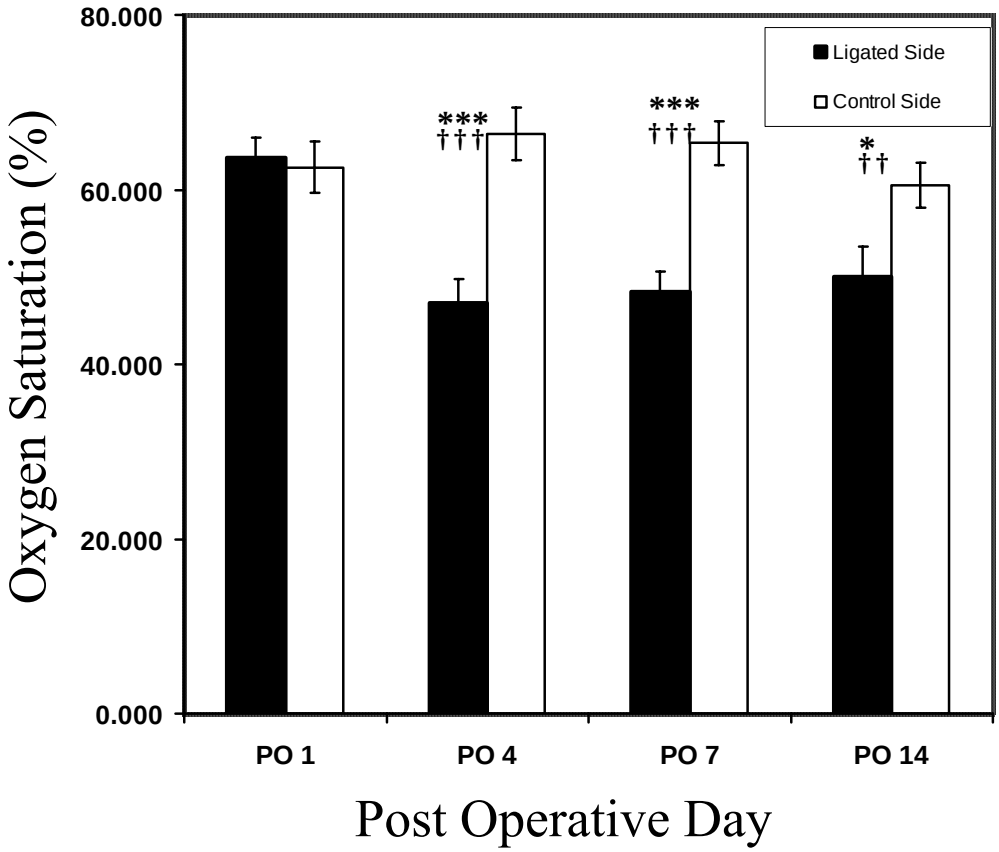

Figure 3.6: Summary of oxygen saturation values due to L4-L5 ligation. * indicates significant difference between ligated and control sides; + indicates significant difference as compared with PO1 on the ligated side; no significant difference among control side. Error bars indicate SEM.

Figures 3.2, 3.3, and 3.4 show the variation in oxygen saturation between the ligated side (L) and the control side (R) for the various ligation types. It is seen clearly from the plot that there is a significant decrease in hemoglobin oxygen saturation due to ligation on postoperative day 4. Figures 3.5, 3.6, and 3.7 show the average values of oxygen saturation on the ligated and control sides.

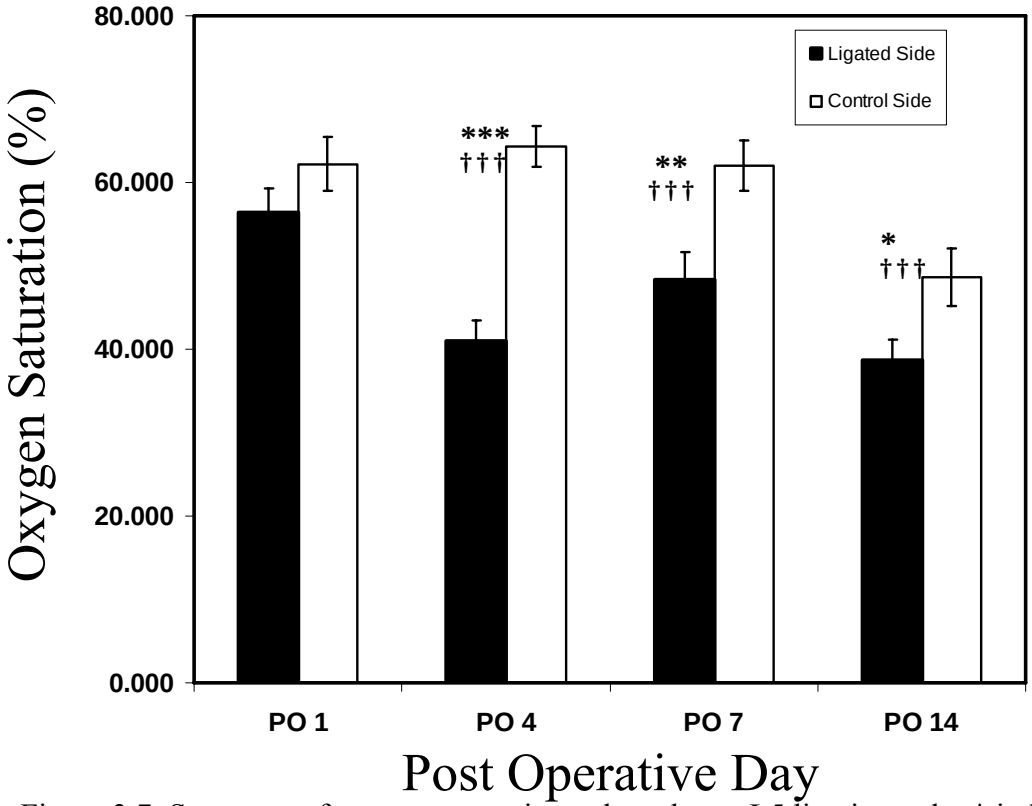

Figure 3.7: Summary of oxygen saturation values due to L5 ligation only. * indicates significant difference between ligated and control sides; + indicates significant difference as compared with PO1 on the ligated side; no significant difference among control side. Error bars indicate SEM.

The same observation or conclusion was held for postoperative days 7 and 14 when compared to the control side and also when compared to the ligated side on postoperative day 1, as shown in Figures 3.8 and 3.9.

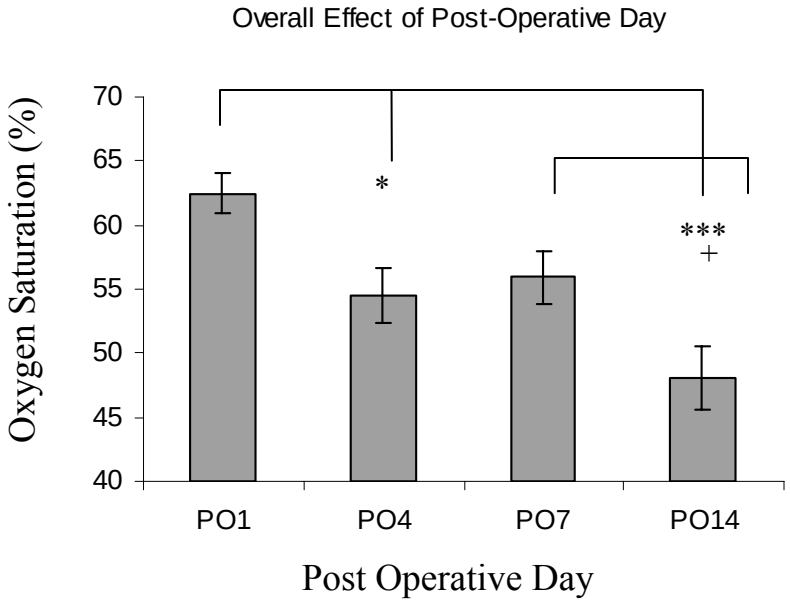

Figure 3.8: Overall effect of postoperative day. * indicates significant difference between PO1 and PO4 and PO14; + indicates significant difference between PO7 and PO14. N=42. Error bars indicate SEM.

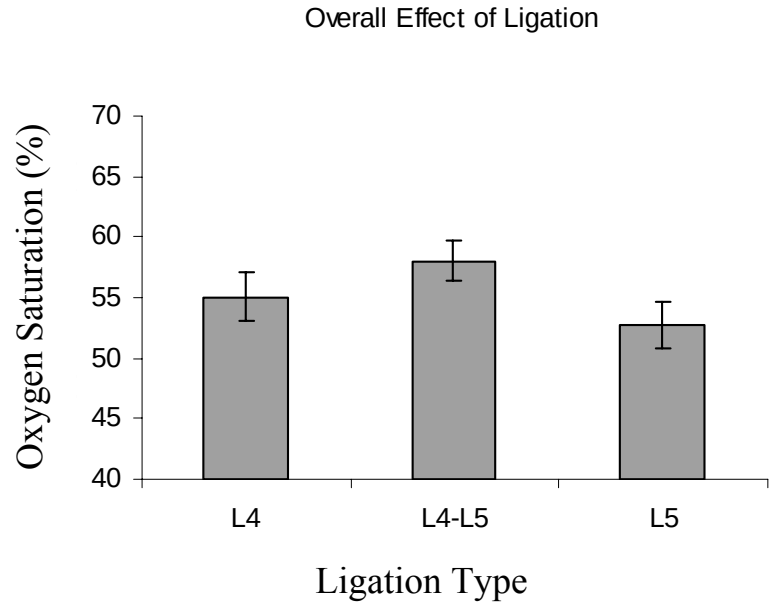

Figure 3.9: Overall effect of ligation. No significant difference among different ligation groups was found. N=54. Error bars indicate SEM.

More specifically, ANOVA was performed for detailed statistical analysis among the different groups, including side of ligation (ligated v.s. nonligated), ligation types (L4, L4+L5, and L5), and postoperative days (1, 4, 7, and 14). The results showed no significant difference among the types of ligation [$F(2, 140)=2.6557$, $p=0.073$] (Figure 3.9). The data were then collapsed under types of ligation. However, significant differences have been detected between the side of ligation [$F(1, 140)=37.232$, $p<0.001$] (Figure 3.10) and among the postoperative days [$F(3, 140)=10.258$, $p<0.001$] (Figure 3.8).

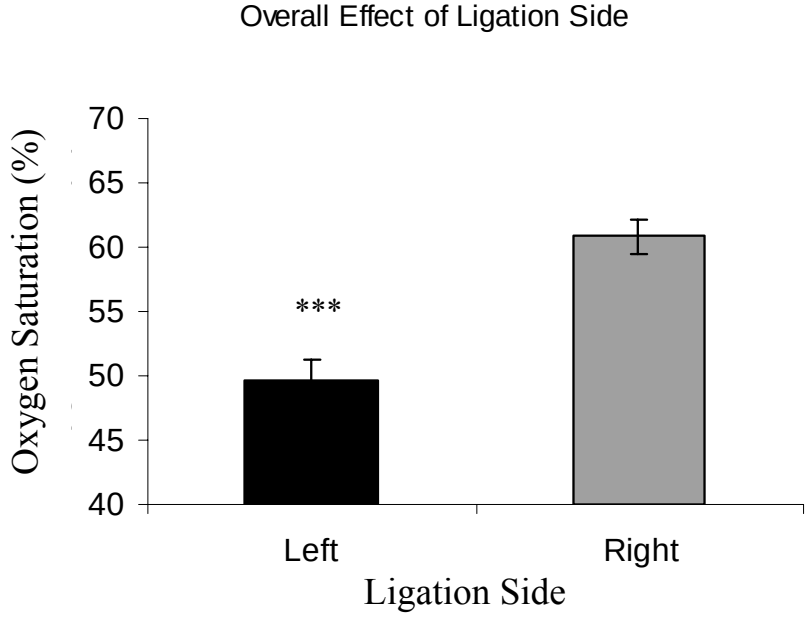

Figure 3.10: Overall effect of ligation side. Left (black bar) indicates ligated side and Right (gray bar) indicates control side. * indicates significant difference between the two sides. Error bars indicated SEM.

Significant interaction (Postoperative day x Side of ligation) was also observed [$F(3, 140)=4.3854$, $p<0.01$]. The average values of oxygen saturation on the ligated side (left) of the nerve were 62.1%±1.5%, 44.8%±1.5%, 49.2%±1.7%, and 42.3%±1.9% for

postoperative days 1, 4, 7, and 14 respectively. On the nonligated (right) side, for postoperative days 1, 4, 7, and 14, the values were 62.8%±1.7%, 64.1%±1.5%, 62.7%±1.5%, and 53.9%±2.0%, respectively. Posthoc Tukey-test revealed that significant differences were found between the ligated and control side (Figure 3.11) on days 4 ($p<0.001$), 7 ($p<0.01$), and 14 ($p<0.05$).

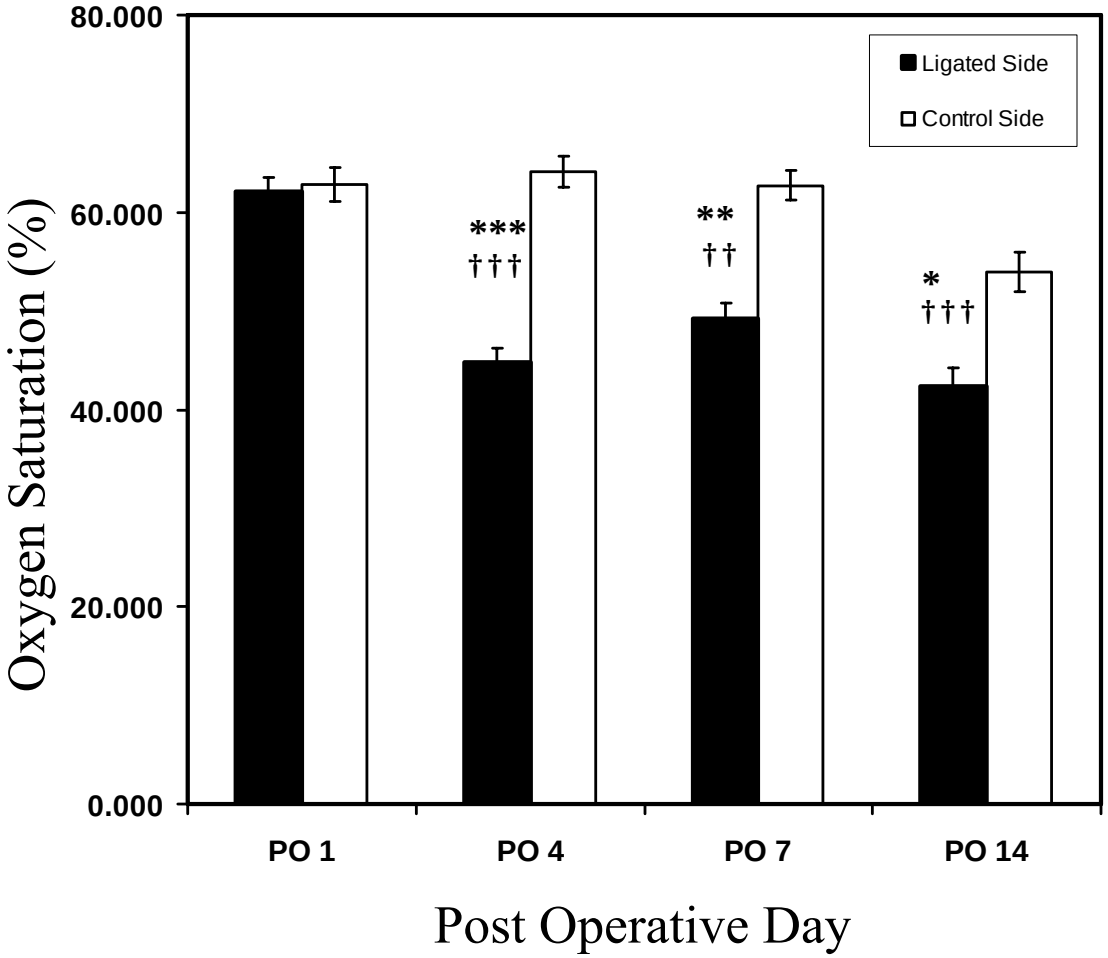

Figure 3.11: Overall effect of postoperative day and side. * indicates significant difference between left (L) and right (R); + indicates significant difference as compared with PO1 on the left side; no significant difference among right side

While no significant difference was found in the nonligated (right) side, Posthoc Tukey test also revealed significant differences on postoperative days 4 ($p<0.001$), 7 ($p<0.01$), and 14 ($p<0.001$) on the ligated (left) side, as compared to day one on the ligated (left) side (Figure 3.11).

3.4 Discussion

The goal of this study was to determine hemoglobin oxygen saturation on the ligated rat sciatic nerve, to reveal the differences between the ligated and control side, and thus to demonstrate the ability of optical spectroscopy to be an effective tool for discriminating diseased tissues from healthy tissues.

We have used the modified spinal nerve ligation model (Kim and Chung, 1982) to induce demyelination in the sciatic nerve. It is well known that nerve damage due to ligation will cause axonal degeneration in the nerve at the distal end to the site of ligation. This degeneration is a result of lack of supply in essential nutrients to the nerve from the cell body located proximal to the site of ligation.

It is known that gray matter has increased blood volume, and therefore, higher percentage of oxygen saturation than white matter, which is predominantly made of myelin fiber tracts and has lesser blood volume. In a prior study, it was shown that the oxygen saturation percentage was greater in gray matter of the brain when compared to white matter (Johns et al., 2001). Our study on the sciatic nerve, predominantly composed of myelin, showed a significantly higher percentage of oxygen saturation than what was reported in white matter of the brain structures. On the other hand, a previous study using microendoscopy and microlightguide spectrophotometry showed

an average of 81.2 % for baseline oxygen saturation and 68.1% during hypoxia on peripheral nerve oxygenation (Ibrahim et al., 1999). Our results on average started at 66% for day 1 after ligation and continuously dropped as the effect of ligation evolved till postoperative day 14.

Similar to our previous study, we were not able to find significant differences in hemoglobin oxygen saturation among the three ligation types. It would seem that the changes due to ligation of both L4 and L5 spinal nerve would be much greater than those due to ligation of either L4 or L5. One of the reasons could be the variations in the structure of the sciatic nerve itself. It was shown that the rat sciatic nerve is composed of spinal nerves L4-L6 (Gelderd and Chopin, 1977; Hebel and Stromberg, 1996). But, this theory was refuted when another research group pointed out that L4 and L5 were the main contributors to the sciatic nerve in all rats, but the contribution of L3 and L6 varied from rat to rat (Astao et al., 2000). Such inter-subject variability has also been previously reported (Sato et al., 2005). Another factor that could affect the signal we obtain is the movement of the rat paw. In our study we found that due to long duration of the experiment, there were certain instances of paw twitch. However, such twitching seems unlikely to account for a lack of group differences because there was no systematic difference in paw movement. One reasonable interpretation is that the optical probe detects a global average within the affected volume of the sciatic nerve, not being able to spatially resolve the local difference of nerve degeneration. On the other hand, it seems rational to hypothesize that the nerve degeneration induced by a single spinal nerve ligation can create demyelination or degeneration of the sciatic nerve as a group,

showing identical effects as those induced by multiple spinal nerve ligations. While the approval of this hypothesis needs further investigation, it supports and accounts for our previous observation in light scattering changes caused by similar ligation procedures (Senapati et al., 2005).

It is noteworthy that we have analyzed the optical reflectance spectra separately in both the visible range, through this paper, and the NIR range (Senapati et al., 2005; Radhakrishnan et al., 2005) for different characteristics of tissue. While the visible spectra focus on absorption of hemoglobin concentrations and thus allow for quantification of hemoglobin oxygen saturation within the nerve vasculature, the NIR spectra emphasize light scattering in nerve tissues due to cell membrane, organelle membrane, the nuclei, and other intracellular organelles (Senapati et al., 2005). Such analyses are based on the fact that blood or hemoglobin has a strong absorption peak in the visible range, but it is relatively transparent in the NIR range, where light scattering is dominant. The results obtained using both the visible and NIR spectroscopies are in good agreement and complementary with one another in identifying nerve degeneration, enabling the researchers to gain insight into physiological evolution during nerve degeneration.

CHAPTER 4

CHANGES IN LIGHT SCATTERING AND HEMOGLOBIN OXYGEN SATURATION IN RAT SPINAL CORD DURING PERIPHERAL ELECTRICAL STIMULATION

4.1 Introduction

In imaging the surface of the brain, use of intrinsic optical signals (IOS) to monitor neural activities *in vivo* is becoming more recognized (Miller et al., 1993; Uchino et al., 1993; Ikeda et al., 1996; Kristal and Dubinsky, 1997; Lemasters et al., 1997; Johnson et al., 2000) and popularly utilized in the field of neurosciences (Aitken et al., 1999; Andrews et al., 1999; Nomura et al., 2000; Haller et al., 2001;). But both IOS and intrinsic optical imaging (IOI) are highly affected by both light scattering and absorption of the measured neural tissue or the brain due to morphological structures and hemodynamic aspects of the brain, respectively. So far it is difficult to separate light scattering and absorption effects within the measured data of IOS and IOI. One common practice in neuroscience research using optical brain imaging is to define a practical index, such as an intensity index (Gias et al., 2005), to associate either IOS or IOI with the neural activity, without being able to decouple the effects from morphological (scattering) and hemodynamic (absorption) aspects of the brain.

On the other hand, in imaging deep tissues in the brain, extensive research has shown that neuronal stimulation results in two kind of optical signals: the fast signal due

to changes in light scattering and the slow hemodynamic signal. It is believed that the fast optical signal originates in the range of milliseconds after stimulation and is related to light scattering (Cohen, 1973; Wachowiak and Cohen, 2003). It was also shown that the changes in light scattering are simultaneous with electrical changes, cell swelling, and increased heat production, and thus the optical signal is directly related to neuronal activity (Tasaki, 1999). The detection of this signal has been shown in both human and animals (Morren et al., 2002; Wolf et al., 2002; Rector et al., 2005; Swartling et al., 2005). On the other hand, the slow hemodynamic signal usually occurs in the range of seconds after stimulation and can be measured by the non-invasive near infrared spectroscopic (NIRS) approach (Yodh and Boas, 2003). This is characterized by an increase in oxygenated hemoglobin [HbO] and a decrease in deoxygenated hemoglobin [HbR] as a result of increases in tissue consumption of oxygen and glucose, leading to an increased blood flow (Dunn et al., 2003). Such kind of hemodynamic signals have been reported before by various authors under different experimental paradigms (Villringer and Chance, 1997; Franceschini et al., 2000; Toronov et al., 2001; Bradley et al., 2003; Fuster et al., 2005). In the latter case, the quantifications of the [HbR] and [HbO] signals are obtained using a common assumption that light scattering does not vary much during the neural (slow) responses and activities. While this assumption has become popularly used in studying dynamic neural functions based on the NIRS measurements, it may be inaccurate and could lead to non-insignificant errors in analyzing the coupling between neural activity and hemodynamics. It would be scientifically useful to quantify how much the light scattering changes could occur during neuronal activities in comparison to the hemodynamic changes. Once the contributions from both changes in light scattering

and hemodynamics are determined, we will be able estimate the accuracy of the current quantitative means that is used for [HbO] and [HbR] calculations in functional NIRS (fNIR) brain imaging.

Specifically, in this study, we aim to detect changes in light scattering (S_{NIR}) and hemoglobin oxygen saturation ($S_{sc}O_2$) on the rat spinal cord due to peripheral electrical stimulation. The measurements were performed *in vivo* using a fiber optic needle probe with a source-detector separation of ~100 microns between the two 100-micron fibers. By using both NIR and visible spectroscopy (see Fig. 1), we will demonstrate that there would be significant changes in both S_{NIR} and $S_{sc}O_2$ on the rat spinal cord during its peripheral stimulation, providing awareness of the fact that variation in light scattering during brain activation exists and should be considered in fNIR brain imaging for better accuracy.

4.2 Materials and Methods

4.2.1 Subjects and surgical methods

Sprague-Dawley rats (n=8, 300 – 400 g, UTA vivarium) were used for this study. The experimental procedures were approved by the IUCAC of University of Texas at Arlington and followed the guidelines of the International Association for the study of pain (Zimmermann, 1993). Surgical procedures have been explained in detail in Section 2.2.1.1.

4.2.2 Experimental set up

The instruments and their set-up used for this experiment has been completely explained previously in Section 2.2.1.2.

4.2.3 Data acquisition

The optical reflectance in both visible and NIR regions was recorded from the fifth segment of the left lumbar (LL5). Electrical stimulations were given to the plantar paw of the left hind limb with a graded intensity from 20 V to 50 V stimulations, in an increment of 10 V, at a frequency of 10 Hz and pulse-width of 1 millisecond duration. The stimulations were given for 20 seconds. The intra-stimulus interval (ISI) was about 10 minutes. The optical measurements were recorded continuously starting from a baseline measurement for 3-5 minutes. Data was taken at 1 Hz sampling rate with an integration time of 60 ms using the LabView programming software (National Instruments, Austin, TX) as the interface between the computer and the spectrometer.

4.2.4 Data analysis for light scattering

One goal of this study was to show changes in light scattering in the rat spinal cord during peripheral stimulation. To achieve this, the reflectance data in the NIR region were first converted to the spectral slope values between 700 nm - 900 nm, as shown by the two straight lines in Fig. 1 within the NIR window. This slope algorithm was previously developed (Johns et al., 1998), with a recent support (Radhakrishnan et al., 2005) that the spectral slopes in the NIR region, S_{NIR}, of rat sciatic nerves indeed have the same trends as their light scattering parameters. Changes in S_{NIR} have been successfully utilized as an index of changes in light scattering for the *in vivo* brain tissues (Giller et al., 2000, 2003) and sciatic nerves (Senapati et al., 2005; Radhakrishnan et al., 2005). In this study, we still utilize the same algorithm, explained in Section 1.3, to detect changes in light scattering during stimulation by comparing the maximum values of S_{NIR} (slope-max)

during the stimulation with the baseline S_{NIR} values. The data are represented as Mean ± Standard Error of Mean. Statistical significances ($p < 0.05$) were determined by *ANOVA* followed by *Tukey HSD posthoc* analysis (Statistica) to show significant differences of slope values between baseline and stimulation.

4.2.5 Data analysis for hemoglobin oxygen saturation

The algorithm to determine hemoglobin oxygen saturation is explained in Section 1.3.

4.2.6 Calculation of relative changes

For comparison, we also summarized the relative changes in both S_{NIR} and $S_{sc}O_2$ during stimulation of the hind paw with respect to the baseline. The percent changes for both S_{NIR} and $S_{sc}O_2$ are defined as

$$S_{NIR}\ Ratio = \frac{S_{NIR}(stimulation)}{S_{NIR}(baseline)} \tag{2a}$$

$$S_{sc}O_2\ Ratio = \frac{S_{sc}O_2(stimulation)}{S_{sc}O_2(baseline)}. \tag{2b}$$

4.3 Experimental Results

4.3.1 Changes in light scattering

Eight rats were used for this experiment. Figure 4.1 shows two representative traces collected from the same animal during the baseline and stimulation measurement, respectively, and it demonstrates clearly that the spectral slope increases during the stimulation.

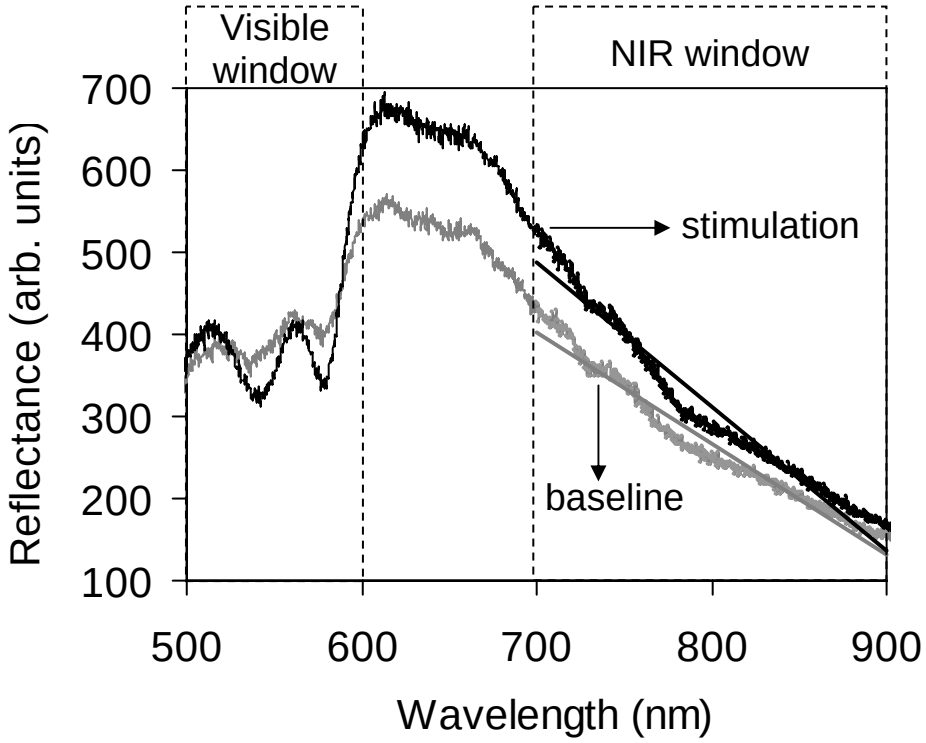

Figure 4.1: Visible-to-NIR reflectance spectra taken during a baseline and stimulation recording. The two spectra exhibit a difference in the NIR spectral slope between 700 and 900 nm, as shown by the two straight lines. This variation is used as an index for scattering variation due to peripheral stimulation. In the visible region (500-600 nm), there also exists a variation in spectral shape due to changes in hemoglobin oxygen saturation induced by the stimulation (black curve) in comparison to the baseline (gray curve). The stimulation curve is a representative with a stimulation voltage of 40 V.

Figure 4.2 shows a temporal plot of the changes in S_{NIR} over time of the data acquisition from a representative rat. The slope values are obtained from 700 to 900 nm, and the periods and intensities of stimulation are marked by the gray bars. This figure clearly confirms increases in the slope values during the stimulation periods with different stimulation magnitudes. Note that the temporal profile at 50V stimulation is

lower than the original baseline due to a possible physiological drift during the experiment.

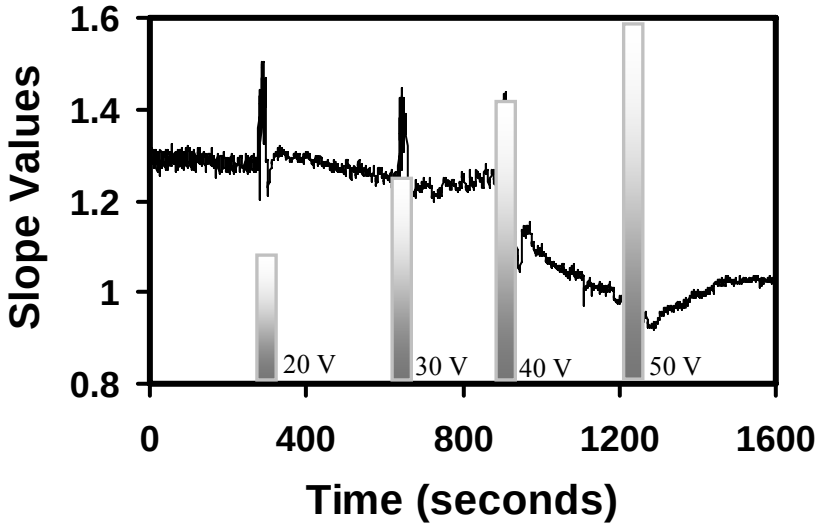

Figure 4.2: Changes in slope values during electrical stimulation obtained from one animal. The periods of stimulation are marked in gray bars at different height, representing stimulus intensities.

Table 4.1: Comparison of slope values between baseline and stimulation

No.	Ave Baseline	20V Max	Ave Baseline	30V Max	Ave Baseline	40V Max	Ave Baseline	50V Max
1	0.864	0.949	0.888	0.930	0.935	1.044	0.926	1.053
2	0.821	1.039	0.969	1.143	0.976	1.126	0.977	1.134
3	1.287	1.503	1.276	1.447	1.236	1.439	1.051	1.211
4	1.073	1.310	1.217	1.367	1.307	1.341	1.327	1.393
5	1.038	1.031	0.974	1.015	0.948	0.994	0.933	1.071
6	1.540	1.649	1.510	1.673	1.485	1.733	1.513	1.683
7	2.980	3.111	2.894	3.174	2.871	2.951	2.971	3.043
8	1.987	2.023	1.401	1.598	1.321	1.459	1.274	1.451
Mean	**1.449**	**1.577**	**1.391**	**1.543**	**1.385**	**1.511**	**1.371**	**1.505**
SEM	**0.258**	**0.254**	**0.228**	**0.251**	**0.224**	**0.223**	**0.241**	**0.233**

ANOVA was performed for detailed statistical analysis of the S_{NIR} value among the different groups, including stimulus conditions (baseline vs. stimulation), and stimulation intensities (20 – 50 V). The results showed no significant difference in S_{NIR} values induced by different stimulus intensities [$F(3, 21)=0.553$, $p=0.65$] (Figure 4.3). There were significant differences between average S_{NIR} values of baseline and average maximum S_{NIR} values during the stimulations [$F(1, 7)=70.83$, $p<0.001$] (n=8). The S_{NIR} values of the baseline for 20, 30, 40, and 50V stimulations were 1.45±0.26, 1.39±0.23, 1.38±0.22, and 1.37±0.24, respectively. The average max-slope values for the corresponding stimulations were 1.58±0.24, 1.54±0.25, 1.51±0.22, and 1.5±0.23, respectively.

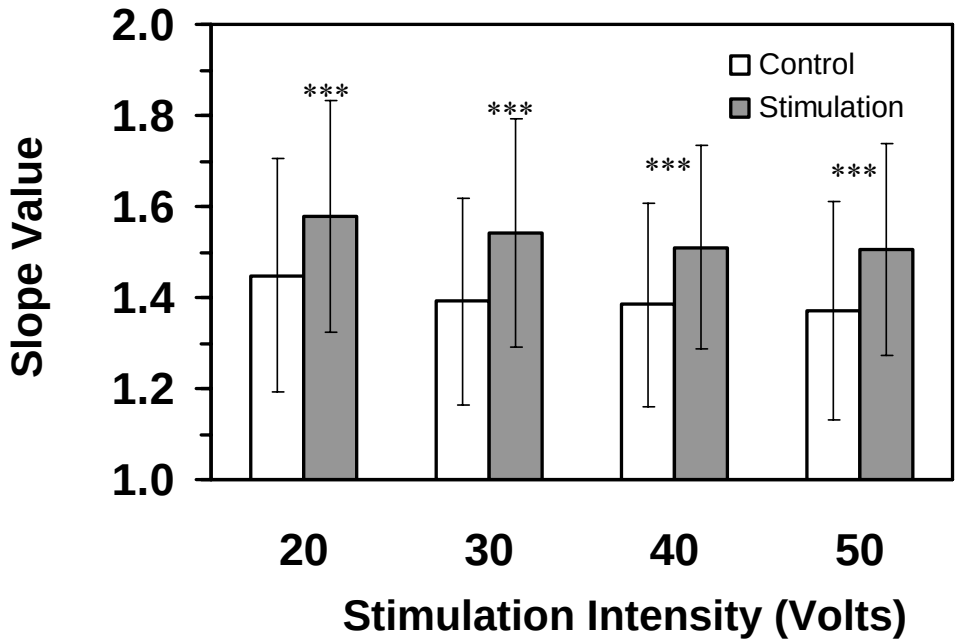

Figure 4.3: Comparison of slope values between baseline and stimulation. The slope values for the stimulation indicate max-slopes by gray bars. The error bars indicate standard error of mean. Significant difference was found between baseline and stimulation slope values. * indicates significant difference between baseline and stimulation. Note: * ($p<0.05$), ** ($p<0.01$), and *** ($p<0.001$).

Comparing with the baseline, posthoc Tukey HSD analysis indicated that the S_{NIR} values were significantly higher for max-slopes induced by 20 V ($p < 0.001$), 30 V ($p < 0.001$), 40 V ($p < 0.001$), and 50 V ($p < 0.001$) with respect to the baselines, as shown in Figure 3A. The net change, shown in Table 4.2, of S_{NIR} values for 20, 30, 40, and 50 V were 0.13±0.03, 0.15±0.03, 0.13±0.03, and 0.13±0.02, respectively (Figure 4.4).

Table 4.2 Net change in slope values

No.	20V Max	30V Max	40V Max	50V Max
1	0.085	0.042	0.109	0.127
2	0.218	0.174	0.150	0.157
3	0.216	0.171	0.203	0.160
4	0.237	0.150	0.034	0.066
5	-0.007	0.041	0.046	0.138
6	0.109	0.164	0.247	0.170
7	0.131	0.280	0.080	0.072
8	0.036	0.197	0.137	0.177
Mean	**0.128**	**0.152**	**0.126**	**0.133**
SEM	**0.032**	**0.028**	**0.026**	**0.015**

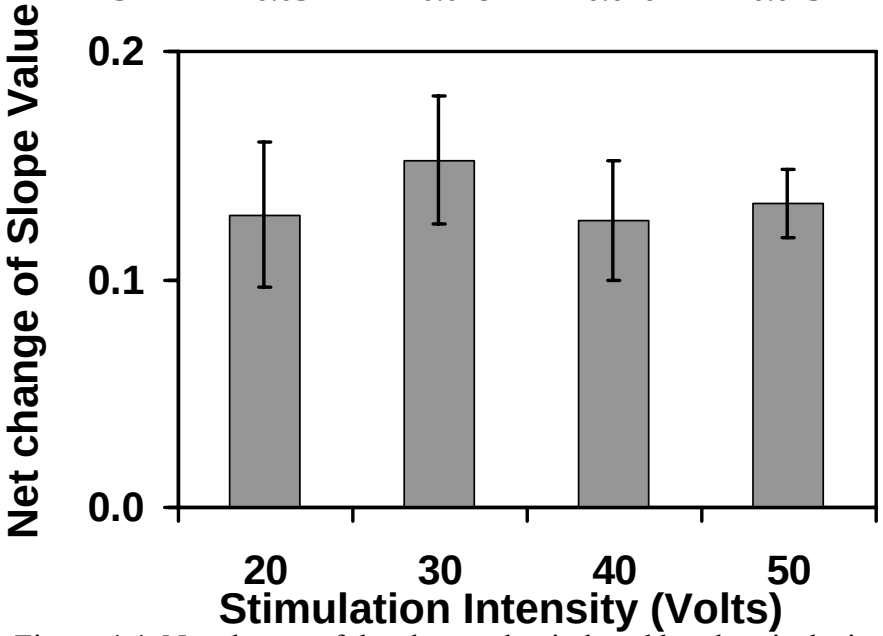

Figure 4.4: Net change of the slope value induced by electrical stimulation. The slope values for the stimulation indicate max-slopes by gray bars. The error bars indicate standard error of mean.

ANOVA was also performed for detailed statistical analysis of the S_{NIR} changes as a ratio to the baseline readings among the different groups, using eq. (2a). The results showed no significant difference in S_{NIR} values among the stimulus intensities [$F(3, 21)=0.09$, $p=0.96$] (Figure 4.5). There was a significant increase in the average ratio of the maximum S_{NIR} during the stimulations [$F(1, 7)=43.83$, $p<0.001$]. Taking the baseline as 100%, the average ratios for 20, 30, 40, and 50V were 111.0±3.5 %, 110.9±1.7 %, 110.1±2.1 %, and 111.5±1.8 %, respectively (Table 4.3). Posthoc Tukey HSD analysis indicated that the S_{NIR} ratio was significantly higher for max-slopes induced by 20 V ($p < 0.001$), 30 V ($p < 0.001$), 40 V ($p < 0.01$), and 50V ($p < 0.001$), with respect to the S_{NIR} baseline readings, as shown in Figure 4.5.

Table 4.3: Ratio of max-slope values to baseline

No.	20V Max	30V Max	40V Max	50V Max
1	109.838	104.730	111.658	113.715
2	126.553	117.957	115.369	116.070
3	116.783	113.401	116.424	115.224
4	122.088	112.325	102.601	104.974
5	99.326	104.209	104.852	114.791
6	107.096	110.848	116.658	111.206
7	104.386	109.661	102.794	102.428
8	101.821	114.068	110.406	113.914
Mean	**110.99**	**110.90**	**110.10**	**111.54**
SEM	**3.48**	**1.65**	**2.11**	**1.80**

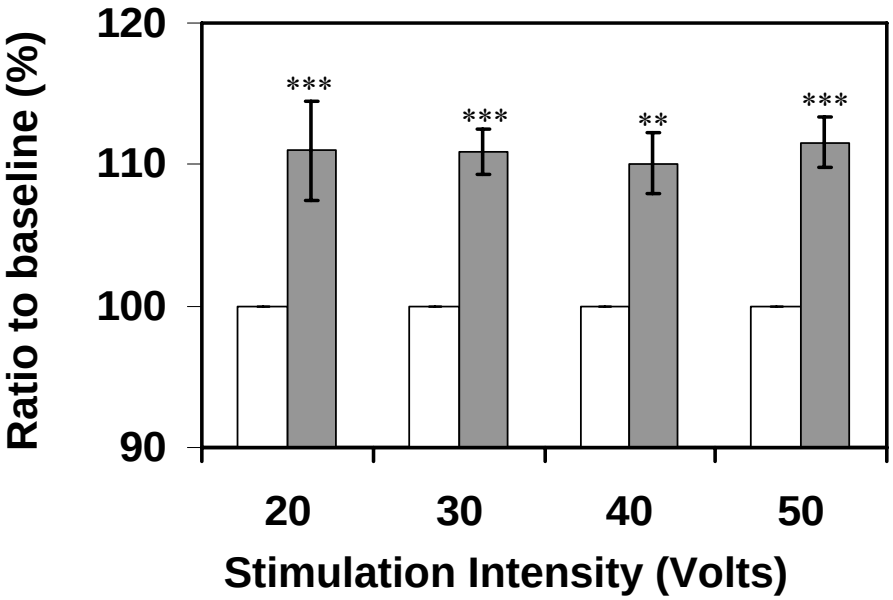

Figure 4.5: Ratio of the slope value induced by electrical stimulation to the baseline level. The slope values for the stimulation indicate max-slopes by gray bars. The error bars indicate standard error of mean. Significant difference was found between baseline and stimulation slope values. * indicates significant difference between baseline and stimulation. Note: * ($p<0.05$), ** ($p<0.01$), and *** ($p<0.001$).

4.3.2 Changes in hemoglobin oxygen saturation

By using the algorithm described in Section 1.3 with the calibrated spectra, we have obtained (Table 4.4) the $S_{sc}O_2$ values of the baseline averages for 20, 30, 40, and 50 V stimulations as 42.0±6.1 %, 40.1±3.3 %, 39.4±3.4 %, and 39.4±3.7 % respectively. The $S_{sc}O_2$ values during 20, 30, 40, and 50 V stimulations were 48.6±5.4 %, 44.8±3.8 %, 44.4±3.7 %, and 44.8±4.0 % respectively, as plotted in Figure 4.6.

Table 4.4: Comparison of $S_{sc}O_2$ values between baseline and stimulation

No.	Ave Baseline	20V Max	Ave Baseline	30V Max	Ave Baseline	40V Max	Ave Baseline	50V Max
1	51.249	53.134	51.549	51.498	51.695	53.222	52.373	52.546
2	16.284	28.323	28.948	32.422	30.523	34.336	31.045	34.494
3	26.504	31.341	27.065	29.144	24.264	27.574	18.985	23.331
4	33.788	41.168	35.338	41.338	31.566	39.845	35.346	42.628
5	46.700	52.082	47.999	51.554	47.320	52.277	46.450	51.871
6	47.974	62.011	48.725	62.102	47.487	58.170	45.520	58.665
7	40.494	46.712	37.787	45.622	40.395	47.622	43.532	49.349
8	72.764	74.085	43.433	44.571	41.517	42.348	41.683	45.184
Mean	41.97	48.61	40.11	44.78	39.35	44.42	39.37	44.76
SEM	6.07	5.39	3.28	3.78	3.42	3.66	3.73	4.00

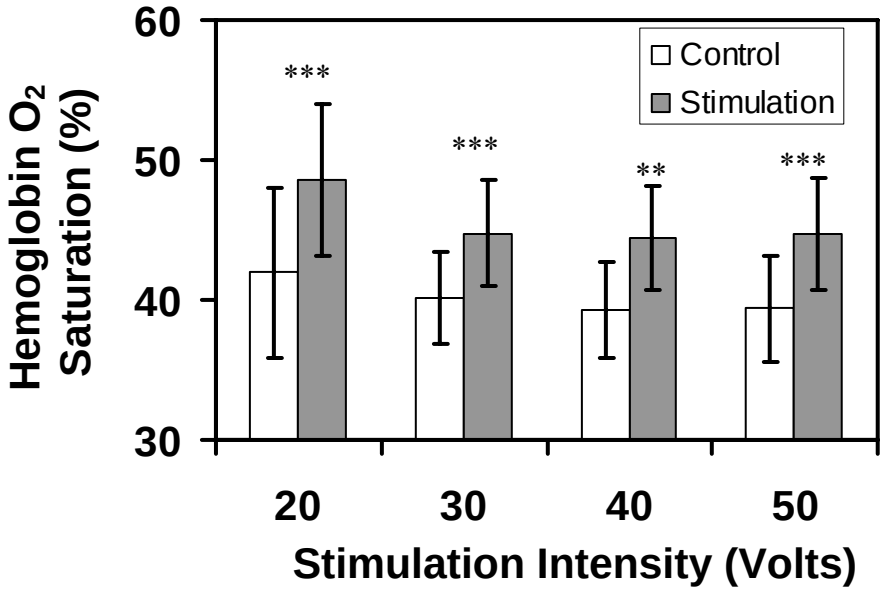

Figure 4.6: Comparison of raw $S_{sc}O_2$ values between baseline and stimulation. The $S_{sc}O_2$ values during the stimulation correspond to maximal $S_{sc}O_2$. The error bars indicate standard error of mean. Significant difference was found between baseline and stimulation $S_{sc}O_2$ values. * indicates significant difference between baseline and stimulation. Note: ** ($p<0.01$), and *** ($p<0.001$).

Similarly, we performed ANOVA and found that there was a significant difference in the hemoglobin oxygen saturation among different groups, including stimulus conditions (baseline v.s. stimulation) and stimulation intensities (20 – 50 V). The results showed no significant difference in $S_{sc}O_2$ values among the stimulus intensities [$F(3, 21)=0.56$, $p=0.65$] (Figure 4.6). There were significant differences between average $S_{sc}O_2$ values of baseline and average value during the stimulations [$F(1, 7)=16.99$, $p<0.01$] (n=8). Comparing with the baseline, posthoc Tukey HSD analysis indicated that the $S_{sc}O_2$ values were significantly higher for stimulations induced by 20 V ($p < 0.001$), 30 V ($p < 0.001$), 40 V ($p < 0.001$), and 50V ($p < 0.001$), as shown in Figure 4.6. The net change of $S_{sc}O_2$ values for the corresponding stimulations were 6.6±1.6 %, 4.7±1.5 %, 5.1±1.2 %, and 5.4±1.3 %, respectively (Figure 4.7).

Table 4.5: Net change in $S_{sc}O_2$ values

No.	20V Max	30V Max	40V Max	50V Max
1	1.886	-0.051	1.527	0.173
2	12.039	3.474	3.814	3.449
3	4.837	2.078	3.310	4.345
4	7.380	6.000	8.279	7.282
5	5.382	3.554	4.957	5.421
6	14.037	13.376	10.683	13.144
7	6.218	7.836	7.227	5.817
8	1.320	1.138	0.831	3.501
Mean	**6.64**	**4.68**	**5.08**	**5.39**
SEM	**1.58**	**1.53**	**1.21**	**1.33**

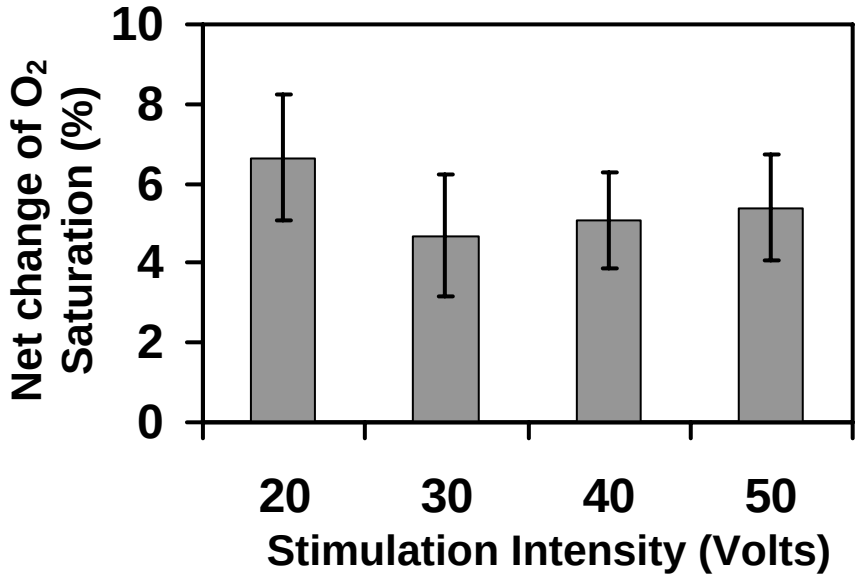

Figure 4.7: Summary of net change of $S_{sc}O_2$ values. The $S_{sc}O_2$ values for the stimulation are indicated by gray bars. The error bars indicate standard error of mean.

ANOVA was also performed for detailed statistical analysis of the $S_{sc}O_2$ changes as a ratio to the baseline among the different groups, using eq. (2b). The results showed no significant difference among the stimulus intensities [$F(3, 21)=1.24$, $p=0.32$] (Figure 4.8). There were significant increases in the average ratio of the $S_{sc}O_2$ changes during the stimulations [$F(1, 7)=20.16$, $p<0.01$]. Taking the baseline as 100%, the average ratio of $S_{sc}O_2$ changes to the baseline induced by 20, 30, 40, and 50V stimulations were 122.0±8.1 %, 111.9±3.3 %, 113.5±3.0 %, and 114.7±3.2 %, respectively (Table 4.6). Posthoc Tukey HSD analysis indicated that the $S_{sc}O_2$ ratios to the baselines were significantly higher for stimulations caused by 20 V ($p < 0.001$), 30 V ($p < 0.01$), 40 V ($p < 0.01$), and 50V ($p < 0.01$), as shown in Figure 4.8.

Table 4.6: Ratio of $S_{sc}O_2$ changes to the baseline

No.	20V Max	30V Max	40V Max	50V Max
1	103.679	99.900	102.953	100.331
2	173.932	112.002	112.495	111.108
3	118.252	107.679	113.640	122.888
4	121.841	116.980	126.227	120.602
5	111.525	107.405	110.476	111.670
6	129.260	127.453	122.497	128.876
7	115.355	120.736	117.891	113.363
8	101.815	102.620	102.002	108.399
Mean	**121.96**	**111.85**	**113.52**	**114.65**
SEM	**8.09**	**3.31**	**3.03**	**3.20**

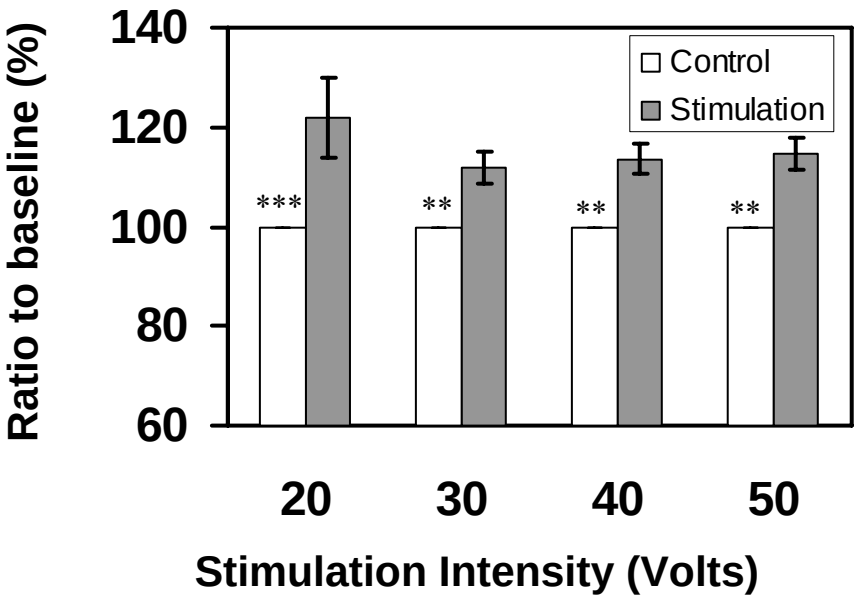

Figure 4.8: Summary of raw ratio to baseline $S_{sc}O_2$ values. The error bars indicate standard error of mean. Significant difference was found between baseline and stimulation $S_{sc}O_2$ values. * indicates significant difference between baseline and stimulation. Note: ** ($p<0.01$), and *** ($p<0.001$).

All of these changes were monitored on the ipsilateral side. Furthermore, Figure 4.9 summarizes the percentage changes in $S_{sc}O_2$ (open bars) and S_{NIR} (gray bars) between the baseline and stimulation. A close inspection of this figure reveals that the mean relative changes over 4 different stimulation voltages for $S_{sc}O_2$ were 22.0±8.1 %, 11.9±3.3 %, 13.5±3.0 %, and 14.7±3.2 %, respectively (overall mean: 15.5% ± 4.4%); and for S_{NIR} were 11.0±3.5 %, 10.9±1.7 %, 10.1±2.1 %, and 11.5±1.8 %, respectively (overall mean: 10.9% ± 0.6%).

Table 4.7: Relative percentage changes of max-slope and $S_{sc}O_2$ values compared to its baseline

No.	**20V Max**		**30V Max**		**40V Max**		**50V Max**	
	Slope	$S_{sc}O_2$	**Slope**	$S_{sc}O_2$	**Slope**	$S_{sc}O_2$	**Slope**	$S_{sc}O_2$
1	9.838	3.679	4.730	-0.100	11.658	2.953	13.715	0.331
2	26.553	73.932	17.957	12.002	15.369	12.495	16.070	11.108
3	16.783	18.252	13.401	7.679	16.424	13.640	15.224	22.888
4	22.088	21.841	12.325	16.980	2.601	26.227	4.974	20.602
5	-0.674	11.525	4.209	7.405	4.852	10.476	14.791	11.670
6	7.096	29.260	10.848	27.453	16.658	22.497	11.206	28.876
7	4.386	15.355	9.661	20.736	2.794	17.891	2.428	13.363
8	1.821	1.815	14.068	2.620	10.406	2.002	13.914	8.399
Mean	10.986	21.957	10.900	11.847	10.095	13.523	11.540	14.655
SEM	3.482	8.085	1.650	3.311	2.115	3.035	1.799	3.198

It suggests that comparable variations in both light scattering and hemodynamics occur along the spinal cord when a neuronal activity or stimulation is given. It also offers evidence that relative changes in both light scattering and hemoglobin oxygen saturation of the rat spinal cord can be clearly detected using a small source-detector separation probe when the peripheral electrical stimulation is induced.

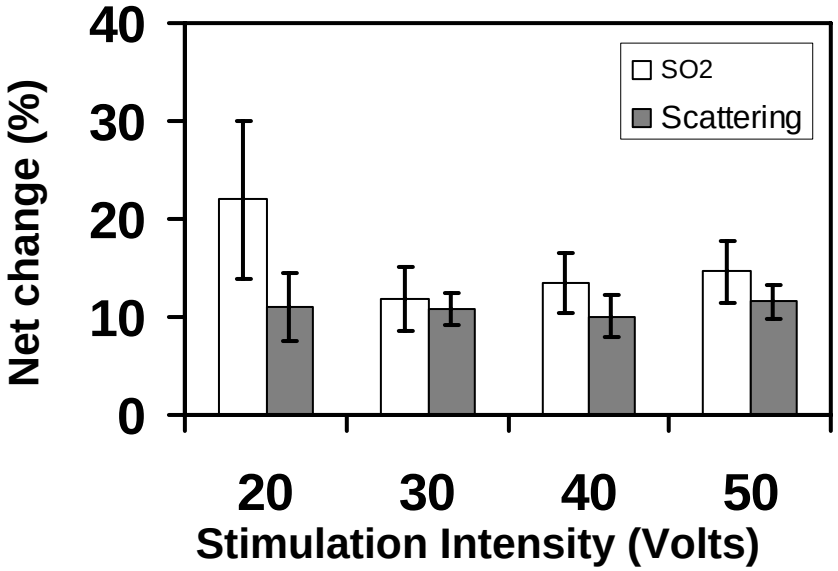

Figure 4.9: Comparison of the percentage changes in $S_{sc}O_2$ and S_{NIR} during stimulation.

4.4 Discussion

The goal of our study was to detect changes in both light scattering and hemoglobin oxygen saturation in the rat spinal cord ($S_{sc}O_2$) during peripheral electrical stimulation. To achieve this, we have analyzed the optical reflectance spectra in the visible to NIR range and determined changes in both spectral slopes, S_{NIR}, and $S_{sc}O_2$. The slope changes were used as indices to reflect changes in light scattering, and such analysis is based on the fact that in the NIR range light scattering is predominant over light absorption, and a small source-detector fiber probe with a few hundred microns would be much sensitive to light scattering than light absorption (Johns et al., 2005). The observed changes in light scattering given in this study are in good agreement with other reports that show changes in light scattering (Malonek and Grinvald, 1997; Rector et al., 1997).

In our study, on the other hand, we utilized the visible spectroscopy to quantify hemoglobin oxygen saturation since both oxy- and deoxy- hemoglobin absorption bands between 500 -600 nm have large and distinct features, allowing us to fit an empirically calibrated equation to obtain $S_{sc}O_2$ values for the rat spinal cord with the same small source-detector fiber probe. In this way, we took the advantage of broad spectroscopic features from visible to NIR region and determined both hemodynamic parameters and light scattering during rat peripheral electrical stimulations, respectively (Figure 4.1).

In fNIR brain imaging, the currently common and accepted methods to quantify hemodynamic parameters, such as [Hb] and [HbO], are based on modified Beer-Lambert's law, which depends on the measurements of overall variations in light intensities reflected from the human head (Yodh and Boas, 2003). Since modified Beer-Lambert's law is highly light-absorption dominant, the light scattering effect is suppressed as a constant within the differential pathlength factor (DPF) in most of approaches where fNIR brain studies have been conducted (Villringer and Chance, 1997). One reason that modified Beer-Lambert's approach has been popularly utilized in fNIR brain imaging stems from the technical challenge: it is theoretically impossible to separate light scattering and absorption using continuous-wave (CW) light with single source-detector separation and only several discrete wavelengths. While it is theoretically possible to quantify both light scattering and absorption with the time-domain (TD) or frequency-domain (FD) approach (Yodh and Boas, 2003), a multi-channel, TD or FD fNIR brain imager posts a real financial challenge in practice, almost infeasible for most of researchers to obtain such an expensive system for their studies. Thus, the CW NIR imaging means becomes more practical and available to the

neuroscience researchers for studying/mapping the brain functions, and modified Beer-Lambert's law is a reasonable approximation to work well with the CW NIR approach. It is still important scientifically, however, to know if indeed there is a variation in light scattering during the brain activation, besides hemodynamic changes. If there is a variation in light scattering, knowing its ratio to the variation in hemodynamic changes will help us estimate and validate the accuracy of the current fNIR brain imaging methods. Our study is an attempt to address this issue, i.e., to quantify light scattering and hemodynamics during the brain stimulation, by using an invasive, non-conventional, visible-to-NIR spectroscopic method with a needle-like, fiber-optic probe. In this way, we are able to obtain quantitative variations in both light scattering and hemodynamic parameter from the rat spinal cord during peripheral electrical stimulations.

Although our measurements were taken on the rat spinal cord, the dynamic results in both light scattering and hemodynamics can be readily applicable to the rat somatosensory cortex. In principle, neuronal stimulation signals can be recorded electrophysiologically at various locations, e.g., at peripheral, spinal, and cortical locations. We expect that the optical signals can be in the same way recorded at those respective locations, revealing similar signal changes in light scattering and hemodynamics taken either at the spinal cord or at the cortical location.

There might exist a question on the optically interrogated volume by the optical probe used in our study. We have defined a term called the 'Look Ahead Distance' (LAD) that is the measure of the depth up to which light could penetrate through using our needle probe. We have previously demonstrated that LAD is a function of light scattering. For the probe used in this study, it was estimated around 1.2 to 1.5 mm for a

wide range of values of reduced scattering coefficient (μ_s') (Giller et al., 2003; Gurnani, 2003; Qian et al., 2003). Taking into account the dimensions of the lumbar segment of the spinal cord and the thickness of white matter, it is possible that the light could penetrate up to the gray matter depths. This would vary greatly depending on anatomical differences between animals, and this issue is beyond the scope of this current study.

It is known that Aδ and C fibers carry the noxious stimulus and terminate at laminae I and II of the spinal cord. Lamina II (the substantia gelatinosa) is associated with the modulation of nociceptive input (Price et al., 1979). The range of stimulus (20 to 50V) used in our study is up to the noxious range, and neuronal activity is expected in the ipsilateral dorsal horn in laminae I and II. These neuronal signals will travel rostrally to the brain stem, thalamus, and eventually project to the somatosensory cortex. Electrophysiologically, these signals can be recorded at various levels (i.e., at peripheral, spinal, supraspinal, and cortical locations). From the numerous studies on the nervous system of the rat, it is established that the hind paws are innervated by fibers from the third to sixth lumbar spinal cord segments. Takahashi et al. (2003) shows that the L4 and L5 spinal cord segments innervate the main dermatomes of the rat hind paw. Based on these observations, our results are well correlated. Functional MRI studies involving animals have shown activity in the 3rd lumbar (L) to 1st sacral (S) spinal cord segments following electrical stimulation hind paw (Malisza et al. 2003) with the greatest activity in the L4-L5 regions of the spinal cord (Lawrence et al., 2004).

We recorded an average increase of 15.9% in $S_{sc}O_2$ during 20, 30, 40, and 50V stimulations, which is similar to the changes in BOLD signal in fMRI studies, as reported by others (Malisza and Stroman, 2002; Lawrence et al., 2004). Fast light scattering

changes within milliseconds were also reported by others (Cohen, 1973; Wolf et al., 2002), but we did not investigate the fast optical signals. This is partially due to our current instrument limitation; namely, our data acquisition rates are not fast enough to collect fast light scattering changes in the order of millisecond.

In our study, there exist experimental variations possibly caused by 1) subject-to-subject variability in spinal cord anatomy, 2) position of dorsal roots when they enter the spinal cord, and 3) slight body movement due to respiration. Issue regarding inter-subject variability has been previously reported (Sato et al., 2005). The current method also lacks in spatial resolution. One way to improve this is to use a CCD camera so as to image the variations in light intensity across a large area from selected wavelengths.

CHAPTER 5

CONCLUSION AND POSSIBILITIES FOR FUTURE WORK

5.1 Conclusions

The overall objective of this thesis is to determine optical properties in specific regions of the rat CNS using a small source-detector separation fiber optic needle probe. The conclusions are provided in the same order of the hypothesis and aims in Section 1.5.

Hypothesis 1: Optical properties of the spinal cord can be determined using a small source-detector separation fiber optic needle probe

Aim 1: to obtain spatial maps of the rat spinal cord showing regions of varying optical properties

Conclusion: spectral slope maps and the μ_s' maps of the rat spinal cord have been generated with higher μ_s' values in the lumbar regions (34.2±2.1 cm^{-1}) and lower values at the center of cord (19.9±1.0 cm^{-1}) near the blood vessels. This is further proof that NIRS can be used to identify variations in anatomical sub-structures with different optical properties.

Hypothesis 2: There would be a decrease in the values of light scattering and hemoglobin oxygen saturation in the rat sciatic nerve due to demyelination / degeneration.

Aim 2: to determine light scattering (Chapter 2) and hemoglobin oxygen saturation values (Chapter 3) of the rat sciatic nerve due to demyelination / degeneration induced by spinal nerve ligation

Conclusion: we utilized a modified spinal nerve ligation method to induce nerve degeneration, and three types of ligation on left spinal nerve (L4, L4 and L5, L5) were performed in rats. The optical reflectance measurements in the visible range were taken from the left and right sciatic nerves on postoperative days 1, 4, 7, and 14. We did not observe significant difference among the three types of ligation, nor between left and right sciatic nerve at postoperative day 1. Significant decreases in light scattering and oxygen saturation were shown between the ligated and control sciatic nerves at postoperative days 4, 7, and 14. This study continues to demonstrate the effectiveness of optical methods in determining/ quantifying tissue properties and physiological parameters, showing the potential of optical spectroscopy for clinical applications in detecting demyelination and degeneration of the nervous system.

Hypothesis 3: There would be an increase in the values of light scattering and hemoglobin oxygen saturation in the rat spinal cord during peripheral electrical stimulation.

Aim 3: to determine light scattering and hemoglobin oxygen saturation values of the rat spinal cord during peripheral electrical stimulation.

Conclusions: using simple and robust visible-NIR spectroscopic instrumentation, we have shown comparable changes in light scattering, using

spectral slope as an index and in hemoglobin oxygen saturation on the rat spinal cord during peripheral electrical stimulation. The light scattering changes are about 10.9% from baseline to the maximum value of slope during stimulation, while the hemoglobin oxygen saturation increased by 15.5% due to the peripheral stimulation. From this study, we wish to demonstrate that the ignorance of variation in light scattering during brain activation may lead to a large overestimate for the hemodynamic parameters in functional NIR brain imaging.

Hypothesis 4: Peripheral electrical stimulation would induce an increase in blood flow

Aim 4: to determine values of hemoglobin derivatives on rat spinal cord during peripheral electrical stimulation

Conclusions: using modified Beer-Lambert's law, we were unable to convincingly prove changes in hemoglobin derivative concentrations and oxygen saturation changes as a function of those derivatives. The insensitivity of the probe to changes in absorption in the NIR region could be the primary reason behind these results.

5.2 Suggestions for Future Work

Based on all the results obtained in this thesis, there is room for tremendous improvement. Some of the possible studies are

1. The reported results in this paper prove the usefulness of the technique, which may have a potential clinical application for minimally invasive, real-time, intraoperative monitoring of subjects suffering from demyelinating CNS diseases.

2. NIRS has potential applications in intraoperatively identifying degenerated nerves before nerve grafting, helping locate the degenerated segment along the nerve and decide the length of nerve graft required, and 2) characterization of light scattering under external neuronal or neurological stimulations *in vivo* to gain insight into functional brain physiology

3. Further exploration in instrumentation and algorithms to accurately quantify light scattering changes on the brain cortex during brain activation is needed to warrant and validate the accuracy of functional NIR brain studies.

4. The use of fiber optic needle probes and the discussed instrumentations lacks temporal and spatial resolution. One way to tackle this would be to use high speed CCD cameras. Building up a system to have milli- to micro-second acquisition speed and a large enough spatial resolution and the need to develop algorithms to quantify tissue optical properties is an interesting task in hand.

APPENDIX A

DETERMINATION OF RELATIVE CHANGES ON RAT SPINAL CORD DURING PERIPHERAL ELECTRICAL STIMULATION

A.1 Introduction

It is well known that when light is incident on a tissue, it propagates into the sample and undergoes multiple scattering and absorption. Chapters 2 and 4 have well elucidated the effects of scattering changes under certain interventions. This chapter focuses on causes and effects of light being absorbed within the tissue.

In the near-infrared region, the absorption mean free path ($1/\mu_a$) is much longer than the scattering mean free path. Thus, the scattering coefficient of the tissue, μ_s, is always larger than the absorption coefficient of the tissue, μ_a. Light absorption of tissue depends strongly on the wavelength, while light scattering of tissue decreases smoothly and gradually with increasing wavelength. The basic principle of NIRS is that oxygenated and deoxygenated hemoglobin molecules are the major chromophores in tissue in the near-infrared region (~700 to 900 nm), and they exhibit distinct absorption characteristics as shown in Figure A.1. There are other chromophores like cytochrome and melanin whose effects are negligible in the NIR wavelength range (Figure A.2).

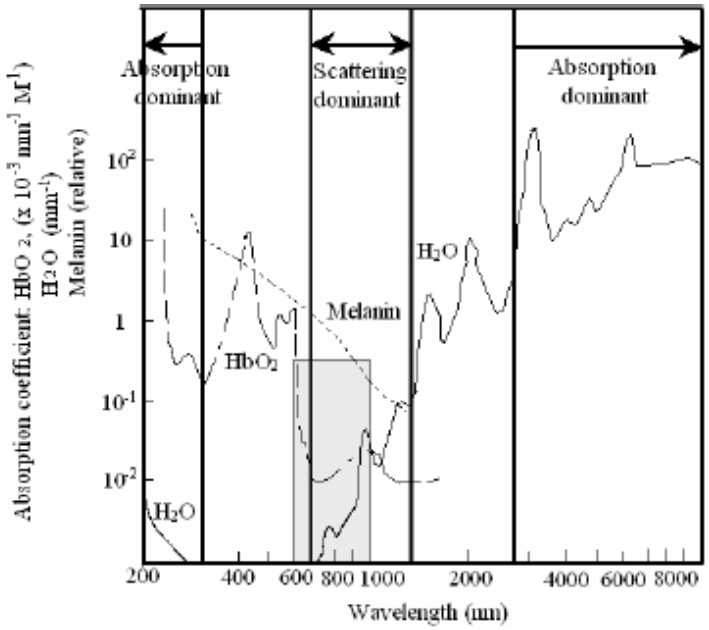

Figure A.1: Spectrum of tissue absorbing chromophores (Wilson et al., 1988)

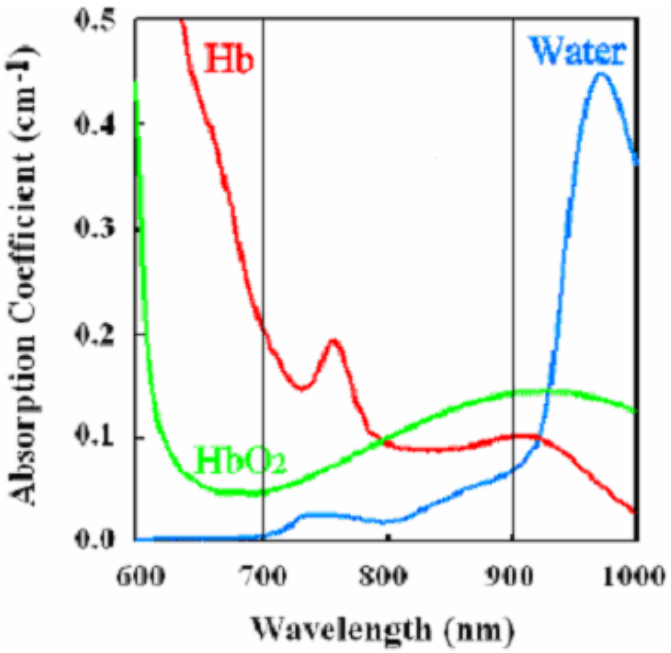

Figure A.2: Absorption spectrum in NIR window (Paunescu, 2001)

NIRS has been extensively used over the last decade in a large number of applications. In NIRS, light in the near infrared wavelength range is incident on the tissue sample under investigation and the transmitted or reflected light from the tissue is recorded for the quantification of hemoglobin concentrations. In principle, for large homogeneous samples, concentrations of oxygenated hemoglobin [HbO], deoxygenated hemoglobin [HbR], and oxygen saturation (SaO_2) can be determined by measuring light absorption and scattering in tissue based on the diffusion theory (Patterson et al., 1986; Sevick et al., 1991).

The mathematical derivation for determining relative changes in hemoglobin derivative concentrations has been well explained (Kim et al., 2005) and used extensively for determining tumor oxygenation (Liu et al., 2000; Kim et al; 2003; Gu et al., 2003; Kim, 2005). The algorithm is as follows: from the Beer-Lambert's law, light absorption can be given as a function of hemoglobin concentration (Horecker, 1943; van Kampen and Zijlstra, 1965; Benesch et al., 1965; 1973; van Assendelft and Zijlstra, 1975) as

$$OD = \log\left(\frac{I_0}{I}\right) = \varepsilon c L \qquad \text{(A.1)}$$

where OD is the optical density, I_0 is the light intensity of the incident light, I is the intensity of the transmitted light, ε is the extinction coefficient of hemoglobin, c is the concentration of hemoglobin, and L is the length of light path through the sample. When the sample is a mixture of oxy- and deoxy-hemoglobin, eq. A.1 can be expanded (Benesch et al., 1965; 1973; van Assendelft and Zijlstra, 1975) as

$$OD^{\lambda} = \left(\varepsilon_{HbR}^{\lambda}\left[HbR\right] + \varepsilon_{HbO}^{\lambda}\left[HbO\right]\right)L \qquad \text{(A.2)}$$

where OD^{λ} is the optical density or absorbance at wavelength λ and $\varepsilon_{HbR}{}^{\lambda}$ and $\varepsilon_{HbO}{}^{\lambda}$ are the extinction coefficients at wavelength λ for molar concentration of oxygenated hemoglobin [HbO] and deoxygenated hemoglobin [HbR] respectively. [HbO] and [HbR] can be determined by measuring light absorbance at two specific wavelengths with known extinction coefficients as

$$\left[HbO\right] = \left(\frac{\varepsilon_{HbR}^{\lambda_2} \times OD^{\lambda_1} - \varepsilon_{HbR}^{\lambda_1} \times OD^{\lambda_2}}{\varepsilon_{HbR}^{\lambda_2} \times \varepsilon_{HbO}^{\lambda_1} - \varepsilon_{HbR}^{\lambda_1} \times \varepsilon_{HbO}^{\lambda_2}}\right)\frac{1}{L} \qquad \text{(A.3)}$$

$$\left[HbR\right] = \left(\frac{\varepsilon_{HbO}^{\lambda_2} \times OD^{\lambda_1} - \varepsilon_{HbO}^{\lambda_1} \times OD^{\lambda_2}}{\varepsilon_{HbR}^{\lambda_1} \times \varepsilon_{HbO}^{\lambda_2} - \varepsilon_{HbR}^{\lambda_2} \times \varepsilon_{HbO}^{\lambda_1}}\right)\frac{1}{L} \qquad \text{(A.4)}$$

From eqs. A.3 and A.4, changes in [HbO] and [HbR] can be given as

$$\Delta\left[HbO\right] = \left(\frac{\varepsilon_{HbR}^{\lambda_2} \times \Delta OD^{\lambda_1} - \varepsilon_{HbR}^{\lambda_1} \times \Delta OD^{\lambda_2}}{\varepsilon_{HbR}^{\lambda_2} \times \varepsilon_{HbO}^{\lambda_1} - \varepsilon_{HbR}^{\lambda_1} \times \varepsilon_{HbO}^{\lambda_2}}\right)\frac{1}{L} \qquad \text{(A.5)}$$

$$\Delta[HbR] = \left(\frac{\varepsilon_{HbO}^{\lambda_2} \times \Delta OD^{\lambda_1} - \varepsilon_{HbO}^{\lambda_1} \times \Delta OD^{\lambda_2}}{\varepsilon_{HbR}^{\lambda_1} \times \varepsilon_{HbO}^{\lambda_2} - \varepsilon_{HbR}^{\lambda_2} \times \varepsilon_{HbO}^{\lambda_1}} \right) \frac{1}{L} \qquad \text{(A.6)}$$

$$\Delta[HbT] = \Delta[HbO] + \Delta[HbR] \qquad \text{(A.7)}$$

where ΔOD^{λ} is the change in optical density at a wavelength λ, and this is equal to log $(I_B)/(I_T)$, where I_B and I_T are the light intensities measured under baseline and transient conditions. The units for Δ[HbO], Δ[HbR], and Δ[HbT] are millimolar. In eqs. A.6 and A.7, the value of L is not a constant. It depends on the optical properties of the sample under investigation and also the source-detector separation. The path length, L, has been previously defined as L = d * DPF (Delpy et al, 1988). DPF stands for Differential Path Factor. DPF values are oxygenation and wavelength dependent and have been studied for muscles (Ferrari et al., 1992) and brain (van der Zee et al., 1992).

In this section, we aim to determine relative changes in hemoglobin derivatives using the equations above. The measurements were performed on the spinal cord of the rat when subject to electrical stimulation of the hind paw. The purpose of determining such changes is to determine the major contributor to the change in oxygen saturation percentage. From Johns et al., 2001, we know that oxygen saturation is defined as the ratio of oxygenated hemoglobin [HbO] to total hemoglobin [HbT] concentrations.

Knowledge of changes in hemoglobin derivatives would gives us a better insight into the underlying physiological actions.

A.2 Materials and Methods

A.2.1 Subjects and Surgical Methods

This is explained in Section 4.2.1

A.2.2 Experimental Set-up

The experimental set up has been explained in Section 2.2.1.2.

A.2.3 Data acquisition

This is explained in Section 4.2.3.

A.2.4 Data Analysis for Relative Changes

The goal of this study was to determine relative changes of hemoglobin derivatives in the rat spinal cord during peripheral stimulation. To achieve this, we make use of eqs. A.5 to A.7. For our purpose, we use wavelengths of 720 and 820 nm. The extinction coefficients of [HbO] and [HbR] at these wavelengths are put in the above equations. They have been previously published and extensively used (Zijlstra et al., 1991). The reflectance data at the two wavelengths are used to obtain ΔOD. The data ([HbO], [HbR], and [HbT]) are represented as Mean ± Standard Error of Mean. To determine changes between baseline and stimulation, we calculate the difference between stimulation and baseline values of the hemoglobin derivatives, i.e. $[HbO]_{stim} - [HbO]_{base}$ where $[\ ]_{base}$ refers to the last 20 seconds of the baseline period and $[\ ]_{stim}$ refers to the 20 seconds stimulation period.

A.2.5 Data Analysis for Oxygen Saturation Changes

The method for relating oxygen saturation and relative changes in hemoglobin derivative concentrations have been explained earlier (Kim et al., 2003). Based on it, we define oxygen saturation (sO_2) in the baseline period as $(sO_2)_{base}$ and during stimulation as $(sO_2)_{stim}$. From the definition of oxygen saturation, we get

$$\left(sO_2\right)_{base} = \left(\frac{[HbO]_{base}}{[HbT]_{base}}\right) \tag{A.8}$$

$$\left(sO_2\right)_{stim} = \left(\frac{[HbO]_{stim}}{[HbT]_{stim}}\right) \tag{A.9}$$

where $[HbO]_{base}$ and $[HbO]_{stim}$ correspond to values of relative changes in oxygenated hemoglobin concentration at baseline and stimulation periods respectively. From eqs. A.8 and A.9, change in oxygen saturation can be obtained as

$$\Delta\left(sO_2\right) = \left(\left(sO_2\right)_{stim} - \left(sO_2\right)_{base}\right) \tag{A.10}$$

Eq. A.10 can be rewritten as

$$\Delta\left(sO_2\right) = \left(\frac{[HbO]_{stim}}{[HbT]_{stim}} - \frac{[HbO]_{base}}{[HbT]_{base}}\right) \tag{A.11}$$

Changes in oxygen saturation (ΔsO_2) are tabulated as Mean ± Standard Error of Mean.

A.3 Experimental Results

A.3.1 Relative Changes in Hemoglobin Derivatives

Eight rats were used for this experiment. Based on the analysis described in the section above, the values of relative changes of [HbO], [HbR], and [HbT] for each animal are tabulated. The bar graphs of the mean values of the hemoglobin derivatives are shown in Figures A.3, A.4, and A.5 for [HbO], [HbR], and [HbT] respectively. We can see a decrease in the concentrations of hemoglobin derivatives during the stimulation as compared to the baseline.

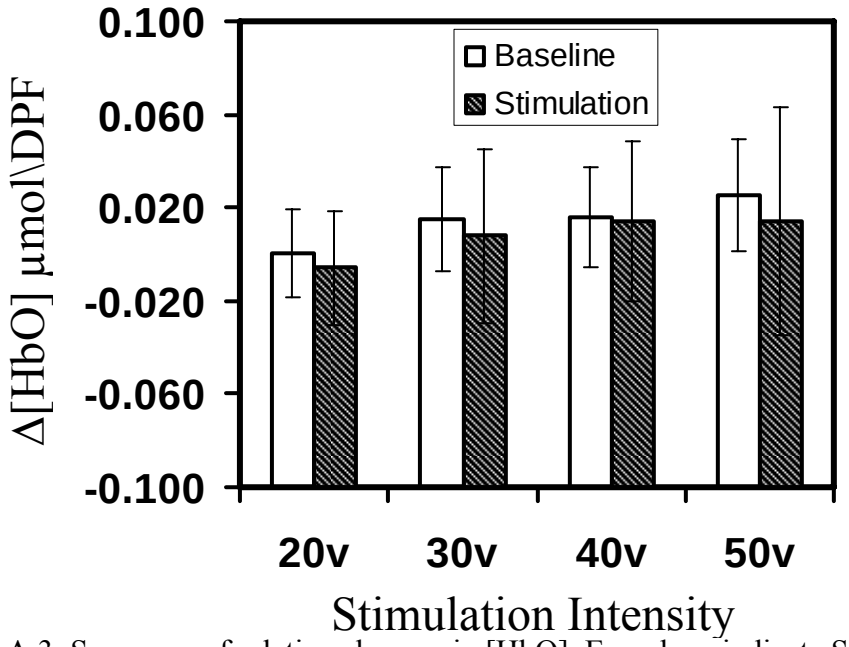

Figure A.3: Summary of relative changes in [HbO]. Error bars indicate SEM.

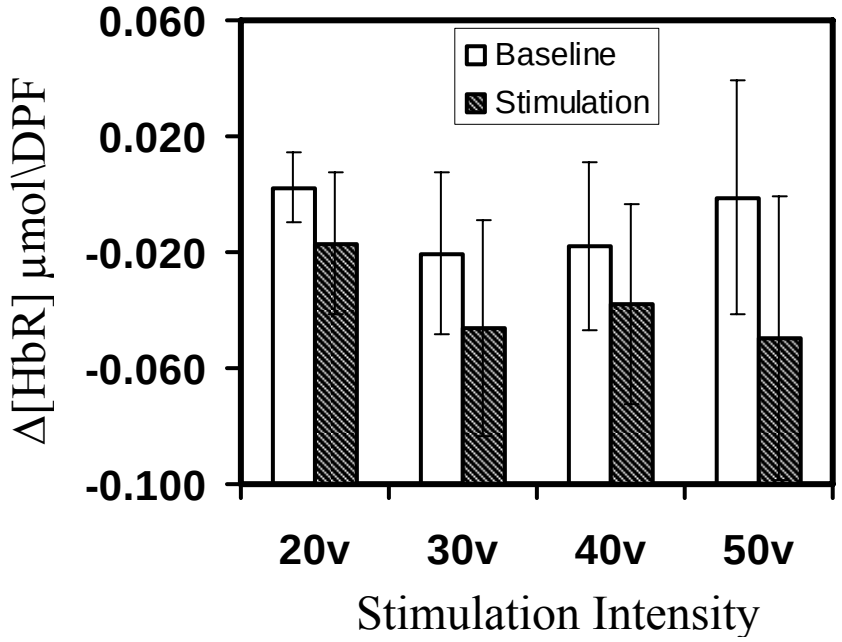

Figure A.4: Summary of relative changes in [HbR]. Error bars indicate SEM.

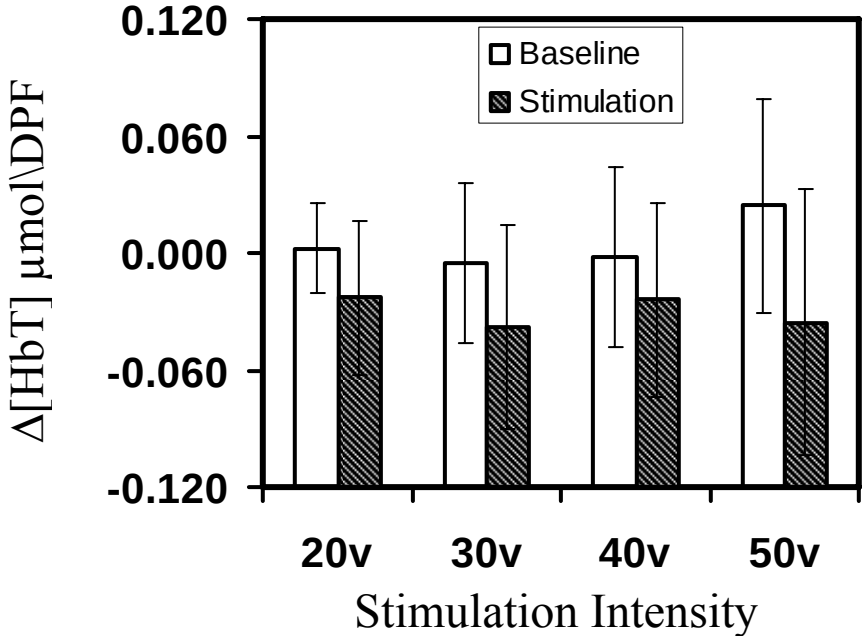

Figure A.5: Summary of relative changes in [HbT]. Error bars indicate SEM.

We did a simple students t-test to check for statistical differences in the values of relatives changes in hemoglobin derivatives between baseline and stimulation. The results showed no statistical difference between baseline and stimulation ($p > 0.15$). To detect differences, we subtracted the values of baseline ($[\ ]_{base}$) from the values of stimulation ($[\ ]_{stim}$). We did not find any set pattern in the changes of hemoglobin derivatives. The differences for 20, 30, 40, and 50 V stimulations are tabulated in Tables A.1 - A.4 respectively. They are also summarized in Figures A.5 – A.9 for the 4 different stimulations.

Table A.4: Differences in concentrations of hemoglobin derivatives between baseline and stimulation at 20V stimulation

	20V		
	HbO	**HbR**	**HbT**
1	0.028	0.087	0.115
2	-0.053	-0.050	-0.103
3	-0.030	-0.057	-0.087
4	-0.017	-0.080	-0.096
5	0.007	0.007	0.014
6	0.003	-0.036	-0.033
7	0.002	-0.025	-0.023
8	0.011	-0.002	0.009
Mean	-0.010	-0.030	-0.040
SEM	0.008	0.011	0.018

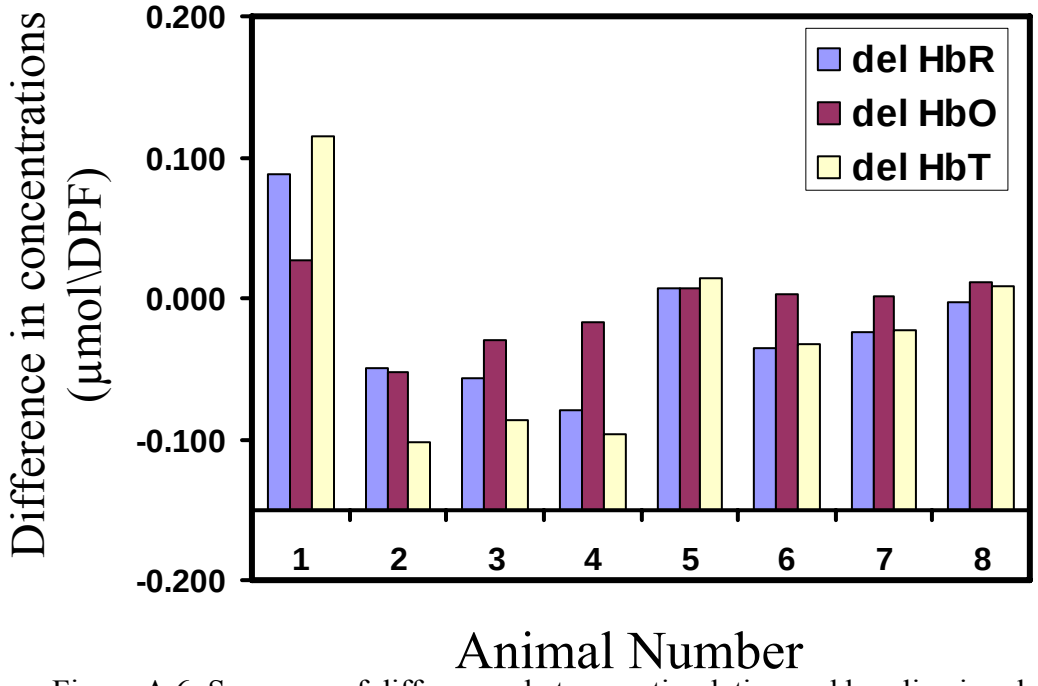

Figure A.6: Summary of differences between stimulation and baseline in relative changes in hemoglobin derivatives for 20V stimulation.

Table A.2: Differences in concentrations of hemoglobin derivatives between baseline and stimulation at 30V stimulation

	30V		
	HbO	**HbR**	**HbT**
1	0.053	0.063	0.116
2	0.008	-0.054	-0.046
3	-0.001	-0.056	-0.056
4	-0.039	-0.041	-0.080
5	-0.023	-0.005	-0.028
6	-0.040	-0.032	-0.072
7	-0.013	-0.022	-0.035
8	-0.001	-0.059	-0.060
Mean	-0.014	-0.034	-0.047
SEM	0.007	0.007	0.007

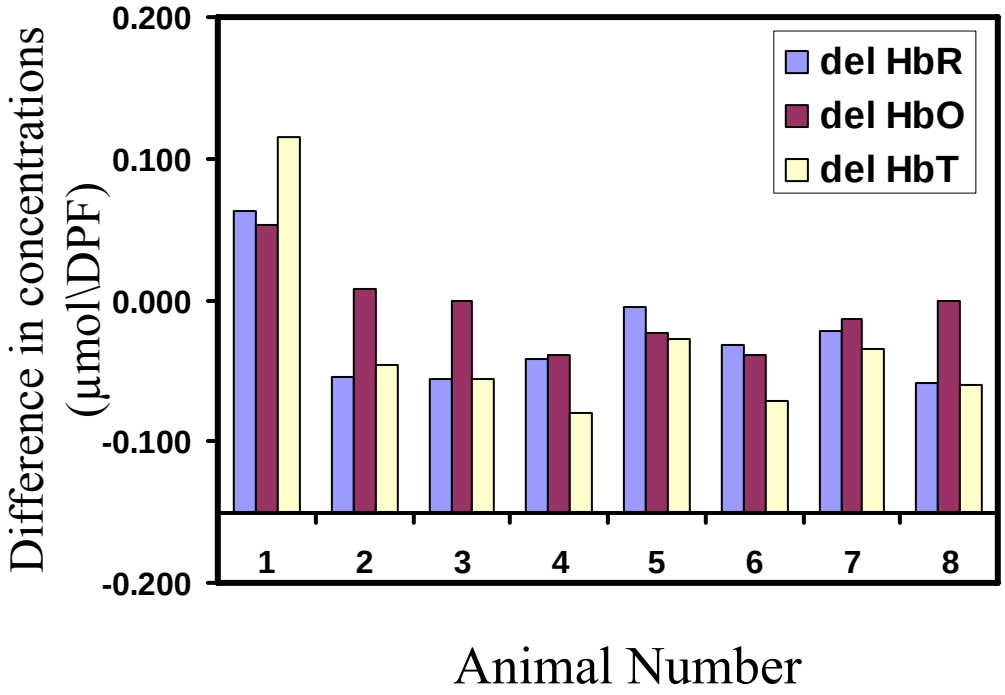

Figure A.7: Summary of differences between stimulation and baseline in relative changes in hemoglobin derivatives for 30V stimulation.

Table A.3: Differences in concentrations of hemoglobin derivatives between baseline and stimulation at 40V stimulation

	40V		
	HbO	**HbR**	**HbT**
1	0.040	0.076	0.116
2	-0.002	-0.049	-0.050
3	-0.006	-0.070	-0.076
4	0.002	0.007	0.009
5	-0.002	-0.007	-0.010
6	-0.065	-0.058	-0.124
7	0.018	-0.007	0.011
8	0.003	-0.053	-0.050
Mean	-0.007	-0.030	-0.036
SEM	0.010	0.012	0.017

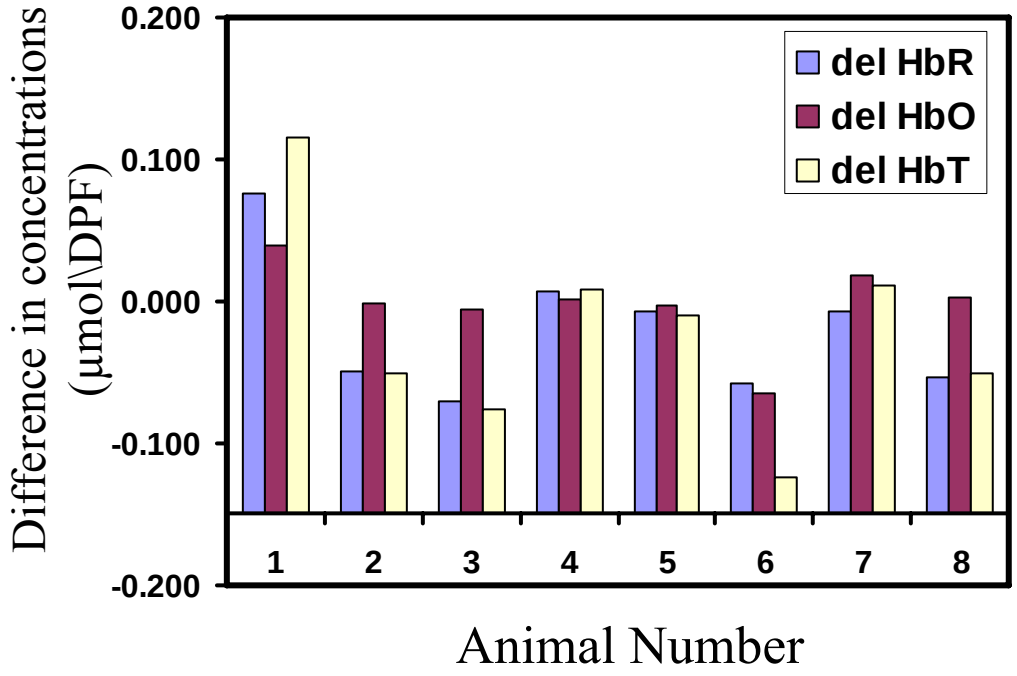

Figure A.8: Summary of differences between stimulation and baseline in relative changes in hemoglobin derivatives for 40V stimulation.

Table A.4: Differences in concentrations of hemoglobin derivatives between baseline and stimulation at 50V stimulation

	50V		
	HbO	**HbR**	**HbT**
1	0.044	0.093	0.137
2	-0.010	-0.038	-0.048
3	-0.010	-0.066	-0.076
4	-0.019	0.015	-0.004
5	-0.020	-0.047	-0.067
6	-0.010	-0.043	-0.053
7	-0.063	-0.262	-0.324
8	-0.002	-0.041	-0.043
Mean	-0.017	-0.060	-0.077
SEM	0.007	0.011	0.038

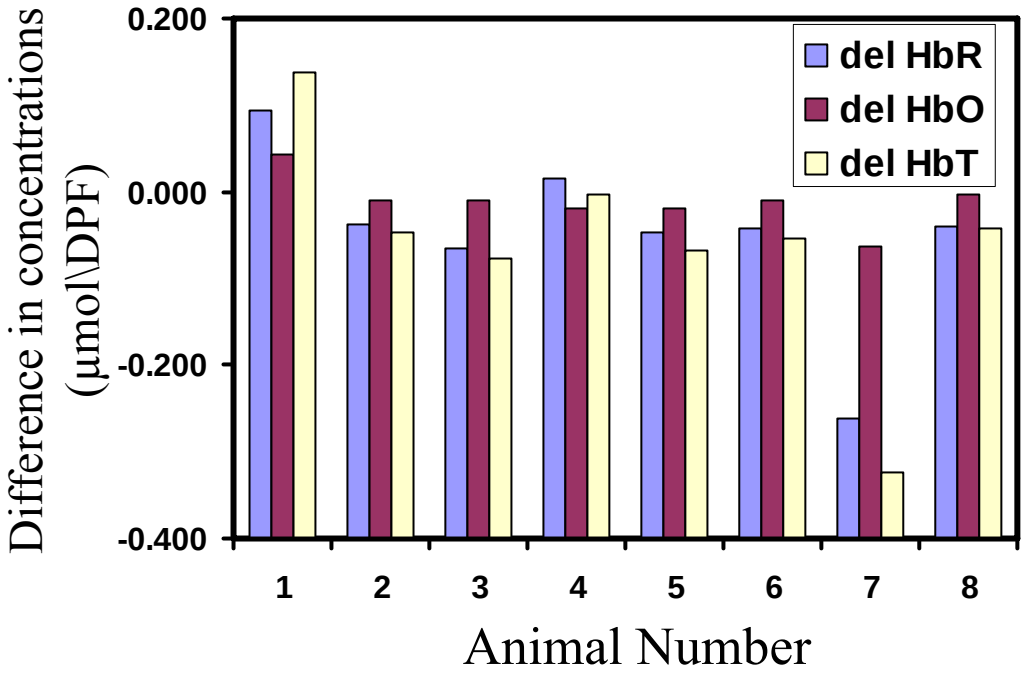

Figure A.9: Summary of differences between stimulation and baseline in relative changes in hemoglobin derivatives for 50V stimulation.

A.3.2 Changes in Hemoglobin Oxygen Saturation

The differences seen in Tables A.1 to A.4 do not directly give us any conclusion in the changes in oxygen saturation percentage. From eq. A.11, we calculate values of oxygen saturation as seen in Table A.5. There is a column of baseline values in Table A.4. These values are with respect to the first data point obtained during data acquisition. Therefore, the values need to be interpreted as changes in oxygen saturation with respect to the first point. The data is plotted in Figure A.10.

Table A.5: Oxygen saturation values obtained from hemoglobin derivative values.

	20v		30v		40v		50v	
	Baseline	**Stim**	**Baseline**	**Stim**	**Baseline**	**Stim**	**Baseline**	**Stim**
1	0.372	0.196	0.125	0.370	0.268	0.325	0.952	0.390
2	-0.332	0.314	0.127	0.053	-0.009	0.003	-0.148	-0.042
3	1.796	0.584	2.589	0.678	2.658	0.541	0.135	0.138
4	0.557	0.350	0.352	0.392	0.367	0.374	0.335	0.404
5	0.545	0.541	0.508	0.446	0.456	0.468	0.451	0.553
6	0.935	2.276	0.904	3.382	0.831	-1.384	0.772	1.854
7	0.077	-0.122	0.841	0.159	0.478	-0.098	0.599	0.219
8	3.863	9.777			1.407	6.744	1.285	3.958
Mean	0.977	1.739	0.778	0.783	0.807	0.872	0.548	0.934
SEM	0.468	1.176	0.324	0.440	0.304	0.867	0.162	0.478

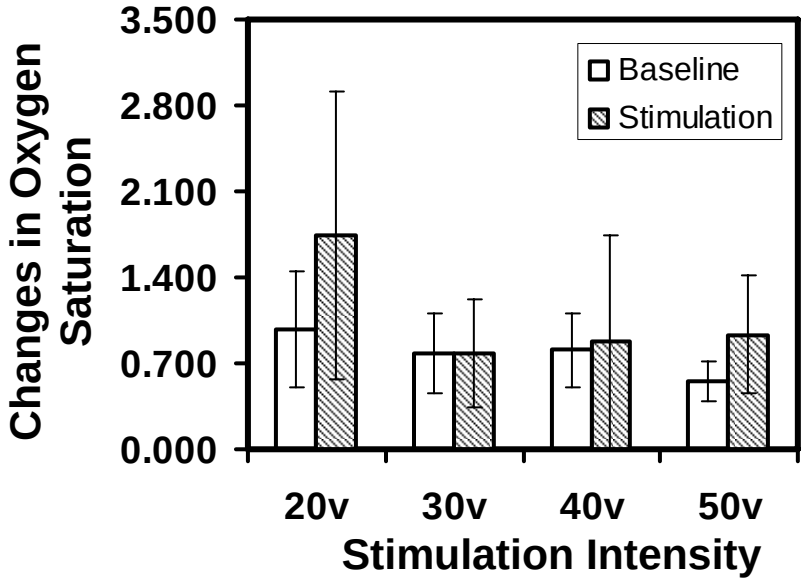

Figure A.10: Values of oxygen saturation during baseline and stimulation induced by electrical stimulation. The error bars indicate standard error of mean.

We did a students t-test between the saturation values of baseline and stimulation. We did not find any statistical difference between the two sets. The p-values were 0.36, 0.99, 0.93, and 0.94 for 20, 30, 40, and 50 V respectively. We then

calculated the net change in the values of oxygen saturation between baseline and stimulation. These are tabulated in Table A.6 and plotted in Figure A.11.

Table A.6: Difference in oxygen saturation based on hemoglobin derivative values

	20v	**30v**	**40v**	**50v**
1	-0.176	0.245	0.057	-0.562
2	0.646	-0.074	0.012	0.106
3	-1.212	-1.911	-2.117	0.003
4	-0.207	0.039	0.007	0.069
5	-0.004	-0.062	0.011	0.102
6	1.341	2.478	-2.215	1.082
7	-0.199	-0.682	-0.576	-0.380
8	5.914		5.337	2.673
Mean	0.763	0.005	0.065	0.387
SEM	0.781	0.464	0.826	0.369

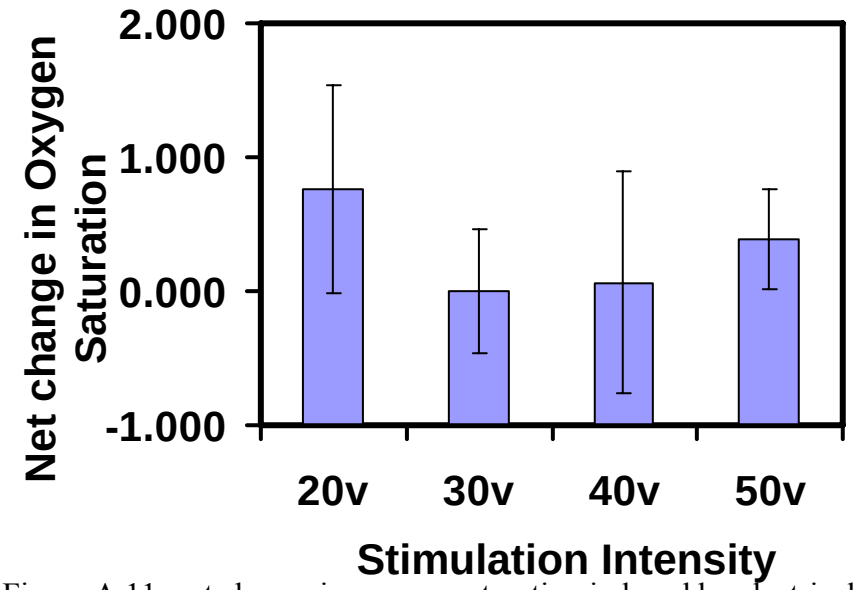

Figure A.11: net change in oxygen saturation induced by electrical stimulation. The error bars indicate standard error of mean.

A.4 Discussion

The goal of our study was to determine relative changes in concentrations of hemoglobin derivatives, namely, oxygenated hemoglobin [HbO] and deoxygenated

hemoglobin [HbR] on the rat spinal cord during peripheral electrical stimulation. To achieve this, we have analyzed the optical reflectance spectra in the NIR region. In the NIR region, there is a dominance of scattering in the sample, but there are changes that could be detected due to absorption. Changes due to absorption or blood-sensitive measurements may not be very conclusive in this region due to the fact that in the NIR range light scattering is predominant over light absorption, and a small source-detector fiber probe with a few hundred microns would be much sensitive to light scattering than light absorption (Johns et al., 2005).

In this study, we have only taken into consideration oxy- and deoxy-hemoglobin. They have distinct absorption spectra in the visible and NIR regions. Myoglobin and cytochromes are the other absorbing materials found in these regions. Myoglobin could be excluded as it is found dominantly in skeletal muscles and cytochrome concentration is several orders in magnitude lesser than the hemoglobin concentrations. These omissions contribute to about a 5% error for oxygen saturation measurements in the visible range (Johns et al., 2001).

Currently, in fNIR brain imaging, hemodynamic parameters such as [HbO] and [HbR] are quantified based on the modified Beer-Lambert's law, which depends on the measurements of overall variations in light intensities reflected from the human head (Yodh and Boas, 2003). The primary reason behind using such an approach is that it is theoretically impossible to separate light scattering and absorption using continuous-wave (CW) light with single source-detector separation and only several discrete wavelengths.

We have tried to utilize the same approach for our study. The results may not be a direct indication of the underlying physiology. From Tables A.1 to A.4, we see a decrease in the values of hemoglobin derivative concentrations during stimulation period as compared to the baseline. A negative [HbO] could be indicative of increased oxygen consumption. This is supported by the fact that there is a drop in the [HbT] values too. [HbT] is a proportional measure to blood flow. It is well known that there is an increased blood flow during such neuronal activations. The negative [HbT] could also be due to oxygen consumption and does not imply less blood flow.

We have also measured oxygen saturation as a function of the hemoglobin derivative concentrations. Our aim was to see the effect of individual hemoglobin components towards changes in oxygen saturation. In the previous chapter, we had utilized the visible spectroscopy to quantify hemoglobin oxygen saturation since both oxy- and deoxy- hemoglobin absorption bands between 500 -600 nm have large and distinct features, allowing us to fit an empirically calibrated equation to obtain SO_2 values for the rat spinal cord with the same small source-detector fiber probe. The oxy- and de-oxy hemoglobin derivatives do not have the same distribution in the NIR region. This could possibly be the reason for us not detecting changes during stimulation.

One main issue for such discrepancies could be the area sampled by the incident light. From prior publications, we have shown that the 'Look Ahead Distance' (LAD), the measure of the depth up to which light could penetrate through using our needle probe, is estimated around 1.2 to 1.5 mm (Giller et al., 2003; Gurnani, 2003; Qian et al., 2003). Taking into account the dimensions of the lumbar segment of the spinal cord and

the thickness of white matter, it is possible that the light could penetrate up to the gray matter depths. This would vary greatly depending on anatomical differences between animals, and this issue is beyond the scope of this current study.

In our study, there exist experimental variations possibly caused by 1) subject-to-subject variability in spinal cord anatomy, 2) position of dorsal roots when they enter the spinal cord, and 3) slight body movement due to respiration. Issue regarding inter-subject variability has been previously reported (Sato et al., 2005). In summary, using simple and robust instrumentation, we have attempted to show changes in hemoglobin derivative concentrations in the NIR regions using modified Beer-Lambert's law. Our results do not conclusively prove the actual physiological changes. More work on development of algorithms is needed to show the changes.

APPENDIX B

SLOPE ALGORITHM

Screen shot of LabView™ interface for data acquisition

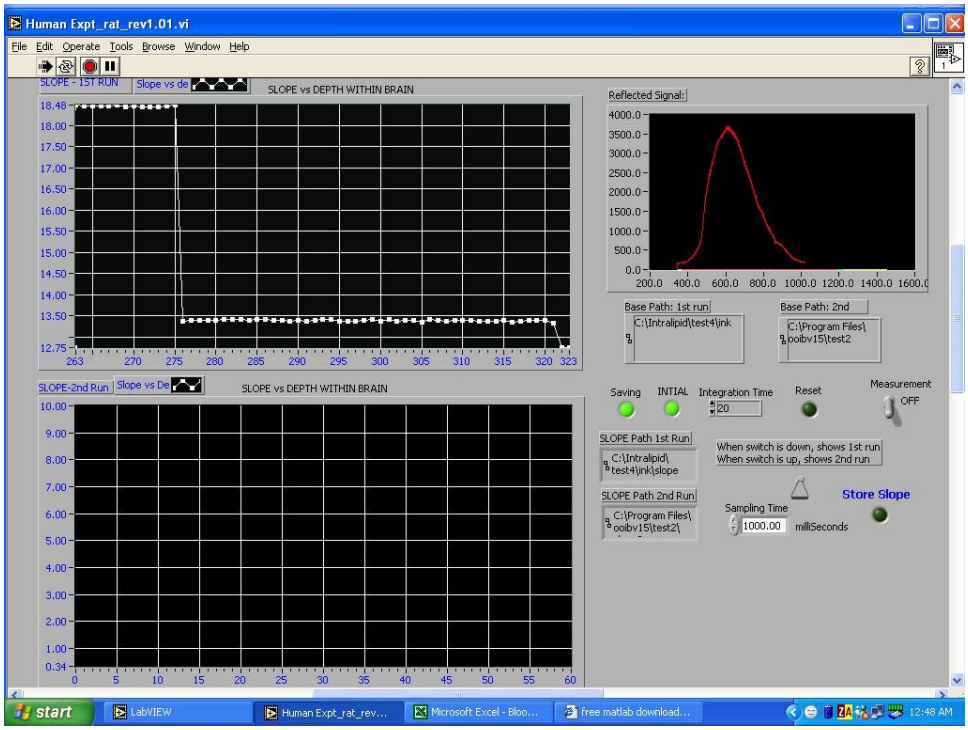

APPENDIX C

MATLAB® CODES

1. **Program to obtain slope: μ_s'**

```
clear all;
close all;
clc

%To read the data file
total1=2048;
for i=1:total1
  jj=i;
  kk=int2str(jj)
  end
  filename=kk;
  filename1=strcat('C:\Harsha\Data\test2\',kk);
  fr=fopen(filename1,'r');
  aaa=fscanf(fr,'%g',[1,inf]);
  fclose(fr);
  for p=1:2048
    aa(p)=aaa(p*2);
    lam(p)=aaa(p*2-1);
    end
  bbb(:,i)=aa';

%To Calculate Slope
sss=0;
for j=1:total1
  sss=0;
  for i=441:879
  sss=sss+bbb(i,j);
  end
  aver550(j)=sss;

   sump1=0;
   sump2=0;
   sump3=0;
   sump4=0;

   for jj=1:471
      sump1=sump1 +(lam(jj+1030)*bbb(jj+1030,j));
      sump2=sump2 + lam(jj+1030);
      sump3=sump3+ bbb(jj+1030,j);
      sump4=sump4 + (lam(jj+1030)^2);
   end
   slope1(j)=-(((471*sump1)- (sump2*sump3))/((471*sump4)-(sump2*sump2)));
```

```
   mean(slope1(j));

end

%Write into a file
fid= fopen('filename.txt','a');
fprintf(fid, '%13.6f \t',mean(slope1(j)));
fprintf(fid, '\n');
fclose(fid);
end
```

2. **Program to obtain μ_s'**

```
clear all;
close all;
clc

% to read the input reflectance data file
n= 60;%input('\n Reflectance Data \n Enter the number of measurements taken \n');
p=0; %input('\n Enter the starting number of the file\n');

% base path where the data files are stored
base='D:\November\28TH NOV 2003 - RAT 3 - IN VIVO\test10\';
refcal=zeros(2048,1);
for i=p:(p+n-1)
   kk=int2str(i);
   s=strcat(base,kk);
   arr=load (s);

   % find the number of rows
   len=length(arr);

   % Extract data from the two dimensional array
   dat=arr(:,2);
   refcal=dat+refcal;
end
refcal=refcal/n;

% to read the calibration data
ncal=61; %input('\n Calibration Data \n Enter the number of  calibration measurements
taken\n');
p= 0 ;%input('\n Enter the starting number of the file\n');
calibcal=zeros(2048,1);

% Path where the calibration data has been stored
base='D:\November\28TH NOV 2003 - RAT 1 - IN VIVO\Calibration\';
for i=p:(p+ncal-1)
   kk=int2str(i);
   s=strcat(base,kk);
   arr_cal=load (s);

   % find the number of rows
   len=length(arr);

   % Extract data from the two dimensional array
   dat1=arr_cal(:,2);
```

```
   calibcal=dat1+calibcal;
end
calibcal=calibcal/ncal;

% To divide the calibration data and the measured reflectance data
for i=1:2048
      ref(i)=refcal(i)/calibcal(i);
end

% extract wavelength information
wav=arr(:,1);

% to calculate the μs' value
for i=1:len
    mus(i) = (((ref(i)/0.0035) + 1.5437)/1.6696);
end

%to write the result in to a file
fid=fopen(filename.txt','w');
for i = 1:len
%fprintf(fid,'%12.6f \n',wav);
  fprintf(fid,'%12.6f \n',mus(i));
end
fclose(fid);
```

3. **Program to obtain Oxygen Saturation Percentage**

```
function left_lumbar_rev4
global m1;
global n1;
global XDATA_1;
global ehb_1;
global ehb02_1;
global lambda_low
global lambda_high


%Define lower limit of wavelength
lambda_low = 500.00;

%Define upper limit of wavelength
lambda_high = 600.00;

%Read first set of calibration data
fid = fopen('21ST AUG 2004_calib4.txt','r');
Ref1 = read_sort(fid);

%Read first set of calibration data
fid = fopen('21ST AUG 2004_calib4.txt','r');
Ref2 = read_sort(fid);

%Read first set of calibration data
fid = fopen('21ST AUG 2004_calib4.txt','r');
Ref3 = read_sort(fid);

%Read first set of calibration data
Ref_avg = (Ref1(:,2) + Ref2(:,2) + Ref3(:,2))./3;

%Read first set of calibration data
fid = fopen('18TH DEC 2003 - RAT 1_test9.txt','r');
Hb = read_sort(fid);

%Create a vector comprising of only wavelength, we assume that the step length in
%lambda remains the same for all the reference data and test data
XDATA = Ref1(:,1);
XDATA_1 = XDATA(1);
```

```
%Eliminate spectral effects
Hb_spectral = Hb(:,2)./ Ref_avg;

%Normalize the above data
YDATA = Hb_spectral./Hb_spectral(1);

%Enter the extinction coeficients for interpolation
lam = [500 510 520 530 538 540 542 550 554 560 568 570 576 580 590 600];

% Extinction coeffs for Rats
ehb = [4.5 5.5 6.57 8.19 10.17 10.75 11.33 13.09 13.38 13.03 11.83 11.46 10.27 9.43
6.86 3.64];
ehb02 = [5.32 5.04 6.15 10.62 14.21 14.65 14.81 12.18 10.29 8.87 10.68 11.91 15.72
14.94 4.29 1];

%Define extinction coeficients value for normalized lambda
ehb_1 = interp1(lam,ehb,XDATA(1));
ehb02_1 = interp1(lam,ehb02,XDATA(1));

%Interpolate extinction coefficients
n1 = interp1(lam,ehb,XDATA);
m1 = interp1(lam,ehb02,XDATA);

%use these set of commands for using Non-linear least square fitting
opt =
optimset('LargeScale','on','DerivativeCheck','off','Display','iter','LevenbergMarquardt','on'
,'MaxFunEvals',10000,'MaxIter',10000,'TolFun',1e-20,'TolX',1e-10,'TolCon',1e-10)

% Since we are dealing with Ill conditioned problem, turn off warning messages.
%warning off

lb=[1e-8 1e-8 1e-8];
hb=[100 100 100];
[Estimates, resnorm] =
lsqnonlin(@fit_simp,[0.00001;0.1;0.0005],[],[],opt,XDATA,YDATA);

%Define numerator terms
first_term1a = (1 - Estimates(1).*XDATA);
first_term = first_term1a.^2;
sec_term2a = ((Estimates(2).*m1) + (Estimates(3).*n1)).*3;
sec_term = 1 + ((sec_term2a./first_term1a).^0.5);
third_term = exp(-((sec_term2a./first_term1a).^0.5));
NUM = (first_term.*sec_term.*third_term);
```

%Define Denominator terms

```
denom1a = (1 - Estimates(1).*XDATA_1);
denom1 = (denom1a).^2;
denom2a = ((Estimates(2).*ehb02_1) + (Estimates(3).*ehb_1)).*3;
denom2 = 1 + ((denom2a./denom1a).^0.5);
denom3 = exp(-((denom2a./denom1a).^0.5));
DEN = (denom1.*denom2.*denom3);

YDATA_NEW = NUM./DEN;
plot(XDATA,YDATA,'o')
hold on
plot(XDATA,YDATA_NEW,'r','LineWidth',2)
residues = YDATA - YDATA_NEW;
plot(XDATA,residues,'+');
legend('measured data','fitted data','residues');
oxy_level = (Estimates(2)./(Estimates(2) + Estimates(3)))*100
```

%Routine to sort data

```
function selected_data = read_sort(fid);
global lambda_low
global lambda_high

%Eliminate header
header1 = fgetl(fid);

%Eliminate header variables
header2 = fgetl(fid);
raw_data_rows = fscanf(fid,'%f',[2,inf]);
status = fclose(fid);
raw_data_columns = raw_data_rows';

%locate the index for wavelength corresponding to Lambda_low
i = 1;
while(raw_data_columns(i,1) < lambda_low);
   i = i + 1;
end

%Locate the index for wavelength corresponding to Lambda_high
j = i;
while(raw_data_columns(j,1) < lambda_high);
   j = j + 1;
end
```

```
%Create a new data matrix for the given wavelength band
k = 1;
for ii=i:j-1;
   selected_data(k,:) = raw_data_columns(ii,:);
   k = k + 1;
end
```

%Routine for curve fitting

```
function diff = fit_simp(params,Input,Actual_Output)
global m1;
global n1;
global XDATA_1;
global ehb_1;
global ehb02_1;
Z = params(1);
X = params(2);
Y = params(3);

term1a = (1 - Z.*Input);
term1 = term1a.^2;
term2a = ((X.*m1) + (Y.*n1)).*3;
term2 = 1 + ((term2a./term1a).^0.5);
term3 = exp(-((term2a./term1a).^0.5));
NUM_f = (term1.*term2.*term3);

termn1a = (1 - Z.*XDATA_1);
termn1 = termn1a.^2;
termn2a = ((X.*ehb02_1) + (Y.*ehb_1)).*3;
termn2 = 1 + ((termn2a./termn1a).^0.5);
termn3 = exp(-((termn2a./termn1a).^0.5));
DEN_f = termn1.*termn2.*termn3;

Fitted_Curve = NUM_f./DEN_f;

diff = Fitted_Curve - Actual_Output;
sse = sum(diff.^2)

% When curvefitting, a typical quantity to minimize is the sum of squares error
```

REFERENCES

1. Aitken, P.G., Fayuk, D., Somjen, G.G., and Turner, D.A., 1999. Use of Intrinsic Optical Signals to Monitor Physiological Changes in Brain Tissue Slices. Methods: A Companion to Methods in Enzymology **18**, 91-103.

2. Andrew, R.D., Jarvis, C.R., and Obeidat, A.S., 1999. Potential Sources of Intrinsic Optical Signals Imaged in Live Brain Slices. Methods: A Companion to Methods in Enzymology **18**, 185-196.

3. Arai, Y., Momose-Sato, Y., Sato, K., and Kamino, K., 1999. Optical mapping of neural network activity in chick spinal cord at an intermediate stage of embryonic development. J. Neurophysiol. **81**, 1889-1902.

4. Asato, F., Butler, M., Blomberg, H., and Gordh, T., 2000. Variation in rat sciatic nerve anatomy: implications for a rat model of neuropathic pain. J Peripher Nerv Syst. **5**, 19-21.

5. Baldissera, F., Hultborn, H., and Illert, M., 1981. Integration in spinal neuronal systems in *Handbook of Physiology*: The Nervous System, J. M. Brookhart, V. B. Mountcastle, V. B. Brooks, and S. R. Geiger, eds., Am. Physiol. Soc., Bethesda, 509-595.

6. Benesch, R., Macduff, D., and Benesch, R.E., 1965. Determination of oxygen equilibria with a versatile new tonomter. Anal. Biochem. **11**, 81-87.

7. Benesch, R.E, Benesch, R., and Yung, S., 1973. Equations for the spectrophotometric analysis of hemoglobin mixtures. Anal. Biochem. **55**, 245-248.

8. Bevilacqua, F., Piguet, D., Marquet, P., Gross, J.D., and Tromberg, B.J., 1999. In vivo local determination of tissue optical properties: Applications to Human Brain. Appl. Opt. **38**, 4939-4950.

9. Bradley, J., MacIntosh, L., Klassen, M., and Menon, R.S., 2003. Transient hemodynamics during a breath hold challenge in a two part functional imaging study with simultaneous near-infrared spectroscopy in adult humans. NeuroImage **20**, 1246–1252.

10. Cheong, W., Prahl, S.A., and A. J. Welch, 1990. A review of the optical properties of biological tissues. IEEE J Quantum Electronics. **26**(12), 2166-2184.

11. Choi, J.H., Wolf, M., Toronov, V., Wolf, U., Polzonetti, C., Hueber, D., Safonova, L.P., Gupta, R., Michalos, A., Mantulin, W., and Gratton,E., 2004. Noninvasive determination of the optical properties of adult brain: near-infrared spectroscopy approach. J. Biomed. Opt. **9**(1), 221–229.

12. Clemence, A., Mirsky, R., and Jessen, K.R., 1989. Non-myelin forming Schwann cells proliferate rapidly during Wallerian degeneration in the rat sciatic nerve. J. Neurocytol. **18**, 185-192.

13. Cohen, L.B., 1973. Changes in neuron structure during action potential propagation and synaptic transmission. Physiol. Rev. **53**, 373-418.

14. Colacino, J.M., Grubb, B., and Jobsis, F.F., 1981. Infrared technique for cerebral blood flow. Comparison with ^{133}Xenon clearance. Neurol. Res. **3**, 17-31.

15. Delpy, D.T., Cope, M., van der Zee, P., Arridge, S., Wray, S., and Wyatt, J., 1988. Estimation of optical pathlength through tissue from direct time of flight measurement. Phys. Med. Biol. **33**, 1433-1442.

16. Doppenberg, E.M.R., Watson, J.C., Broaddus, W.C., Holloway, K.L., Young, H.F., and Bullock, R., 1997. Intraoperative mornitoring of substrate delivery during aneurysm and hemotoma surgery: initial experience in 16 patients. J Neurosurg. **87**, 809-816.

17. Dunn, A.K., Devor, A., Bolay, H., Andermann, M.L., Moskowitz, M.A., Dale, A.M., and Boas, D.A., 2003. Simultaneous imaging of total cerebral hemoglobin concentration, oxygenation, and blood flow during functional activation. Opt. Lett. **28**, 28-30.

18. Durduran, T., Choe. R., Culver, J.P., Zubkov, L., Holboke. M.J., Jiammarco, J., Chance, B., and Yodh, A.G., 2002. Bulk properties of healthy female breast tissue. Phys. Med. Biol. **47**, 2847-2861.

19. Edwards, A.D., Richardson, C., van der Zee, P., Elwell, C., Wyatt, J.S., Cope, Delpy, D.T., and Reynolds, E.O.R., 1993. Measurement of hemoglobin flow and blood flow by near-infrared spectroscopy. J. Appl. Physiol. **75**, 1884-1889.

20. Elwell, C.E., Owen-Reece, H., Cope, M., Wyatt, J.S., Edwards, A.D., Deply, D.T., and Reynolds, E.O.R., 1993. Measurement of adult cerebral hemodynamics using near infrared spectroscopy. Acta Neurochir. **59,** 74-80.

21. Farrell, T.J., Patterson, M.S., and Wilson, B., 1992. A diffusion theory model of spatially resolved, steady state diffuse reflectance for the non-invasive determination of tissue optical properties in vivo. Med. Phys. **19**, 879-888.

22. Ferrari, M., Wei, Q., Carraresi, L., De Blasi, R.A., and Zaccanti, G., 1992. Time resolved spectroscopy of human forearm. J Photochem. Photobiol. **16**, 141-153.

23. Fox, S.I., 1993. Human Physiology, 4th Edition, Wm. C Brown Publishers, Dubuque, IA.

24. Franceschini, M.A., Toronov, V., Filiaci, M.E., Gratton, E., and Fantini, S., 2000. On-line optical imaging of the human brain with 160-ms temporal resolution. Opt. Exp. **6**, 49-57.

25. Fukui, Y., Ajichi, Y., and Okada, E., 2003. Monte Carlo Prediction of Near-Infrared Light Propagation in Realistic Adult and Neonatal Head Models. Appl. Opt. **42**(16), 2881-2890.

26. Fuster, J., Guiou, M., Ardestani, A., Cannestra, A., Sheth, S., Zhou, Y., Toga, A., and Bodner, M., 2005. Near-infrared spectroscopy (NIRS) in cognitive neuroscience of the primate brain. NeuroImage **26**, 215-220.

27. Gardner, E.P., Martin, J.H., and Jessel, T.M., 2000. The bodily senses" in *Principles of Neural Science*, E. R. Kandel, J. H. Schwartz, and T. M. Jessel, eds., 4th ed., Mcgraw Hill, New York, pp. 430–450.

28. Gelderd, J.B. and Chopin, S.F., 1977. The vertebral level of origin of spinal nerves in the rat, Anat Rec, **188**, 45-47.

29. Germon, T., 2002. Intraoperative monitoring with near infrared spectroscopy. Spine **27**, 2850-2852.

30. Gias, C., Hewson-Stoate, N., Jones, M., Johnston, D., Mayhew, J.E., and Coffey, P.J., 2005. Retinotopy within rat primary visual cortex using optical imaging. NeuroImage **24**, 200– 206.

31. Giller, C.A., Johns, M., and Liu, H., 2000. Use of an intracranial near-infrared probe for localization during stereotactic surgery for movement disorders. J Neurosurg. **93**, 498-505.

32. Giller, C.A., Liu, H., Gurnani, P., Victor, S., Yazdani, U., and German, D.C., 2003. Validation of a near-infrared probe for detection of thin intracranial white matter structures. J Neurosurg. **98**, 1299-1306.

33. Gu, Y., Bourke, V., Kim, J.G., Constantinescu, A., Mason, R.P., and Liu, H., 2003. Dynamic response of breast tumor oxygenation to hyperoxic respiratory challenge monitored with three oxygen sensitive parameters. Appl. Opt. **42**, 2960-2967.

34. Gurnani, P.P., 2003. Near Infrared spectroscopic measurement of human and animal brain structures. Master Thesis, University of Texas at Arlington, TX.

35. Haller, M., Mironov, S.L., and Richter, D.W., 2001. Intrinsic Optical Signals in Respiratory Brain Stem Regions of Mice: Neurotransmitters, Neuromodulators, and Metabolic Stress. J. Neurophysiol. **86**, 412-421.

36. Hebden, J.C., Gibson, A., Yusof, R.M., Everdell, N., Hillman, E.M., Delpy, D.T., Arridge, S.R., Austin. T., Meek, J.H., and Wyatt, J.S., 2002. Three dimensional optical tomography of the premature infant brain. Phys. Med. Biol. **47**, 4155-4166.

37. Hebel, R., and Stromberg, M.W., 1996. Anatomy and Embryology of the laboratory rat. Biomed Verlag, Germany, pp 182-184.

38. Horecker, B.L., 1943. The absorption spectra of hemoglobin and its derivatives in the visible and near infrared regions. J. Biol. Chem. **148**, 173-183.

39. Hueber, D.M., Franceschini, M.A., Ma, H.Y., Zhang, Q., Ballesteros, J.R., Fantini, S., Wallace, D., Ntziachristos, V., and Chance, B., 2001. Non-invasive and quantitative near-infrared haemoglobin spectrometry in the piglet brain during hypoxic stress, using a frequency-domain multidistance instrument. Phys. Med. Biol. **46**, 41–62.

40. Ibrahim, S., Laude, E.A., Bee, D., Eaton, S., Ward, J.D., and Harris, N.D., 1999. Combined microlightguide spectrophotometry and microendoscopy for measurement of oxygen saturation in peripheral nerves. Physiol. Meas. **20**, 65-73.

41. Ikeda, J., Terakawa, S., Murota, S., Morita, I., and Hirakawa, K., 1996. Nuclear disintegration as a leading step of glutamate excitotoxicity in brain neurons. J. Neurosci. Res. **43**, 613-622.

42. Isobe, K., Kusaka, T., Fujikawa, Y., Kondo, M., Kawada, K., Yasuda, S., Itoh, S., Hirao, K., and Onishi, S., 2000. Changes in cerebral hemoglobin concentration and oxygen saturation immediately after birth in the human neonate using full-spectrum near infrared spectroscopy. J. Biomed. Opt. **5**, 283-286.

43. Jobsis, F.F., 1977. Noninvasive, infrared monitoring of cerebral and myocardial oxygen sufficiency and circulatory parameters. Science **198**, 1264-1267.

44. Johns, M., Giller, C.A., and Liu, H., 1998. Computational and In Vivo Investigation of Optical Reflectance from Human Brain to Assist Neurosurgery. J. Biomed. Opt. **3**, 437-445.

45. Johns, M., Giller, C.A., and Liu, H., 2001. Determination of hemoglobin oxygen saturation from turbid media using reflectance spectroscopy with small source detector separations. Appl. Spectroscopy **55**, 1686-1694.

46. M. Johns, 2003. Optical properties of living tissues determined in vivo using a thin fiber optic probe. PhD Dissertation, University of Texas at Arlington, TX.

47. Johns, M., Giller, C.A., German, D.C., and Liu, H., 2005. Determination of reduced scattering coefficient of biological tissue from a needle-like probe. Opt. Exp. **13**, 4828-4842.

48. Johnson, L.J., Hanley, D.F., and Thakor, N.V., 2000. Optical light scatter imaging of cellular and sub-cellular morphology changes in stressed rat hippocampal slices. J. Neurosci. Meth. **98**, 21-31.

49. Kariman, K., Jobsis, F.F., and Saltzman, H.A., 1981. Cytochrome aa3 reoxidation. Early indicator of metabolic recovery from hemorrhagic shock in rats. J. Clin. Invest. **72**, 180-191.

50. Kim, J.G., Song, Y., Zhao, D., Constantinescu, A., Mason, R.P., and Liu, H., 2003. Interplay of tumor oxygenation and tumor pO_2 observed using nar infrared spectroscopy, an oxygen needle electrode, and ^{19}F MR pO_2 mapping. J. Biomed. Opt. **8**, 53-62.

51. Kim, J.G., Xia, M., and Liu, H., 2005. Extinction coefficients of hemoglobin for near infrared spectroscopy of tissue. IEEE Eng. Med. Biol. Magazine **24**, 118-121.

52. Kim, J.G., 2005. Investigation of breast tumor hemodynamics by near infrared spectroscopy: applications to cancer therapy monitoring. PhD Dissertation, University of Texas at Arlington, TX.

53. Kim, S.H. and Chung, J.M., 1992. An experimental model for peripheral neuropathy produced by segmental spinal nerve ligation in the rat. Pain **50**, 355-363.

54. Kristal, B.S. and Dubinsky, J. M., 1997. Mitochondrial permeability transition in the central nervous system: induction by calcium cycling-dependent and – independent pathways. J. Neurochem. **69**, 524-538.

55. Kurth, C.D. and Thayer, W.S., 1999. A multiwavelength frequency domain near infrared Oximeter. Phy.Med.Biol. **44,** 727-740.

56. Lawrence, J., Stroman, P.W., Bascaramurty, S., Jordan, L.M., and Malisza, K.L., 2004. Correlation of functional activation in the rat spinal cord with neuronal activation detected by immunohistochemistry. Neuroimage **22**, 1802-1807.

57. Lemasters, J.J., Nieminen, A.L., Qian, T., Trost, L.C., and Herman, B., 1997. The mitochondrial permeability transition in toxic, hypoxic and reperfusion injury. Mol. Cell Biochem. **174**, 159-165.

58. Liu, H., Song, Y., Worden, K.L., Jiang, X., Constantinescu, A., and Mason, R.P., 2000. Non Invasive Investigation of blood oxygenation dynamics of tumors by near-infrared spectroscopy. App. Opt. **39,** 5231-5243.

59. Lubinska, L., 1997. Early course of Wallerian degeneration in myelinated fibres of the rat phrenic nerve. Brain Res. **130**, 47-63.

60. Lubinska, L., 1982. Patterns of Wallerian degeneration of myelinated fibres in short and long peripheral stumps and in isolated segments of rat phrenic nerve. Interpretation of the role of axoplasmic flow of the trophic factor. Brain Res. **233,** 227-240.

61. Macnab, A.J., Gagnon, R.E., and Gagnon, F.A., 2002. Near infrared spectroscopy for intraoperative monitoring of the spinal cord. Spine **27**, 17-20.

62. Malisza, K.L. and Stroman, P.W., 2002. Functional imaging of the rat cervical spinal cord. J Magn. Reson. Imaging **16**, 553–558.

63. Malisza, K.L., Stroman, P.W., Turner, A., Gregorish, L., Foniok, T., and Wright, A., 2003. Functional MRI of the rat lumbar spinal cord involving painful stimulation and the effect of peripheral joint mobilization. J Magn. Reson. Imaging **18**, 152–159.

64. Malonek, D. and Grinvald, A., 1997. Vascular regulation at sub millimeter range. Adv. Exp. Med. Bio. **1413**, 215-219.

65. Marder, E., and Calbrese, C., 1996. Principles of rhythmic motor pattern generation. Physiol. Rev. **76**, 687-717.

66. Matcher, S.J., Cope, M., and Delpy, D.T., 1997. In vivo measurements of the wavelength dependence of tissue scattering coefficients between 760 and 900 nm measured with time-resolved spectroscopy. Appl. Opt. **36**, 386-396.

67. Maxim, P.G., Carson, J.J.L., Benaron, D.A., Loo,Jr., B.W., Xing, L., Boyer, A.L., and Friedland, S., 2005. Optical detection of tumors in vivo by visible light tissue oximetry. Tech Cancer Res Treat. **4**, 227-234.

68. Miller, L.D., Petrozzina, J.J., Mahanty, N.K., and Connor, J.A., 1993. Optical imaging of cytosolic calcium, electrophysiology, and ultrastructure in pyramidal neurons of organotypic slice cultures from rat hippocampus. Neuroimage **1**, 109-120.

69. Mira, J.C., 1976. Quantitative studies on the regeneration of myelinated nerve fibers. II. Variation on the number and size of regenerating nerve fibers after localized crushing or total section. Arch Anat Microsc. Morphol. Exp. **65**, 255-284.

70. Mochida, H., Sato, K., Arai, Y., Sasaki, S., Kamino, K., and Momose-Sato, Y., 2001. Optical imaging of spreading depolarization waves triggered by spinal nerve stimulation in the chick embryo: Possible mechanisms for large-scale coactivation of the CNS. Eur. J. Neurosci. **14**, 809-820.

71. Mochida, H., Sato, K., Arai, Y., Sasaki, S., Yazawa, I., Kamino, K., and Momose-Sato, Y., 2001. Multiple-site optical recording reveals embryonic organization of synaptic networks in the chick spinal cord. Eur. J. Neurosci. **13**, 1547-1558.

72. Mook, P.H., Proctor, H.J., Jobsis, F.F., and Wildevuur, Ch.R.H., Assessment of brain oxygenation: A comparison between an oxygen electrode and near infrared spectrophotometry. Adv. Exp. Med. Biol. **169**, 841-847.

73. Morren, G., Wolf, U., Lemmerling, P., Wolf, M., Choi, J.H., Gratton, E., De Lathauwer, L., and Van Huffel, S., 2004. Detection of fast neuronal signals in the motor cortex from functional near infrared spectroscopy measurements using independent component analysis. Med. Biol. Eng. Comp. **42**, 92-99.

74. Mourant, J.R., Bigio, I.J., Boyer, J., Conn, R.L., Johnson, T., and Shimada, T., 1995. Spectroscopic diagnosis of bladder cancer with elastic light scattering. Lasers Surg. Med. **17**, 350–357.

75. Mourant, J.R., Bigio, I.J., Boyer, J., Johnson, T.M., Lacey, J., Bohorhoush, A.G., and Mellow, M., 1996. Elastic Scattering Spectroscopy as a Diagnostic Tool for Differentiating Pathologies in the Gastrointestinal Tract: Preliminary Testing. J. of Biomed. Opt. **1**(2), 192-199.

76. Mourant, J.R., Fuselier, T., Boyer, J., Johnson, T.M., and Bigio, I.J., 1997. Predictions and measurement of scattering and absorption over broad wavelength ranges in tissue. Appl. Opt. **36**, 949-957.

77. Mourant, J.R., Hielscher, A.H., Eick, A.A., Johnson, T.M., and Freyer, J.P., 1998. Evidence of intrinsic differences in the light scattering properties of tumorigenic and nontumorigenic cells. Cancer **84**, 366-374.

78. Murase, K., Saka, T., Asai, T., and Ikeda, H., 1999. Functional circuitry for the induction of prolonged excitation in the rat spinal dorsal horn. Eur. J. Neurosci. **11**, 3355-3358.

79. Nilsson,A.M.K., Sturesson, C., Liu, D.L., and Andersson-Engels, S., 1998. Changes in spectral shape of tissue optical properties in conjunction with laser-induced thermotherapy. Appl. Opt. **37**(7), 1256-1267.

80. Nomura, Y, Fuji, F. Sato, C., Nemoto, M., and Tamura, M., 2000. Exchange transfusion with fluorocarbon for studying synaptically evoked optical signal in rat cortex. Brain Res. Prot. **5**, 10-15.

81. Patterson, M.S., Chance, B., and Wilson, B.S., 1986. Time-resolved reflectance and transmittance for the non-invasive measurement of tissue optical properties. App. Opt. **28**, 2331-2336.

82. Paunescu, L.A., 2001. Tissue blood flow and oxygen consumption measured with near infrared frequency domain spectroscopy, University of Illinois at Urbana-Champaign.

83. Pogue, B.W., Poplack, S.P., Mcbride, T.O., Wells, W.A., Osterman, K.S., Osterberg, U.L., and Paulsen, K.D., 2001. Quantitative hemoglobin tomography with diffuse near-infrared spectroscopy: Pilot results in breast. Radiology **218**, 261-266.

84. Price, D.D., Hayashi, H., Dubner, R., and Ruda, M.A., 1979. Functional relationships between neurons of the marginal and substantia gelatinosa layers of the primate dorsal horn. J Neurophysiol. **42**, 1590–1608.

85. Qian, Z., Victor, S., Gu, Y., Giller, C.A., and Liu, H., 2003. 'Look Ahead Distance' of a fiber probe used to assist neurosurgery: Phantom and Monte Carlo study. Opt. Exp. **11**(16), 1844-1855.

86. Radhakrishnan, H., Senapati, A.K., Kashyap, D.R., Peng, Y.B., and Liu, H., 2005. Light scattering from rat nervous system measured intraoperatively by near infrared reflectance spectroscopy. J Biomed. Opt. **10**, 051405.

87. Radhakrishnan, H., Liu, H., Senapati, A.K., and Peng, Y.B., 2006. Determination of hemoglobin oxygen saturation in rat sciatic nerve by in vivo near infrared spectroscopy. Brain Res. Prot. **In Print**.

88. Rector, D.M., Poe, G.R., Kristensen, M.P., and Harper, R.M., 1997. Light scattering changes follow evoked potentials from hippocampal Schaeffer collateral stimulation. J Neurophysiol. **78**, 1707-1713.

89. Rector, D.M., Carter, K.M., Volegov, P.L., and George, J.S., 2005. Spatio-temporal mapping of rat whisker barrels with fast scattered light signals. Neuroimage **26**, 619-627.

90. Rorden, C., and Karnath, H.O., 2004. Using human brain lesions to infer function: a relic from a past era in the fMRI age? Nat Rev Neurosci. **5**(10), 813-819.

91. Sasaki, S., Yazawa, I., Miyakawa, N., Mochida, H., Shinomiya, K., Kamino, K., Momose-Sato, Y., and Sato, K., 2002. Optical Imaging of intrinsic signals induced by peripheral nerve stimulation in the in vivo rat spinal cord NeuroImage **17**, 1240–1255.

92. Sato, H., Fuchino, Y., Kiguchi, M., Katura, T., Maki, A., Yoro, T., and Koizumi, H., 2005. Intersubject variability of near infrared spectroscopy signals during sensorimotor cortex activation. J Biomed. Opt. **10**, 1-10.

93. Schwarzmaier, H.J., Yaroslavsky, A.N., Yaroslavsky, I.V., Goldbach, T., Kahn, T., Ulrich, F., Schulze, P.C., and Schober, R., 1997. Optical properties of native and coagulated human brain structures. SPIE Proceeding **2970**, 492-499.

94. Schweitzer, D., Hammer, M., Kraft, J., Thamm, E., Konigsdorffer, E., and Strobel, J., 1999. *In vivo* measurement of the oxygen saturation of retinal vessels in healthy volunteers. IEEE Trans Biomed Eng. **46,** 1454-1465.

95. Senapati, A.K., Radhakrishnan, H., Liu, H., and Peng, Y.B., 2005. Detection of degeneration in rat sciatic nerve by in vivo near infrared spectroscopy. Brain Res. Protocol **14**, 119-125.

96. Sevick, E.M., Chance, B., Leigh, J., Nokia, S., and Maris. M., 1991. Quantification of time- and frequency-resolved optical spectra for the determination of tissue oxygenation. Anal. Biochem. **195**, 330-351.

97. Soyemo, O.O., Landry, M.R., Yang, Y., Idwasi, P.O., and Soller, B.R., 2005. Skin color correlation for tissue spectroscopy: demonstration of a novel approach for tissue mimicking phantoms. Appl. Spectroscopy **59**, 237-244.

98. Strangman, G., Boas, D.A., and Sutton, J.P., 2002. Non-invasive neuroimaging using near infrared light. Biol. Psychiatry **52**, 679-693.

99. Svaasand, L.O., and Ellingsen, R., 1983. Optical properties of human brain. Photochem. Photobiol. **38**, 293-299.

100. Swartling, J., Bassi, A., D'Andrea, C., Pifferi, A., Torricelli, A., and Cubeddu, R., 2005. Dynamic time-resolved diffuse spectroscopy based on supercontinuum light pulses. Appl. Opt. **44**, 4684-4692

101. Symms, M., Jager, H.R., Schmierer, K., and Yousry, T.A., 2004. A review of structural magnetic resonance neuroimaging. J Neurol Neurosurg Psychiatry **75**(9), 1235-44.

102. Taddeucci, A., Martelli, F., Barilli, M., Ferrari, M., and Zaccanti, G., 1996. Optical properties of brain tissue. J. of Biomed. Opt. **1**(1), 117-123.

103. Takahashi, Y., Chiba, T., Kurokawa, M., and Aoki, Y., 2003. Dermatomes and the central organization of dermatomes and body surface regions in the spinal cord dorsal horn in rats. J Comp. Neurol. **462**, 29–41.

104. Tasaki, I., 1999. Rapid structural changes in nerve fibers and cells associated with their excitation processes. Jpn. J Physiol. **49**, 125–138.

105. Toronov, V., Webb, A., Choi, J. H., Wolf, M., Michalos, A., Gratton, E., and Hueber, D., 2001. Investigation of human brain hemodynamics by simultaneous near-infrared spectroscopy and functional magnetic resonance imaging. Med. Phys. **28**, 521–527.

106. Tsau, Y., Wenner, P., O'Donovan, M.J., Cohen, L.B., Loew, L.M., and Wuskell, J.P., 1996. Dye screening and signal-to-noise ratio for retrogradely transported voltage dyes. J. Neurosci. Methods **70,** 121-129.

107. Uchino, H., Elmer, E., Uchino, K., Lindvall, O., and Siesjo, B.K., 1995. Cyclosporin A dramatically ameliorates CA1 hippocampal damage following transient forebrain ischaemia in the rat. Acta Physiol. Scand. **155**, 469-471.

108. van Assendelft, O.W. and Zijlstra, W.G., 1975. Extinction coefficients for use in equations for the spectrophotometric analysis of hemoglobin mixtures. Anal. Biochem. **69**, 43-48.

109. van der Zee, P., Cope, M., Arridge, S.R., Essenpreis, M., Potter, L.A., Edwards, A.D., Wyatt, J.S., McCormick, D.C., Roth, S.C., Reynolds, E.O.R., and Delpy, D.T., 1992. Experimentally measured optical pathlengths of adult human head, calf, and forearm and the head of newborn infants as a function of inter optode spacing. Adv. Exp. Med. Biol. **316**, 143-153.

110. van der Zee, P., Essenpreis, M., and Delpy, D.T., 1993. Optical properties of Brain tissue in Photon Migration and Imaging in Random Media and Tissues: Chance, B., Alfano, R.R., and Katzir, A., eds. Proc. SPIE. **1888**, 454-465.

111. van Kampen, E.J. and Zijlstra, W.G., 1965. Determination of hemoglobin and its derivatives. Adv. Clin. Chem. **8**, 141-187.

112. Villringer, A. and Chance, B., 1997. Non-invasive optical spectroscopy and imaging of human brain function. Trends Neurosci. **20**, 435–442.

113. Wachowiak, M. and Cohen, L.B., 2003. Correspondence between odorant-evoked patterns of receptor neuron input and intrinsic optical signals in the mouse olfactory bulb. J Neurophysiol. **89**, 1623-1639.

114. Wenner, P., Tsau, Y., Cohen, L.B., O'Donovan, M.J., and Dan, Y., 1996. Voltage-sensitive dye recording using retrogradely transported dye in the chicken spinal cord: Staining and signal characteristics. J. Neurosci. Methods **70**, 111-120.

115. Wiensperger, N., Sylvia, A.N., and Jobsis, F.F., 1981. Incomplete transient ischemia. A non-destructive evaluation of *in vivo* cerebral metabolism and hemodynamics in rat brain. Stroke **12**, 864-868.

116. Wilson, B.C., Patterson, M.S., Flock, S.T., and Wyman, D.R., 1988. Tissue optical properties in relation to light propagation models and in vivo dosimetry. Photon Migration in Tissues. B. Chance, Plenum Press.

117. Wolf, M., Wolf, U., Choi, J.H., Gupta, R., Safonova, L.P., Paunescu, L.A., Michalos, A., and Gratton, E., 2002. Functional frequency-domain near-infrared spectroscopy detects fast neuronal signal in the motor cortex. Neuroimage **17**, 1868-1875.

118. Yaroslavsky, A.N., Schulze, P.C., Yaroslavsky, I.V., Schober, R., Ulrich, F., and Schwarzmaier, H.J., 2002. Optical properties of selected native and coagulated human brain tissues in vitro in the visible and near infrared spectral range. Phys Med Biol. **47**(12)**,** 2059-73.

119. Yodh, A.G. and Boas, D.A., 2003. Functional Imaging with Diffusing Light. Biomedical Photonics Handbook, ed. by T. Vo-Dinh, CRC Press, New York, 21-1—21-45.

120. Zijlstra, W.G., Buursma, A., and Meeuwsen-van der Roest, W.P., 1991. Absorption spectra of human fetal and adult oxy-hemoglobin, deoxy-hemoglobin, carboxyhemoglobin and methemoglobin. Clin. Chem. **37**, 1633-1638.

121. Zimmermann,M., 1983. Ethical guidelines for investigations of experimental pain in conscious animals. Pain **16**, 109-110.

122. Zonios, G., Perelman, L.T., Backman, V., Manoharan, R., Fitzmaurice, M., van Dam, J., and Feld, M.S., Diffuse Reflectance Spectroscopy of Human Adenomatous Colon Polyps In Vivo. Appl. Opt. **38**(31), 6628-6637.

BIOGRAPHICAL INFORMATION

Harsha Radhakrishnan was born on November 14th, 1978 in Chennai, India. He received his Bachelor of Engineering degree in Electronics and Instrumentation Engineering from University of Madras, India in June, 2000 and Master of Science degree in Medical Software from Manipal Academy of Higher Education in May 2002. In spring 2003, he started his Master of Science degree in Biomedical Engineering from the University of Texas at Arlington and completed it in the summer of 2006. His research interest includes functional neuron-imaging and medical imaging techniques.